contribution to patient-specific stress assessment in the human left ventricle using image-based finite element analyse

Sareh Behdadfar

N°d'ordre NNT : 2017LYSEM004

THESE de DOCTORAT DE L'UNIVERSITE DE LYON
opérée au sein de
l'Ecole des Mines de Saint-Etienne

Ecole Doctorale N° 488
Sciences, Ingénierie, Santé

Spécialité de doctorat : Mécanique et Ingénierie
Discipline : Biomécanique

Soutenue publiquement le 10/02/2017, par :
(Sareh BEHDADFAR)

CONTRIBUTION TO PATIENT-SPECIFIC STRESS ASSESSMENT IN THE HUMAN LEFT VENTRICLE USING IMAGE-BASED FINITE-ELEMENT ANALYSES

Devant le jury composé de :

CROISILLE, Pierre Professor CHU Saint-Étienne, Saint-Priest-en-Jarez — Président

SAMSET, Eigil Professor, GE Vingmed Ultrasound, Oslo — Rapporteur
DOBLARE, Manuel Full Professor, University of Zaragoza, Sevilla — Rapporteur
SERMESANT, Maxime Research Scientist, Inria Sophia Antipolis, sophia Antipolis — Examinateur

AVRIL, Stéphane Professor, Mines Saint etienne, saint-etienne — Directeur de thèse
SUNDNES, Joakim Associate Professor, Simula Research Laboratory and University of Oslo, Fornebu — Co-Directeur de thèse
NAVARRO, Laurent Assistant Professor, Mines Saint Etienne, Saint-Etienne — Co-Encadrant de thèse

Spécialités doctorales	Responsables :	Spécialités doctorales	Responsables
SCIENCES ET GENIE DES MATERIAUX	K. Wolski Directeur de recherche	MATHEMATIQUES APPLIQUEES	O. Roustant, Maître-assistant
MECANIQUE ET INGENIERIE	S. Drapier, professeur	INFORMATIQUE	O. Boissier, Professeur
GENIE DES PROCEDES	F. Gruy, Maître de recherche	IMAGE, VISION, SIGNAL	JC. Pinoli, Professeur
SCIENCES DE LA TERRE	B. Guy, Directeur de recherche	GENIE INDUSTRIEL	A. Dolgui, Professeur
SCIENCES ET GENIE DE L'ENVIRONNEMENT	D. Graillot, Directeur de recherche	MICROELECTRONIQUE	S. Dauzere Peres, Professeur

EMSE : Enseignants-chercheurs et chercheurs autorisés à diriger des thèses de doctorat (titulaires d'un doctorat d'État ou d'une HDR)

ABSI	Nabil	CR	Génie industriel	CMP
AVRIL	Stéphane	PR2	Mécanique et ingénierie	CIS
BALBO	Flavien	PR2	Informatique	FAYOL
BASSEREAU	Jean-François	PR	Sciences et génie des matériaux	SMS
BATTAIA-GUSCHINSKAYA	Olga	CR	Génie industriel	FAYOL
BATTON-HUBERT	Mireille	PR2	Sciences et génie de l'environnement	FAYOL
BERGER DOUCE	Sandrine	PR2	Sciences de gestion	FAYOL
BIGOT	Jean Pierre	MR(DR2)	Génie des Procédés	SPIN
BILAL	Essaid	DR	Sciences de la Terre	SPIN
BLAYAC	Sylvain	MA(MDC)	Microélectronique	CMP
BOISSIER	Olivier	PR1	Informatique	FAYOL
BONNEFOY	Olivier	MA(MDC)	Génie des Procédés	SPIN
BORBELY	Andras	MR(DR2)	Sciences et génie des matériaux	SMS
BOUCHER	Xavier	PR2	Génie Industriel	FAYOL
BRODHAG	Christian	DR	Sciences et génie de l'environnement	FAYOL
BRUCHON	Julien	MA(MDC)	Mécanique et ingénierie	SMS
BURLAT	Patrick	PR1	Génie Industriel	FAYOL
COURNIL	Michel	PR0	Génie des Procédés	DIR
DAUZERE-PERES	Stéphane	PR1	Génie Industriel	CMP
DEBAYLE	Johan	CR	Image Vision Signal	CIS
DELAFOSSE	David	PR0	Sciences et génie des matériaux	SMS
DELORME	Xavier	MA(MDC)	Génie industriel	FAYOL
DESRAYAUD	Christophe	PR1	Mécanique et ingénierie	SMS
DOLGUI	Alexandre	PR0	Génie Industriel	FAYOL
DRAPIER	Sylvain	PR1	Mécanique et ingénierie	SMS
FAVERGEON	Loïc	CR	Génie des Procédés	SPIN
FEILLET	Dominique	PR1	Génie Industriel	CMP
FRACZKIEWICZ	Anna	DR	Sciences et génie des matériaux	SMS
GARCIA	Daniel	MR(DR2)	Génie des Procédés	SPIN
GAVET	Yann	MA(MDC)	Image Vision Signal	CIS
GERINGER	Jean	MA(MDC)	Sciences et génie des matériaux	CIS
GOEURIOT	Dominique	DR	Sciences et génie des matériaux	SMS
GONDRAN	Natacha	MA(MDC)	Sciences et génie de l'environnement	FAYOL
GRAILLOT	Didier	DR	Sciences et génie de l'environnement	SPIN
GROSSEAU	Philippe	DR	Génie des Procédés	SPIN
GRUY	Frédéric	PR1	Génie des Procédés	SPIN
GUY	Bernard	DR	Sciences de la Terre	SPIN
HAN	Woo-Suck	MR	Mécanique et ingénierie	SMS
HERRI	Jean Michel	PR1	Génie des Procédés	SPIN
KERMOUCHE	Guillaume	PR2	Mécanique et Ingénierie	SMS
KLOCKER	Helmut	DR	Sciences et génie des matériaux	SMS
LAFOREST	Valérie	MR(DR2)	Sciences et génie de l'environnement	FAYOL
LERICHE	Rodolphe	CR	Mécanique et ingénierie	FAYOL
LI	Jean-Michel		Microélectronique	CMP
MALLIARAS	Georges	PR1	Microélectronique	CMP
MAURINE	Philippe	Ingénieur de recherche	Microélectronique	CMP
MOLIMARD	Jérôme	PR2	Mécanique et ingénierie	CIS
MONTHEILLET	Frank	DR	Sciences et génie des matériaux	SMS
MOUTTE	Jacques	CR	Génie des Procédés	SPIN
NEUBERT	Gilles	PR	Génie industriel	FAYOL
NIKOLOVSKI	Jean-Pierre	Ingénieur de recherche		CMP
NORTIER	Patrice	PR1		SPIN
OWENS	Rosin	MA(MDC)	Microélectronique	CMP
PICARD	Gauthier	MA(MDC)	Informatique	FAYOL
PIJOLAT	Christophe	PR0	Génie des Procédés	SPIN
PIJOLAT	Michèle	PR1	Génie des Procédés	SPIN
PINOLI	Jean Charles	PR0	Image Vision Signal	CIS
POURCHEZ	Jérémy	MR	Génie des Procédés	CIS
ROBISSON	Bruno	Ingénieur de recherche	Microélectronique	CMP
ROUSSY	Agnès	MA(MDC)	Génie industriel	CMP
ROUSTANT	Olivier	MA(MDC)	Mathématiques appliquées	FAYOL
ROUX	Christian	PR	Image Vision Signal	CIS
STOLARZ	Jacques	CR	Sciences et génie des matériaux	SMS
TRIA	Assia	Ingénieur de recherche	Microélectronique	CMP
VALDIVIESO	François	PR2	Sciences et génie des matériaux	SMS
VIRICELLE	Jean Paul	DR	Génie des Procédés	SPIN
WOLSKI	Krzystof	DR	Sciences et génie des matériaux	SMS
XIE	Xiaolan	PR1	Génie industriel	CIS
YUGMA	Gallian	CR	Génie industriel	CMP

ENISE : Enseignants-chercheurs et chercheurs autorisés à diriger des thèses de doctorat (titulaires d'un doctorat d'État ou d'une HDR)

BERGHEAU	Jean-Michel	PU	Mécanique et Ingénierie	ENISE
BERTRAND	Philippe	MCF	Génie des procédés	ENISE
DUBUJET	Philippe	PU	Mécanique et Ingénierie	ENISE
FEULVARCH	Eric	MCF	Mécanique et Ingénierie	ENISE
FORTUNIER	Roland	PR	Sciences et Génie des matériaux	ENISE
GUSSAROV	Andrey	Enseignant contractuel	Génie des procédés	ENISE
HAMDI	Hédi	MCF	Mécanique et Ingénierie	ENISE
LYONNET	Patrick	PU	Mécanique et Ingénierie	ENISE
RECH	Joël	PU	Mécanique et Ingénierie	ENISE
SMUROV	Igor	PU	Mécanique et Ingénierie	ENISE
TOSCANO	Rosario	PU	Mécanique et Ingénierie	ENISE
ZAHOUANI	Hassan	PU	Mécanique et Ingénierie	ENISE

Mise à jour : 29/06/2015

تقدیم به پدر و مادر زحمتکش و فداکارم,

و به خواهرها و برادر عزیزم,

و توماس .

Remerciements

Who we meet on our life journey has an important impact on our personality and destination. I believe that I thanked everybody during my defence day which, in my opinion, was the best way to express my feelings in person rather than writing in a white page.
I would like to thank all the people who helped and support me during these years. Doing a PhD is a great achievement which changes all the aspects of one's life in different manners.
I would like to thank, in the first place, all the Jury members who travelled a long way to come and participate in one of my best days in my life. The president, Prof. Pierre CROISILLE, and other examinators : Prof. Eigil SAMSET, Prof. Manuel DOBLARE and Dr. Maxime SERMESANT. I am very grateful to have your great opinions on my PhD thesis which gave several new directions to the potential future works.
I would like to thank particularly Stéphane Avril, my PhD director, who supported me to work on this new subject and to fly higher. He was a great motivation in order to develop several methods and achieve interesting results. Then, I would like to thank Joakim SUNDNES, my codirector, who was very patient all the time to explain all the details I needed. You were always available for my questions and I am grateful for that. You are one of my favourite people during my PhD cause I learned not only from you in details about cardiac mechanics but also about personal aspects as a PhD student. It was also a chance for me to work with Laurent NAVARRO, my co-advisor. We spent a lot of time discussing in a very good atmosphere about different methods and solutions while drawing on the board. I thank you for all these good memories during my PhD (Aussi à ta petite famille). At last, I would like to thank Molly MALECKAR, my co-advisor. She is a great and joyful person. I've met her while I was a junior and she, as a woman, gave me the envy to become someone like her. I regret that she could not come for my defence where I could express my feelings directly. I thank you for your support during the last months of my PhD; it was a great chance to have your opinions.
I would like to thank all my friends and colleagues in Ecole des Mines : Previous doctors -Aaron (and Manu ;)), Bilal, Alex, Olivier, Karolina, Nicola, PY, ...-, friend became sister Amélie (ma meileur rencontre à Saint Etienne et les deux Ms ;)), sweet/bella Cristina and Francesca, officemate/fun Boris, nice/sweet Armelle, active Fanette, chef/pro David, Bretonne/nice Klervi,

sportive/funny Pierrech, determined Olfa, sweet Victor, nice Baptiste[2], sweet/funny Frances, kind as a father/generous Jérôme, kind/helpful Françoise, determined Claire, dance champion Mikhaël, friendly/sweet Romain, nice Witold, kind Phuoc and my generous teacher Pierre Badel. I also thank Thierry, Afafe, Vincent, Sabri, Nicola (technician), Woos-suck, Thomas, Martin, Jérémie, Nathalie and Coralie that permitted me to work in a warm atmosphere. My kind friends in CCSTI La Rotonde : Celine, Mathilde, Christine and Julie. I learnt a lot from you and I am grateful for that.
My Iranian friends: Jamal (Kabab paze maher), Solmaz[2] (mehraboona), Setareh va shima (joo-jehaye man), Saheb va Gita (nasimeh garmeh darya), Hossein (khoshe abadi) va Mohsen.
Finally and the best to my Family: My lovely parents, brother and sisters, aunts and uncles, cousins (Specially Ghazal, my PhD soul-mate), my best and lovely fan Thomas and his family (Mamoune, Nadine, Alain,...) who became my family.

Table des matières

Table des figures

Liste des tableaux

Chapitre 1

Introduction Générale

"The heart of animals is the foundation of their life, the sovereign of everything within them, the sun of their microcosm, that upon which all growth depends, from which all power proceeds."
William Harvey (1578-1657), An Anatomical Disquisition on the Motion of the Heart and Blood in Animals.

Préambule

Le cœur est un organe fascinant. En raison de son importance, il a été largement étudié par les scientifiques pour comprendre les causes de ses éventuels dysfonctionnements et trouver des traitements efficaces permettant d'anticiper des risques cardiaques comme l'infarctus du myocarde ou la mort subite [Ridker, 2003]. Néanmoins, encore aujourd'hui, selon la société européenne de cardiologie, les maladies cardiovasculaires (MCV) sont la principale cause de mortalité en Europe, responsables de plus de 4 millions de décès par an [Network and of Cardiology, 2012]. On doit donc encore intensifier l'effort de recherche dans ce domaine, qui couvre de nombreuses disciplines scientifiques.

La discipline sur laquelle porte les travaux de cette thèse est la biomécanique du tissu cardiaque. De nombreux travaux ont permis dès les années 1980 de déterminer le comportement mécanique du tissu cardiaque in-vitro [Dokos et al., 2002, Demer and Yin, 1983, Yin et al., 1987, Smaill and Hunter, 1991] et les progrès de l'imagerie médicale ont également permis de déterminer le comportement mécanique du tissu cardiaque in-vivo dans les années 2000 [Perk et al., 2007,Dandel et al., 2009,Geyer et al., 2010,Heimdal, 2011,Kaluzynski et al., 2001,D'hooge et al., 2002, Reisner et al., 2004, Leitman et al., 2004]. Aujourd'hui la structure multi-échelle

(dont nano et macro) du tissu cardiaque ainsi que le lien entre cette structure et la fonction (ou dysfonction) cardiaque sont connues.

Tous ces travaux ont permis de mettre en place des modèles détaillés de la machinerie cardiaque, de l'échelle cellulaire à l'échelle d'organe, permettant notamment de simuler les déformations du tissu au cours d'un cycle cardiaque [Marchesseau et al., 2013a, Niederer and Smith, 2009, Vendelin et al., 2002, Hunter et al., 1998, Nash and Hunter, 2000, Sundnes et al., 2007]. Le défi majeur aujourd'hui est de rendre ces modélisations spécifiques à chaque patient en prenant en compte la spécificité des propriétés mécaniques du tissu de chaque individu, l'organisation locale des fibres musculaires, la présence d'éventuelles pathologies, etc. Cela permettra d'employer les modèles, en association avec des techniques d'imagerie médicale telles que l'imagerie par résonance magnétique (IRM), les ultrasons (US) et le scanner de tomodensitométrie (CT scan), dans des outils de médecine prédictive pour affiner le diagnostic des pathologies et cibler les traitements.

Le chemin pour relever ce défi semble encore long avec de nombreux verrous à relever. Dans cette thèse, nous faisons l'hypothèse que la contrainte dans le tissu cardiaque in-vivo doit être reconstruite avec précision pour pouvoir comprendre, analyser, diagnostiquer et traiter une dysfonction cardiaque. Dans la reconstruction de ces cartes de contrainte, deux verrous principaux ont motivé cette thèse :

1. le champ de contrainte dans le tissu cardiaque peut être prédit par les modèles numériques mais cela requiert de déterminer précisément les propriétés mécaniques du tissu. Certains modèles nécessitent plus de 10 valeurs à déterminer, ce qui n'est pas réaliste à l'échelle de chaque individu. La question qui est posée est alors s'il est possible de reconstruire le champ de contrainte dans le tissu cardiaque dans un contexte d'incertitude forte sur les propriétés mécaniques.
2. les modèles nécessitent souvent des données d'imagerie avec très forte résolution spatiale pour pouvoir être reconstruits et exploités dans la reconstruction précise des cartes de contraintes dans le tissu cardiaque. Cela oriente la modalité d'imagerie vers l'IRM. Cependant il s'agit d'une modalité coûteuse. La seconde question qui est posée est donc s'il est possible d'exploiter des données d'échographie pour atteindre les mêmes objectifs.

Par conséquent, une collaboration a été établie avec Simula Research Laboratory à Oslo en Norvège et le centre d'ingénierie et santé (CIS) de Mines Saint Étienne pour pouvoir relever ces verrous. Cela a permis de lever les financements pour cette thèse de doctorat qui a été encadrée par Prof Stéphane AVRIL et Dr. Laurent NAVARRO de CIS de Mines Saint Etienne, ainsi que

par Dr. Joakim SUNDNES et Dr. Molly M. MALECKAR de Simula Research Laboratory.

Après cette introduction générale, ce manuscrit est organisé en quatre chapitres dont 3 sont des articles de revues internationales à comité de lecture rédigés en anglais (2 soumis et 2 en attente de soumission).

Le *chapitre 1* de cette thèse est consacré à l'état de l'art : aspects médicaux et physiologiques du système cardio-vasculaire, caractéristiques générales du comportement du ventricule gauche (VG), pathologies notamment le Bloc de Branche Gauche (BBG), et méthodes d'imagerie cardiaque. Les modèles de comportement mécanique de la littérature sont également présentés avec les protocoles expérimentaux qui permettent d'en identifier les paramètres. Enfin, une revue exhaustive de la littérature scientifique est présentée sur les simulations numériques prédictives en biomécanique cardiaque. Les objectifs de la thèse sont finalement résumés en fin de chapitre 1.

Dans le *chapitre 2*, l'impact des modèles de comportement et de leurs paramètres sur le champ de contrainte dans le VG d'un sujet sain est étudié avec une approche originale, d'abord en mode passif, puis dans le cas d'une contraction. Il est montré que dans plusieurs modèles, la dépendance aux paramètres de comportement est faible voire nulle. Ce chapitre nous permettre de mieux comprendre comment les différents paramètres de comportement influent sur la contrainte dans le tissu.

Dans le *chapitre 3*, nous introduisons une nouvelle méthode de morphing pour générer un maillage (patient-spécifique) qui servira à effectuer des calculs éléments finis (*EFs*) à partir d'un modèle de référence. Nous avons développé cette méthode pour adapter une géométrie de VG maillée en hexaèdre fins à des d'imagerie US. Une validation étant nécessaire, nous avons effectué des calculs EFs de fin-diastole sur 8 sujets pour analyser l'efficacité de notre approche.

Dans le *chapitre 4*, à partir de la méthode présentée au chapitre 3, une approche a été mise en place pour détecter une dysfonction tissulaire sur les sujets d'une cohorte de patients porteurs de la pathologie BBG. Les données ont été fournies par Simula Research Laboratory. Après identification de la contrainte moyenne de contraction sur un ventricule puis reconstruction de la déformation systolique induite par cette contrainte par analyse EFs, la méthode permet de déterminer les zones potentiellement infarctées et a été validée avec succès sur des données synthétiques simulant une ischémie aiguë. Les résultats mettent en évidence le potentiel prometteur de l'approche.

Après la *conclusion générale* et les *perspectives* de ce travail, le manuscrit comporte une *annexe* présentant un travail complémentaire qui a été mené en parallèle et qui a débouché vers

un modèle de matériau isotrope transverse avec contraction active dans le logiciel Abaqus® (avec développement d'une routine UMAT en Fortran®).

Introduction

The heart is a fascinating organ. Because of its importance, it has been studied extensively by scientists to understand the causes of its possible malfunctions in order to find effective treatments for anticipating cardiac risks such as myocardial infarction or sudden cardiac death [Ridker, 2003]. Nevertheless, according to the European Society of Cardiology, cardiovascular disease (CVD) are the leading cause of death in Europe and responsible for more than 4 million deaths per year [Network and of Cardiology, 2012]. So it is necessary to consider further research effort in this area which covers several scientific disciplines.

The main focus of this thesis is the biomechanics of the heart tissue. Generally, most of researches in the 1980s were focused to determine the mechanical behavior of the cardiac tissue in-vitro [Dokos et al., 2002, Demer and Yin, 1983, Yin et al., 1987, Smaill and Hunter, 1991], and later the advances in medical imaging techniques have allowed to determine these properties in-vivo in the 2000s [Perk et al., 2007, Dandel et al., 2009, Geyer et al., 2010, Heimdal, 2011, Kaluzynski et al., 2001, D'hooge et al., 2002, Reisner et al., 2004, Leitman et al., 2004]. Nowadays, the multiscale structure (from nano to macro) of the heart tissue, as well as the link between this structure and the cardiac function (or dysfunction) are known.

All these works aimed to develop and improve detailed models of cardiac machinery, from cellular to the organ scale, allowing to simulate particularly the deformation of the cardiac tissue during a complete cycle [Marchesseau et al., 2013a, Niederer and Smith, 2009, Vendelin et al., 2002, Hunter et al., 1998, Nash and Hunter, 2000, Sundnes et al., 2007]. Today, the major challenge is to make these models specific to each patient, taking into account the specific mechanical properties of each individual, the local direction of the muscle fibers, the presence of any diseases, etc. Such a complex system should employ FE models, in combination with medical imaging techniques such as magnetic resonance imaging (MRI), ultrasound (US) and computed tomography scan (CT scan), in medical prediction tools to refine the diagnosis of a patient's disease and target the best personalized treatment.

The way to meet this challenge seems still far to achieve with numerous scientific challenges and locks up. In this thesis, we assume that the stress in the cardiac tissue should be reconstructed accurately in order to understand, analyse, diagnose and treat cardiac dysfunction. In the reconstruction of these stress maps, two main barriers motivated this thesis : 1. the stress

field in the cardiac tissue can be predicted by numerical models but this requires to determine, precisely, the mechanical properties of the tissue. Some models require more than 10 values to be identified, which is not realistic and easy to interpret for each individual. The question was whether it is possible to reconstruct the stress field in the heart tissue with a strong uncertainty on the mechanical properties, 2. often numerical models require high spatial resolution images in order to reconstruct the geometry and to be used for accurately estimate the cardiac tissue stress distribution map. In this case, the MRI images attracted more attentions due to their advantages despite the fact that it is an expensive technique. The second question asked is whether it is possible to use US data to achieve the same objectives.

Therefore, a collaboration was established between Simula Research Laboratory in Oslo, Norway and the Center for Biomedical and Healthcare Engineering of Mines Saint Etienne to meet these barriers and to answer to the proposed questions. This collaboration helped us to raise funding for this PhD which is supervised by Prof. Stéphane Avril and Dr. Laurent NAVARRO from Mines Saint Etienne, and by Dr. Joakim Sundnes and Dr. Molly M. MALECKAR from Simula Research Laboratory.

After this *General Introduction*, this manuscript is organized into four chapters including 3 articles for international journals in English (2 submitted and 2 pending for submission).

The *Chapter 1* of this thesis is devoted to the state of the art of the medical and physiological aspects of the cardiovascular system, the general characteristics of the left ventricle (LV) behaviour and its related pathologies including the Left Bundle branch block (LBBB), and the cardiac imaging method which has been used in this thesis. Several models from the literature which describe the cardiac mechanical behaviour are also presented with the experimental protocols used to identify their parameters. Finally, an exhaustive review of the literature is presented on personalized simulations in cardiac mechanics. The objectives of the thesis are finally summarized at the end of *Chapter 1*.

In *Chapter 2*, the impact of different strain energy functions and their parameters on the stress field of a healthy LV subject is studied with an original approach, first for a passive model and then for a contraction. It is shown that the mechanical behaviour dependency on the strain energy parameters is low or zero. This Chapter allows us to understand better how different parameters affect the stress behaviour in the cardiac tissue.

In *Chapter 3*, we introduce a new mesh morphing method to generate patient-specific mesh from a reference geometry. This algorithm is developed to take a detailed FE model of the LV with hexahedral elements and morph it to the patient's coarse geometries obtained from US

images. We performed diastolic FE simulations of 8 subjects to analyse the efficiency and to validate our approach.

In *Chapter 4*, an approach was developed to detect abnormal tissue zone in the LV. The FE meshes used in this Chapter are the results of the proposed approach in *Chapter 3*. The cohort data was provided by Simula Research Laboratory. For each patient, an average active stress value was identified for ventricular contraction employing a simple strain energy function and contraction model. This permitted us to detect the abnormal zones with significant differences in the ventricular deformation induced by this active contraction. Application of this method for detection of potentially infarcted patients has been validated successfully on synthetic data simulating acute ischemia.

After the *General Conclusion* and perspectives of this work, the manuscript includes an *Appendix* with additional work that was conducted in parallel and that resulted in an isotropic transverse material model with active contraction in Abaqus® software (a UMAT routine in Fortran®).

Chapitre 2

Introduction à la modélisation du cœur

Ce chapitre présente le contexte médical, scientifique et le point de vue des biomécaniciens sur différents aspects du comportement du VG. Ainsi, ce chapitre va nous permettre de présenter les motivations de cette thèse.

Sommaire

Préambule

Le cœur est composé de quatre chambres dont deux ventricules et deux atriums (Figure 2.1 & 2.2). La cavité la plus importante qui pompe le sang oxygéné dans le système cardio-vasculaire est le VG et le ventricule droit renvoie le sang désoxygéné vers les poumons (les circuits systémiques et pulmonaires). Le muscle cardiaque est principalement constitué du myocarde. Les tissus annexes du myocarde sont (Figure 2.3): l'endocarde à l'intérieure et l'épicarde à l'extérieure.

Le cycle cardiaque contient deux phases principales: la diastole et la systole. Entre chaque phase, il a y une étape isovolumique où le tissu change de comportement (sans changer son volume) qui est donc en état de relaxation au début de la contraction (Figure 2.6). La contraction est le résultat de la propagation d'une impulsion électrique à l'intérieur du muscle cardiaque. Cette activation est due à un stimulateur naturel qui régule le rythme cardiaque via deux ensembles de cellules électriques nommés sino-atrial (SA) et le atrioventriculaire (AV). Ces cellules stimulent successivement la contraction tout au long de muscle cardiaque par le réseau nerveux (Figure 2.4).

Plusieurs études montrent que les fibres cardiaques sont composées de plusieurs centaines à plusieurs milliers de rangées parallèles de myofibrilles (Figure 2.7.a). Ces myofibrilles sont constituées de filaments protéiques minces et épais (myosine et actine) disposées en sarcomères (Figure 2.7.b) et sont capable de générer ensemble une force de contraction. Dès que le potentiel d'action est émis par le SA et le AV, le réticulum sarcoplasmique libère une grande quantité d'ions calcium (Ca^{2+}) aux myofibrilles. Par conséquent, la concentration en ions calcium (Ca^{2+}) augmente dans le liquide intracellulaire et lorsqu'un certain seuil est atteint, les myosines se lient à l'actine et la contraction cellulaire se produit [Betts et al., 2013, Guyton and Hall, 2006, Netter, 1971].

Cette contraction musculaire dans la direction des myofibrilles provoque une torsion du VG qui se tourne pendant la phase systolique [Nakatani, 2011]. Cette rotation est due à l'organisation des myofibrilles à l'intérieur du tissu cardiaque. L'idée d'une architecture discrète des fibres cardiaques a été étudiée par [LeGrice et al., 1995a, LeGrice et al., 1995b] sur le cœur d'un chien. Ce cœur canin a été arrêté en phase de diastole et coupé tout au long des méridiens pour être analyser sous microscopie électronique. Les auteurs ont observé que les sections longitudinales-transmurals étaient construites en couches différentes à travers la paroi ventriculaire. De ce fait, ils ont suggéré un système de coordonnées local dans lequel la fibre, la feuille et la normale

perpendiculaire à leurs plans forment un repère orthogonal pour ce milieu continu.

Au cours des dernières décennies, les progrès dans le domaine de l'imagerie médicale notamment avec l'imagerie par l'IRM et en particulier avec le tenseur de diffusion par l'IRM (*TDIRM*); ont ouvert des solutions plus accessibles pour les mesures personnalisées de l'orientation des fibres in-vivo [Hsu et al., 1998, Scollan et al., 1998, Seemann et al., 2006, Lombaert et al., 2011, Scollan et al., 2000, Hooks et al., 2007, Vetter and McCulloch, 1998]. On peut constater sur la Figure 2.9, la variation d'orientation des fibres à travers l'épaisseur du VG, ces images ont été acquises à partir de TDIRM [Hsu et al., 1998]. Les directions des fibres cardiaques chez les mammifères ont été décrites comme variant de -70° environ à +70° de l'endocarde à l'épicarde [Pearlman et al., 1982, Streeter et al., 1978, Streeter and Hanna, 1973, Ross and Streeter Jr, 1975, Streeter and Bassett, 1966, Hort, 1960, Omens et al., 1991, Vetter and McCulloch, 1998, Nash and Hunter, 2000].

En 2012, la World Health Organisation a annoncé que les *maladies cardiovasculaires* ont tué mondialement 17,5 millions de personnes (Figure 2.10). Parmi ceux-ci, 7,4 millions de personnes sont mortes d'une *ischémie*. On observe une augmentation de la tendance mondiale de la mortalité due à l'ischémie depuis 2000 [WHO, 2012]. Cette tendance a motivé les autorités à prendre des mesures et consacrer plus de budget à la recherche sur les maladies cardiovasculaires pour fournir une compréhension et des traitements efficaces. Les trois principales maladies cardio-vasculaires sont présentées dans ce travail de thèse:

— Maladies cardiaques ischémiques: dues au manque d'approvisionnement en sang oxygéné et en nutriment pour le cœur, cette pathologie se développe au cours du temps. L'ischémie peut être due à l'athérosclérose, rétrécissement ou un blocage des artères coronaires qui va augmenter le risque d'infarctus du myocarde.

— Cardiomyopathie: pour une raison quelconque le muscle cardiaque ne peut pas se contracter. Cela peut être dû à une mutation des gènes ou être la conséquence d'une autre maladie. Souvent, il est difficile de caractériser cette pathologie en raison des structures complexes de protéines dans le myocarde, de la présence de mutations pathogènes, et d'autres déclencheurs prouvent affaiblir le muscle.

— BBG: l'activation du VG à travers la branche gauche du faisceau de His (Figure 2.4) est retardée par rapport au ventricule droit et à la paroi septale. Statistiquement, 40% des patients qui souffrent de la cardiomyopathie (de type dilatée) et d'une *insuffisance cardiaque* ont une contraction ventriculaire désynchronisée. Cette pathologie modifie la morphologie des ventricules (*remodelage*) qui peut être visualisée à l'aide de l'imagerie

médicale. Ce trouble est également visible dans la routine clinique d'électrocardiographie. Les patients présentant un infarctus du myocarde et un BBG ont un taux plus élevé de mortalité à l'hôpital (22, 6%) [Go et al., 1998, Hamby et al., 1983].

La compréhension de la structure du VG à l'échelle micro et macro nécessite une connaissance précise des propriétés du matériau. Les deux essais expérimentaux utilisés fréquemment pour déterminer les propriétés mécaniques du myocarde, sont des tests biaxiaux et en cisaillement. Dans ce contexte, la réponse biaxial d'un échantillon du myocarde est limitée à la description du comportement isotrope transverse [Demer and Yin, 1983, Yin et al., 1987, Smaill and Hunter, 1991] et plus tard, les tests de cisaillement réalisés sur un échantillon du myocarde ont décrit plutôt son comportement orthotrope [Dokos et al., 2002]. Il a également été souligné dans la littérature, que le myocarde est 1.5 à 3 fois plus rigide dans la direction des fibres que les autres directions [Humphrey et al., 1990, Yin et al., 1987]. Ce comportement est le plus souvent exprimé sous la forme d'une fonction exponentielle ou polynomiale où plusieurs de ces modèles sont basés sur l'hypothèse d'isotropie transverse. Trois fonctions classiques sont introduites ici pour modéliser le comportement du VG: le modèle de [Guccione et al., 1991], celui de [Holzapfel and Ogden, 2009] et celui de [Marchesseau et al., 2013a]. Dans ce travail, nous avons utilisé deux modèles pour effectuer des simulations numériques: [Guccione et al., 1991] et [Marchesseau et al., 2013a].

Le modèle de [Guccione et al., 1991] a été largement utilisé pour l'identification des paramètres du matériau. Cependant, les paramètres identifiés sont souvent différents en raison de la configuration de l'expérimentation et des conditions de chargement, de la méthode d'identification et des échantillons des animaux [Wang et al., 2013, Yettram and Beecham, 1998, Périé et al., 2013]. La modification des propriétés des tissus après la mort dans des tests in-vitro rend cette solution imprécise pour déterminer les propriétés mécaniques du myocarde. En outre, les paramètres sont fortement couplés, ce qui les rend difficile à interpréter et identifier.

Une description de chaque cycle cardiaque implique de faire face à un couple complexe de simulation multiphysique dans des domaines tels que l'électro-biochimie, la physique, la mécanique des fluides et des solides. Cependant, l'incorporation de tous ces phénomènes est coûteuse et très complexe à mettre en œuvre. L'interaction du flux sanguin et du myocarde dans les ventricules est considérée comme un problème d'interaction fluide-structure. Le couplage fluide-structure a été décrit par [Peskin and McQueen, 1997, Kovács et al., 2001, Domenichini et al., 2005] pour une phase de remplissage en utilisant les trois équations de la mécanique des fluides à partir des formulations de Navier Stokes et avec une méthode de *Arbitrary Lagrangian*

Eulerian. Les progrès dans ces méthodes d'EFs (fluide-structure) pour les applications comme les dispositifs d'assistance ventriculaire sont très prometteurs pour les traitements de différentes pathologies. Un autre exemple est la simulation électromécaniques (couplant l'électrophysiologie et la mécanique) qui nous permet de comprendre le mouvement du VG de l'échelle cellulaire à l'échelle de l'organe [Humphrey et al., 1990, Hunter et al., 1997, Nash, 1998].

L'influence de la géométrie dans les réponses mécaniques de simulation spécifique au patient a été étudiée précédemment [Miller and Lu, 2013, Mayeur et al., 2016, Joldes et al., 2016]. Dans ces travaux, il a été montré que les modèles de matériaux isotropes sont insensibles à leurs paramètres, mais fortement couplés à la géométrie et l'épaisseur de sa paroi. Ceci met en évidence l'importance de la génération de modèles précis à partir des données d'imagerie médicale. Cependant, cette tâche est compliquée et chronophage. Une solution consiste à générer automatiquement les géométries à partir des images du patient. Mais il n'existe pas d'outils automatisés développés précédemment pour reconstruire et personnaliser une géométrie du VG avec des éléments cubiques qui sont plus stables du point de vue mécanique [Lamata et al., 2011].

Récemment, les progrès en échocardiographie quantitative deviennent précieux pour les besoins quotidiens des cliniques [Willenheimer et al., 1997, Kimura et al., 1998, Jensen et al., 2004, Moore et al., 2002, Breitkreutz et al., 2007, Frederiksen et al., 2010], ce qui présente un intérêt commun pour reconstruire les géométries automatiques 3D [Ledesma-Carbayo et al., 2004] et une méthode de référence pour la détection d'anomalies cardiaques. Dans ce contexte, General Electric (*GE*) Healthcare a développé un logiciel intégré (EchoPac®) à sa machine d'imagerie US qui mesure les déformations régionales du VG [Heimdal, 2011] et qui génère un maillage de l'endocarde et de l'épicarde (surface triangulaire fermée) à différents instants du cycle cardiaque. Les données brutes qui ont été utilisée dans la présente thèse ont été fournie par la machine US de Ge Healthcare avec EchoPac® intégré. Néanmoins, il convient de souligner ici que les géométries extraites de ce logiciel sont les données brutes qui doivent être maillées avec les éléments volumétriques pour le logiciel d'FEs (Abaqus®).

Nous avons d'abord étudié le comportement du VG pour une fonction de l'énergie de déformation isotrope (Équation 2.1) puis pour une fonction isotrope transverse (Équation 2.5) pour les paramètres du matériau expérimentalement identifiés en phase diastolique. La géométrie a été fourni par GE Healthcare et par un volontaire sain. Ensuite, nous avons étudié la possibilité d'utiliser les déplacements (générés par la pression sanguine) de l'endocarde pour effectuer des simulations de type Dirichlet. Nous avons comparé ces résultats avec les résultats de simulation

où l'endocarde est sous pression sanguine.

En outre, nous avons développé une méthodologie pour personnaliser le maillage de référence à chaque patient. Ensuite, nous avons validé notre approche en simulant la phase de diastole avec des maillages personnalisés. Enfin, pour chaque patient une valeur de contraction active a été identifiée à la fin de la phase de systole.

Enfin, nous avons développé une subroutine pour le logiciel Abaqus ® afin de simuler la phase de contraction pour un modèle de matériau isotrope transverse. Ce travail est basé sur la littérature et un tel modèle n'existe pas encore dans ce logiciel.

2.1 Heart and its role in cardiovascular system

2.1.1 Anatomy and function

The heart is the first organ in vertebrate embryos which is functional and beats instantly after 4 weeks of development. It begins with the formation of the *primitive heart tube* which later loops and septates into four chambers as in an adult heart [Moorman et al., 2003].

It is a cone-shaped organ with the size of one's clenched fist ($12\times8\times6$ *cm* in length, wide, and thickness, respectively) and capable of pumping 5 litres of blood to the cardiovascular system per minute. The average weight of the heart is sex dependent; for males, it is about 300-350 *grams* and for females, it is approximately 250-300 *grams*. It is placed in the middle *mediastinum* and the front surface sits deep to *sternum* at the level of the thoracic vertebrae. It rests on the diaphragm layer which follows its movements inside the *pericardium* and is slightly offset to the left side (the stronger side) of the thoracic cavity (Figure 2.1). The pericardium is a double membrane sac of tough and dense connective tissue made of an outer lubricated lining *fibrous* layer to protect the heart from infections and an inner serous layer which adheres the pericardium to the heart.

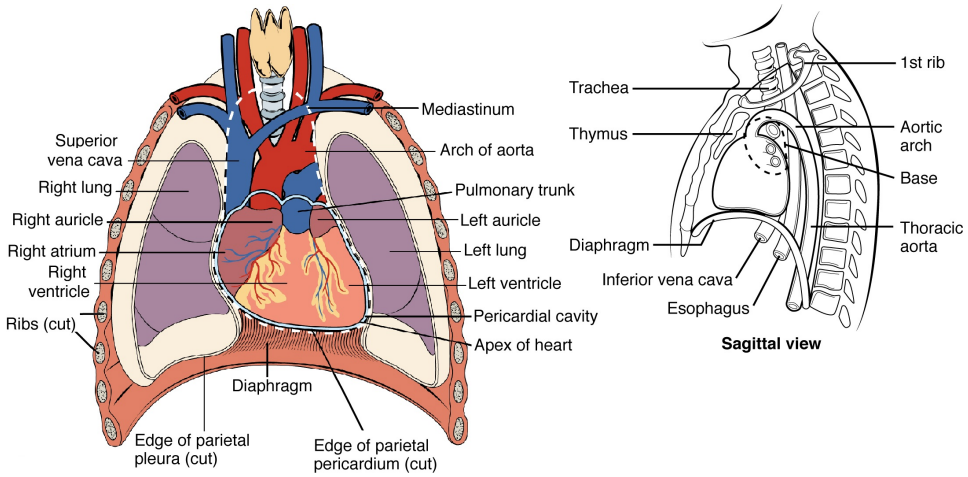

FIGURE 2.1 – The location of the heart in the thoracic cavity and associated anatomical structures. The heart rests on the diaphragm layer which follows its movements and is slightly offset to the left side of thoracic cavity [Betts et al., 2013].

The upper part of the heart called the *base* where the great vein (*venae cavae*) and great arteries (*aorta* and *pulmonary artery*) are attached to it (Figure 2.2.A). The lower part, the *apex*, is pointing to the left side of the body and it is relatively thick in comparison to other

parts. The two main halves of the heart (left and right) are divided by a muscular wall (*septum* from Latin means "something that encloses") which receives and pumps the blood from and to the vascular system. The upper and lower parts of these halves are called the *atria* and the *ventricles*, respectively (Figure 2.2.A).

There are two separate and linked circuits in the cardiovascular structure: the *pulmonary* and *systemic* circuits. These systems transport oxygen and nutrients to the organisms and assists in the removal of the tissue waste products, carbon dioxide and re-oxygenation of the blood through the lungs (Figure 2.2.B). A heart beat is a complete cycle consisting of a contraction (*systole*) and a relaxation (*diastole*) phase.

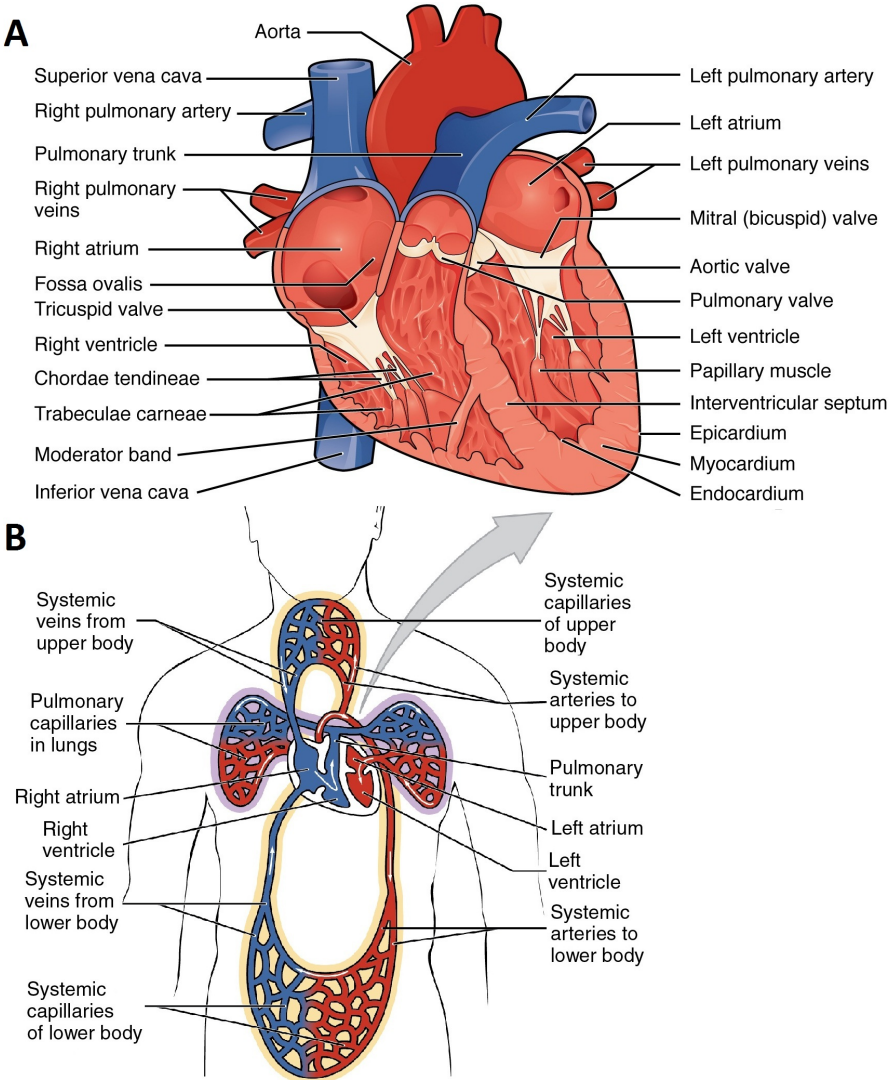

FIGURE 2.2 – The cardiovascular system, composed of the heart (A), as well as arteries and veins (B), as well as detailed anatomical structures. The pulmonary and systemic circuits transport the blood to and from the heart in order to provide cell's basic needs (A and B). Reprinted from [Betts et al., 2013].

Heart Wall Layers

The thickness of the heart chambers depends on their workload in pumping blood to the systemic circulation. As a consequence, the left ventricle (LV) of the heart is stronger and thicker (by about 1 cm) due to its workload (12-16 kPa in average) at systole. The workload on the right side is 3 to 4 fold less because it propels blood to the pulmonary system only, so the wall thickness is half as thick as the left side. The atria act as temporary chambers to receive and push blood from the systemic circulation into the ventricles. They move blood over a short distance and against low resistance so the atrial wall thickness is relatively thin in comparison to the ventricular walls (Figure 2.2.A).

The ventricular tissue is made up of three main layers: the *epicardium* (outer layer consisting of connective tissue of 100 μm), *myocardium* (middle layer and the driving muscle), and *endocardium* (inner thin layer and the interface of the cavity and the intracavital blood pressure of 100 μm) (Figure 2.3). The endocardial surface is also mainly covering the valves and their tendons. The heart has four valves (Figure 2.2.A) which prevent any backflow of blood and they are controlled with pressure changes in the ventricles by *papillary* muscles which are connected to the myocardium (Figure 2.2.A). The oxygen and nutrients for the myocardial layer is supplied by coronary arteries (CAs) to maintain cardiac contraction (Figure 2.3 & 2.2.A) [Betts et al., 2013, Guyton and Hall, 2006].

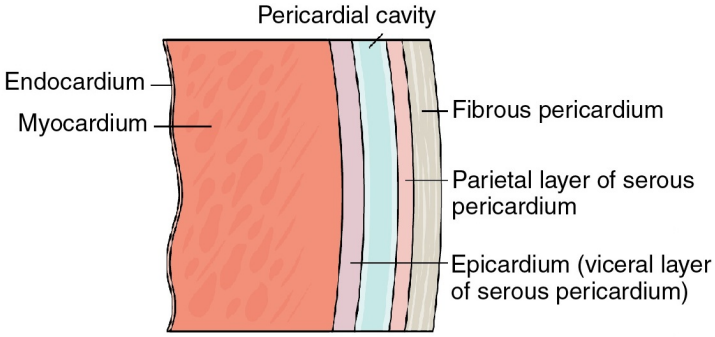

FIGURE 2.3 – The layers of ventricular wall. The driving layer in cardiac contraction is the myocardium [Betts et al., 2013].

Cardiac Electrical Activity and LV Contraction

The systolic phase is the result of an electrical activation pulse released inside the cardiac muscle. This activation is due to a natural pacemaker which regulates the rhythm via a collection of electrical cells named the sinus or sino-atrial (SA) node on the upper side of the right atrium and the atrioventricular (AV) node or junction at the base of the right atrium (Figure 2.4). The SA node has a natural rate of 60 to 100 beats per minute in normal condi-

tions. At the beginning of the systolic phase, an action potential from the SA propagates from the atria and reaches the AV node via the *inter-atrial septum* with a small delay (to prevent overlap in depolarization) at the ventricle's basal part, to trigger the heart contraction.

A micro-structure of muscle fibres (*myocytes*) occupies about 70% of the LV volume. To conduct the electrical pulse from the SA node through myocardium, there are two types of muscle cells, as well as a specialized conduction system: myocardial contractile (the responsible for contraction, 99% of) and myocardial conducting (forming the conduction system, 1% of) cells. Both sympathetic and/or parasympathetic stimulation, which are coupled to the SA node, and hormonal activities, such as adrenaline, tune the activity of the pacing and the contraction frequency. The main pathway from the AV node to the ventricles is the *bundle of His* (named after German physician Wilhelm His, 1863-1934), which branches off into two main bands of conduction pathways (left and right bundle branches) through the right ventricle (RV) and LV, respectively (Figure 2.4). These bands, further, divide into hundreds of tiny nerve/muscle fibrils called *Purkinje* fibers (named after Jan Evangelista Purkinje, 1787-1869) to spread the action potential rapidly throughout the contractile cells (like a network) in the ventricular wall [Betts et al., 2013, Guyton and Hall, 2006, Durrer et al., 1970].

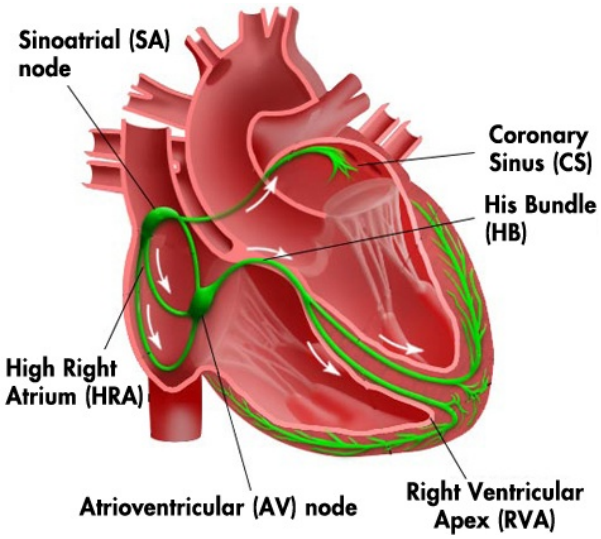

FIGURE 2.4 – Conduction pathways which show the SA and AV nodes and the Purkinje system of the heart. [Jiang et al., 2012].

The heart's electrical activity can be recorded via electrodes on the body surface by electrocardiogram (ECG) tracers (Figure 2.5 & 2.6-ECG curve). The standard placement of electrodes for the 12-lead ECG is on the chest (6 electrodes), limbs (4 electrodes) and arms (2 electrodes).

Three main waves define the ECG captured from these electrodes: 1. *P wave*, due to the atrial depolarisation and contraction (which is hardly detectable), 2. *QRS wave complex* due to the depolarization of ventricles and the main wave, 3. *T wave* due to the repolarisation of the ventricles. There are two segments between these three waves which represent the time delays: 1. The *PR segment*, which is the time for activation of the AV node after the SA node, 2. the *ST segment*, that is, the time between the transition of the fully contracted to the completely relaxed ventricles [Betts et al., 2013, Guyton and Hall, 2006].

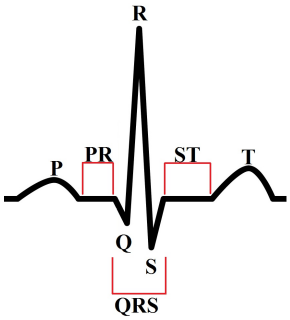

FIGURE 2.5 – Normal ECG and QRS complex. The ECG captures the electrical activity on the body surface as a result of the electrical activity in the heart.

In this thesis, a finite-element (*FE*) setup has been developed for both the systolic and diastolic phases of heart contraction, so it is important here to review the cardiac contraction and relaxation processes and their complex movements briefly. Various quantities such as left atrial, LV and aortic pressure changes, the ventricular volume, the ECG and the *phonocardiogram* (sounds of the heart beat) are shown in Figure 2.6 for the simultaneous cardiac events in the LV. Besides the two main phases (systole and diastole), there are two isovolumic pre-phases right before the beginning of systole and diastole where the ventricles contract and relax with no volume changes. The *isovolumic contraction* is when the ventricular valves are closed while the ventricles are depolarizing and the pressure starts to rise due to muscle contraction. As soon as the pressure reaches a certain level, the valves open and the main phases start [Betts et al., 2013, Guyton and Hall, 2006] (refer to Figure 2.6-pressure curves). The *isovolumic relaxation* happens where the ventricles start to relax and the intracavital pressure drops.

We focus on the cardiac muscle (myocardium) which is quite similar to skeletal muscle in terms of its microstructure. Cardiac muscle fibers are composed of several hundreds to several thousands of parallel arrays of *myofibrils* (Figure 2.7.a). Only 2±5 percent of the myocardium is made of collagen, which is the major protein in connective tissues [Weber, 1989]. Myofibrils

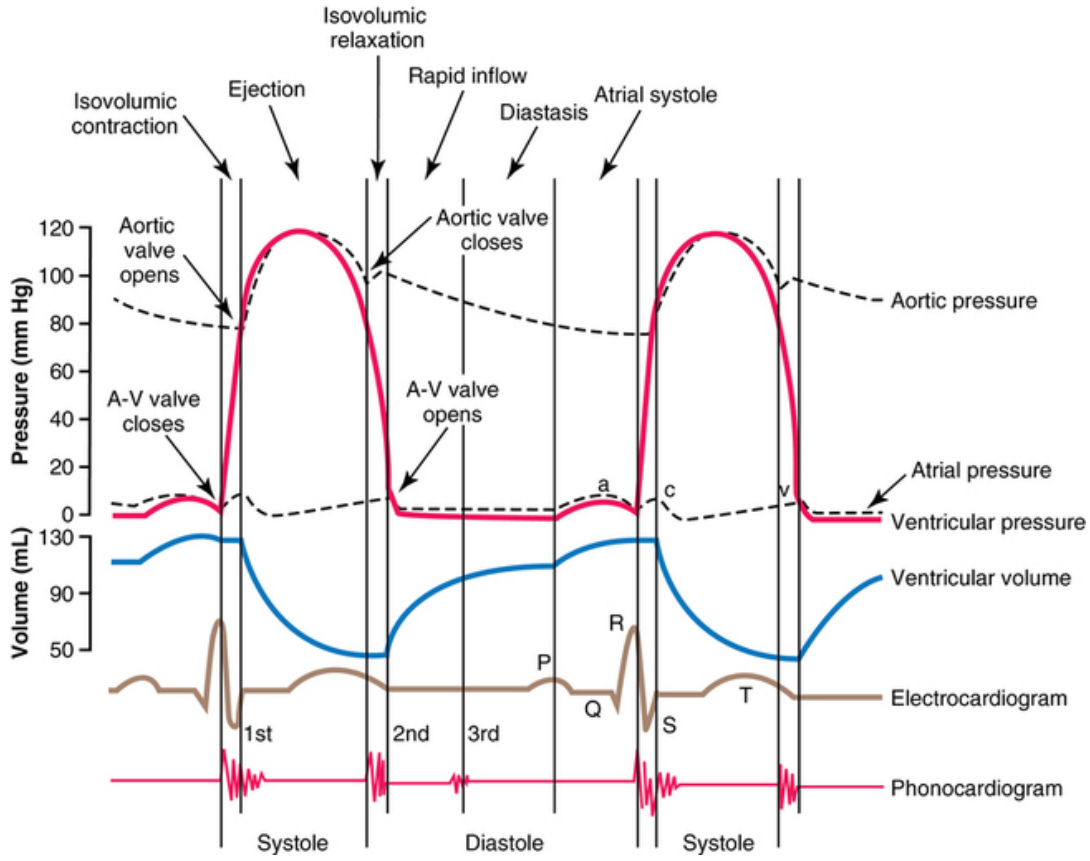

FIGURE 2.6 – The normal cardiac cycle and its measured various quantities. Left atrial, LV and aortic pressure changes, the ventricular volume, the ECG and the phonocardiogram (recorded sounds of the heart) for a normal heart beat is shown [Guyton and Hall, 2006].

are built of thick and thin protein filaments (*myosin* and *actin*) arranged in sarcomeres (Figure 2.7.b) providing the force-generating apparatus. The myosin and actin filaments can be observed with electron microscopy with lighter and darker appearance (I and A bands). These filaments are strongly attached side by side with a protein named *titin*. The I band in a chain of sarcomeres contains a band called the Z disc. The distance between Z discs is called sarcomere length (Figure 2.7.c). An intracellular matrix called the *sarcoplasm*, rich in potassium, magnesium, phosphate, and several enzymes, is holding the myofibrils inside the muscle fibers.

In cell membranes there are several junctions which provide a lower resistance through them (1/400 as compared to the outside membranes) (Figure 2.7.b-c). As a result, calcium ions can spread easily in intracellular fluid from a muscle cell to another one. These main junctions are at the *intercalated discs*, which connect cardiomyocytes and allow the transmission of electrical impulses through the cells to initiate contraction (Figure 2.7.b) as well as stabilize cell connections mechanically. The disc is made of other micro junctional complexes such as: *desmosomes* for cell-cell adhesion, which are resistant to shearing forces, and gap junctions, which is the

intercellular connection gate between muscle cells to permit electrical conduction.

Excitation-Contraction Coupling

Excitation-contraction coupling is a multiscale and multidisciplinary phenomenon. The electrical conduction in cardiac muscle is realised through transverse (T) tubules, placed at the Z disc, from the surface plasma membrane (*sarcolemma*) to the interior of the cell. As soon as the action potential in ventricular muscles is triggered, the sarcoplasmic reticulum releases a large quantity of calcium ions (Ca^{2+}) to the myofibrils and through the cells. As a result, the concentration of calcium ions increases in the intracellular fluid and when a certain threshold is reached, the myosins bind to actin (binds to a complex protein chain named tropnin C) and the cellular contraction begins. The duration of this impulse in cardiac muscle is two folds longer than that in nerve cell or skeletal muscle [Betts et al., 2013, Guyton and Hall, 2006, Netter, 1971], to enable sustained contraction of the heart muscle.

The quantity of blood being pumped by the ventricles indicates how efficient the heart is at working and providing for the demands of the body, particularly, the LV. The contraction output is measured by the ability of the LV to contract from the relaxation phase. It is the fraction of LV end-diastole cavity volume (EDV) to end-systole cavity volume (ESV) and denoted as *Ejection Fraction* (EF) $= \frac{EDV-ESV}{ED} \times 100$. In a normal healthy heart, EF is between $(50-75)\%$ [HRS, 2014].

Fiber Orientation

The microstructure of cardiac muscle has been explained above. It is more complex in macroscale, as the electrical conductivity is greatest along the myocyte axis which causes the LV to twist and rotate during the systolic phase [Nakatani, 2011]. The fiber orientations in the heart were first studied in the late 16^{th} and 17^{th} century by Vesalius (1514), Lower (1669) and Winslow (1714) [Lower, 1932, Winslow, 1711] and later the in 20^{th} century with advances in medical imaging techniques by [Streeter and Bassett, 1966, Torrent-Guasp, 1980, Streeter, 1979, Fernandez-Teran and Hurle, 1982]. Traditionally, the heart has been boiled in acetic acid [Fernandez-Teran and Hurle, 1982] and the atria, epicardium and the subepicardial have been removed, to obtain a rope structure (Figure 2.8) of the fibers with no beginning and no end as it can be observed in skeletal muscle [Torrent-Guasp, 1980].

Later, Streeter and coworkers identified the muscle myofilaments in the cell with the fiber direction using light microscopy with $400\times$ magnification [Streeter and Bassett, 1966, Streeter,

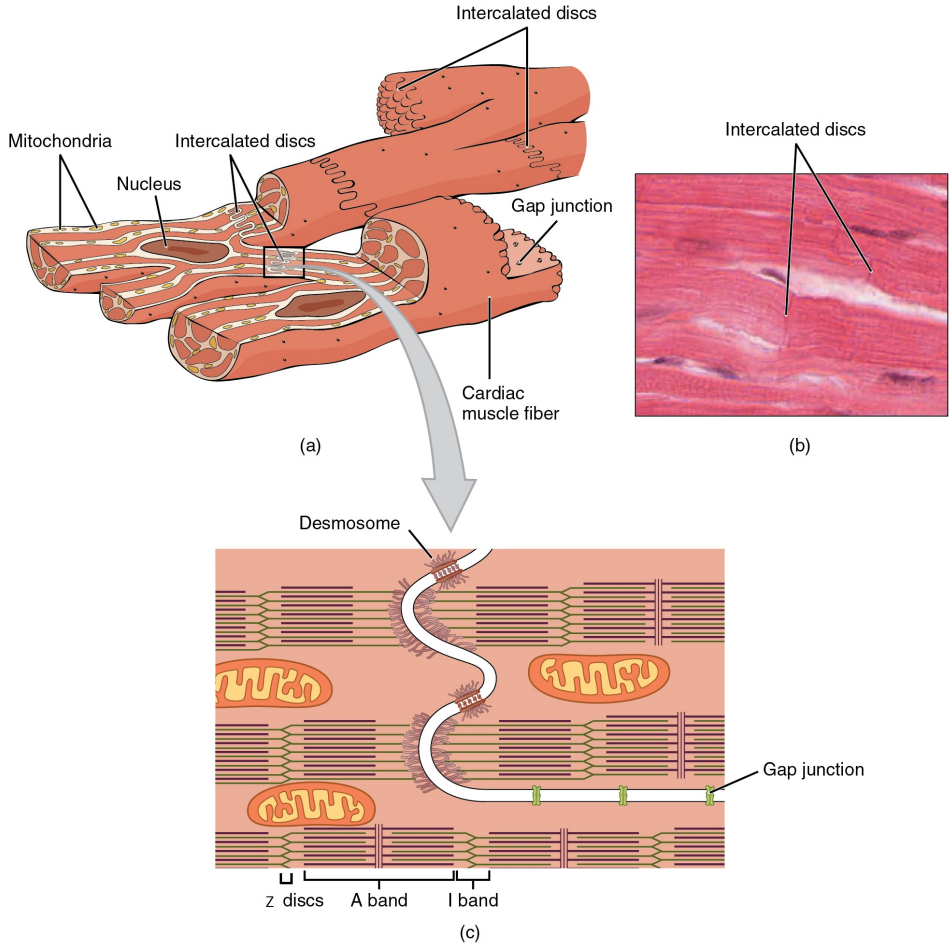

FIGURE 2.7 – (a) Cardiac muscle fiber structure. (b) Intercalated discs. (c) Magnified myofibril with A and I bands, and Z discs in sarcomere structure. Copyright to Regents of the University of Michigan Medical School © 2012.

1979, Streeter et al., 1969]. They suggested that the LV is a cross-linked, fibrous elipsoidal, pressured vessel with fiber directions smoothly changing from 60° on the endocardium to -60° on the epicardium. It has been observed that there is a constant increase in the fiber angle from the diastolic relaxation to the systolic contracted phase and also that the fiber orientation is different in transition between these phases at the equatorial plane.

The cardiac fiber structure, following observations of Streeter and coworkers, was considered to be a unified muscle (rope shape) which had some variations in direction throughout the heart wall layer. However, LeGrice and coworkers later investigated the idea of a discrete architecture of cardiac muscle tissue from the arrested canine heart. The heart was arrested at the diastolic phase and cut along meridians to be analysed by electron microscopy. They observed that the longitudinal-transmural sections are built of layers varying through ventricular wall. They suggested a local fiber coordinate system where the fiber, sheet, and sheet-normal axes are along

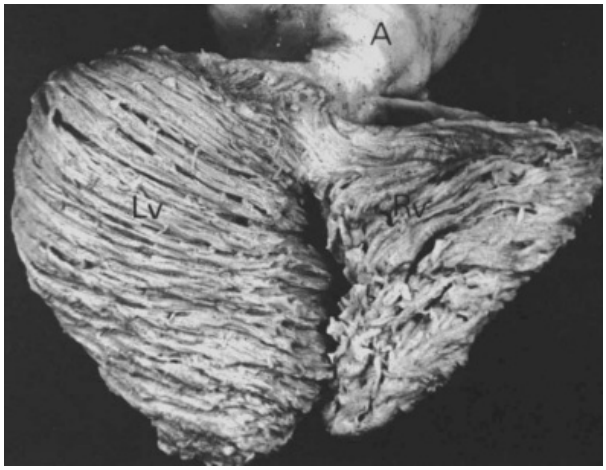

FIGURE 2.8 – Diaphragmatic view of the middle layer of the ventricles. This LV belonged to a 55-year old female, which rested in formaldehyde solution for 30 days and was then boiled in acidulated water with acetic acid [Fernandez-Teran and Hurle, 1982].

the muscle fiber, transverse to the muscle fiber (in plane), and perpendicular to the plane of sheet and fiber, respectively. Later, research from LeGrice and coworkers shows that the cleavage planes in the ventricular wall permit lateral movements of muscle layers, and so this allows the rearrangements of muscle fibers in different cardiac phases [LeGrice et al., 1995a, LeGrice et al., 1995b]. These histological studies provided a good understanding of cardiac fiber structure. However, this complex architecture is still under investigation, particularly, to determine the degree of anisotropy of discrete fiber orientations for each individual. The debate is ongoing whether the heart is a single muscle in a helical pattern or it is rather a continual muscle of laminar sheets.

However, the presented histological studies for defining fiber orientation structure have been done on the arrested canine heart or provided from human cadavers. In the last decades, the medical imaging advances in magnetic resonance imagining (*MRI*), especially, after developing methods like the diffusion tensor for MRI (*DTMRI*) modality, opened more possible solutions for personalised in-vivo measurements of fiber orientations in the human heart [Vetter and McCulloch, 1998, Hsu et al., 1998, Scollan et al., 1998, Scollan et al., 2000, Chen et al., 2003, Burton et al., 2006, Seemann et al., 2006, Hooks et al., 2007, Li et al., 2008b, Lombaert et al., 2011]. The diffusion of water molecules is more rapid in the preferred internal structural orientation (along the fiber) than in the perpendicular direction. DTMRI allows mapping this water diffusion in fibrous structures, such as cardiac muscle, in-vivo and non-invasively [Le Bihan and Breton, 1985].

In Figure 2.9, we can observe the variation of fiber orientations through the myocardial wall

thickness that can be obtained from DTMRI [Hsu et al., 1998]. The analysed fiber orientations in mammalian hearts such as humans, dogs, macaques, pigs, and rats were experimentally determined from about -60° to -70° clockwise from the circumferential axis at the epicardium to about +60° to +70° at the endocardium, where at mid layer it is 0° and parallel to the circumferential direction. [Pearlman et al., 1982, Streeter et al., 1978, Streeter and Hanna, 1973, Ross and Streeter Jr, 1975, Streeter and Bassett, 1966, Hort, 1960, Omens et al., 1991, Vetter and McCulloch, 1998, Nash and Hunter, 2000].

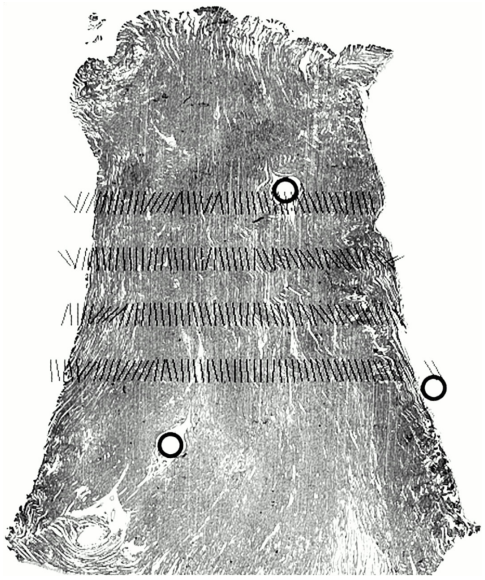

FIGURE 2.9 – Registered image of histological sections (4.5 mm depth from epicardium layer) with fiber directions in black lines from DTMRI [Hsu et al., 1998]. The black circles are the registration markers.

2.1.2 LV related pathologies

In 2012, the World Health Organisation announced that *cardiovascular diseases* killed 17.5 million people in the world (Figure 2.10). Of these, 7.4 million people died of *ischaemic heart* diseases which have been increasing in global burden trend since 2000 [WHO, 2012]. This increasing trend motivated the health authorities to take action and dedicate more budget to cardiovascular disease research in order to provide effective understanding and to develop new treatments. This Section will review several main causes of cardiac insufficiencies which directly impact myocardial tissue or ventricular movement. These have furthermore been analysed from a mechanical point of view in Chapter 3 and 4.

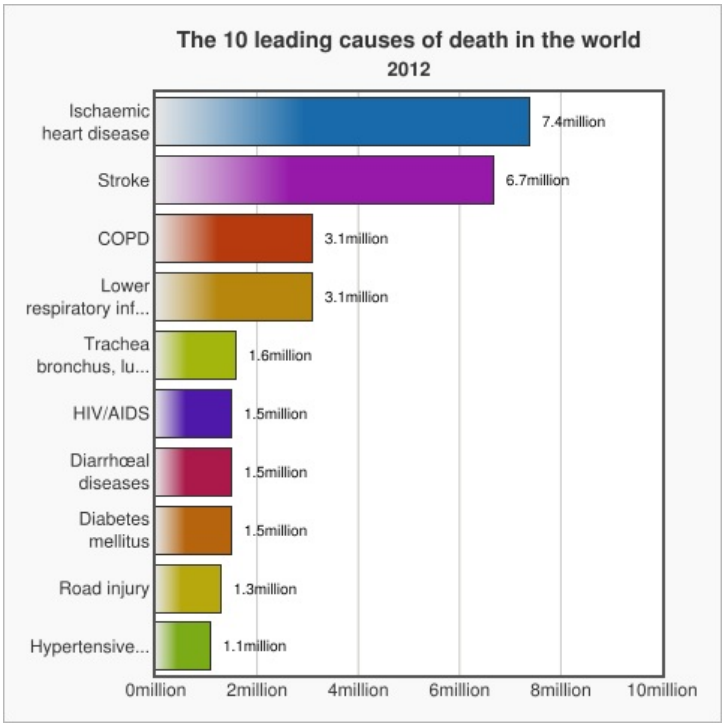

FIGURE 2.10 – The top 10 causes of death in the world. The ischemic heart diseases are the first cause of death in the world [WHO, 2012].

Ischaemic Heart and Myocardial Infarction

Ischaemic heart diseases are due to a lack of blood supply to bring oxygen and nutrition to the ventricles and occur in a time-dependent manner. The LV is primarily affected in this condition due to its complex workload. Ischaemia can be due to atherosclerosis, narrowing or blockage of the CAs. Atherosclerosis occurs when fatty deposits (*plaques*) start to build up on the artery walls so these become thick and stiff. It can happen in any artery in the body but when it comes to the LV, its consequences can be mortal. In the worst case -blockage of CAs

(*Angina*)-, it can produce myocardial infarction (*MI*), stroke, cardiogenic shock, mitral valve dysfunction, aneurysms, cardiac rupture, chamber arrhythmias, AV and SA nodes dysfunction, thrombosis and emboli in the central nervous system, mitral regurgitation, pericarditis, RV infarction, and depression [Mullasari et al., 2011, Grasso and Brener, 2014].

In 2013, about 8.6 million MIs occurred in the world [Vos et al., 2015]. The atherosclerosis, emboli and spasm of CAs are the main causes of MI due to the tissue death from lack of blood flow (Figure 2.11). The main symptoms are angina pectoris (sensation of tightness and pressure in the chest) and dyspea (shortness of breath). The body systems can manage to respond to the MI by progressive organisation of dead myocytes and capillary in growth so the infarct zone starts to shrink even in the early stage (0-24 hours). The complications increase in cases where the blockage of CAs continues, which causes pericardial inflammation (1-3 days), myocardial (lateral or septum wall) or papillary muscle rupture or ventricular aneurysm and ballooning of the heart chambers due to the weakened wall (3-14 days) and ends in LV remodelling and heart failure (after 2 weeks) [Grasso and Brener, 2014, Becker et al., 1996].

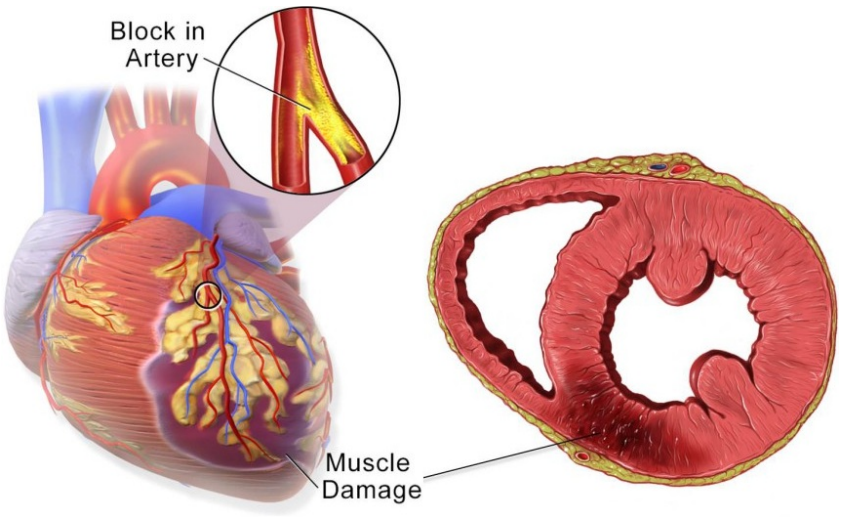

FIGURE 2.11 – MI due to a CA blockage [Lynch, 2000], leading to cell death and tissue damage.

MI is not necessary fatal, especially if medical attention and treatment dealt with the blockage soon after the heart attack, but it is likely to result in a damaged heart, impaired LV filling, acute atrial enlargement and later heart attack. MI, according to its severity, can be divided into two main groups: Non ST segment Elevated Myocardial Infarction (*NSTEMI*) where the CA is partially blocked and ST segment Elevation Myocardial Infarction (*STEMI*) where the CA is completely blocked and the muscle tissue starts to become necrotic. As soon as the first symptoms appear, an electrocardiogram should be obtained. Patients with raised

ST segment and signs of left bundle branch block (*LBBB*) are considered as STEMI and the strategy is to undergo medical therapy with aspirin (inhibits the formation of blood clots), heparin, nitrates (to dilate blood vessels), and beta-blockers (to decrease heart rate) or in particular cases undergo a *coronary revascularisation* therapy (vascular bypass and angioplasty) which also improves the EF and significantly reduces mortality.

Cardiomyopathy

Cardiomyopathy (*CMP*) is a condition wherein, for any reason, the heart muscle is incompetent with respect to contraction. It can be a mutation of genes or acquired during an individual lifetime due to another disease, persistence to compensatory responses, stress, diabetes, cardiac muscle infection, pregnancy and alcohol. Often, it is difficult to characterize this pathology, due to the complex protein structures in myocardial muscle, the presence of disease-causing mutations, and other triggers which weaken the heart muscle.

The World Health Organisation described this pathology in five main groups (Figure 2.12): 1. *Hypertrophic*: increase in wall mass and septal wall asymmetric thickening due to an increase in cardiomyocyte size, perivascular and interstitial fibrosis (Figure 2.12.B), 2. *Dilated*: reduction in wall thickness (mass) and enlargement of the cavities under blood pressure which is highly correlated with a mortality of 50% death within five years (Figure 2.12.C), 3. *Restrictive*: response and regulation of actin-myosin (calcium-mediated) interactions, sarcomeric proteins and contractibility to environmental stimuli caused by radiation, secondary effects after heart surgery, muscle infection and amyloidosis. It often leads to increase in stiffness of the myocardial wall and in pressure in the ventricular cavities, 4. *Arrhythmogenic RV*: reduction in the stability of the desmosomal complex at junctions between cardiomyocytes, which coordinates contractile activities at the cell level. It leads to replacement of cardiomyocytes by fibrotic and adipose tissue, primarily in the RV, and 5. *Unclassified groups*: such as noncompaction CMP (Figure 2.12.D), which results in a spongiform appearance of the myocardial walls. The responsible cellular and environmental trigger mechanisms are poorly identified and this has often been related to the malformation of the heart structure during the 5^{th} and 8^{th} weeks of embryonic development [Harvey and Leinwand, 2011, Michels et al., 1992, Grogan et al., 1995, Kamisago et al., 2000, Peddy et al., 2006, Mogensen et al., 2003, Karam et al., 2008, Parvatiyar et al., 2010, Corrado et al., 1997, Yamaji et al., 2005, Yang et al., 2006, Yousef et al., 2009].

The remarkable advances in histological studies and cellular responses to CMP have allowed therapeutic drug developments which decrease blood pressure and heart rate, to reduce

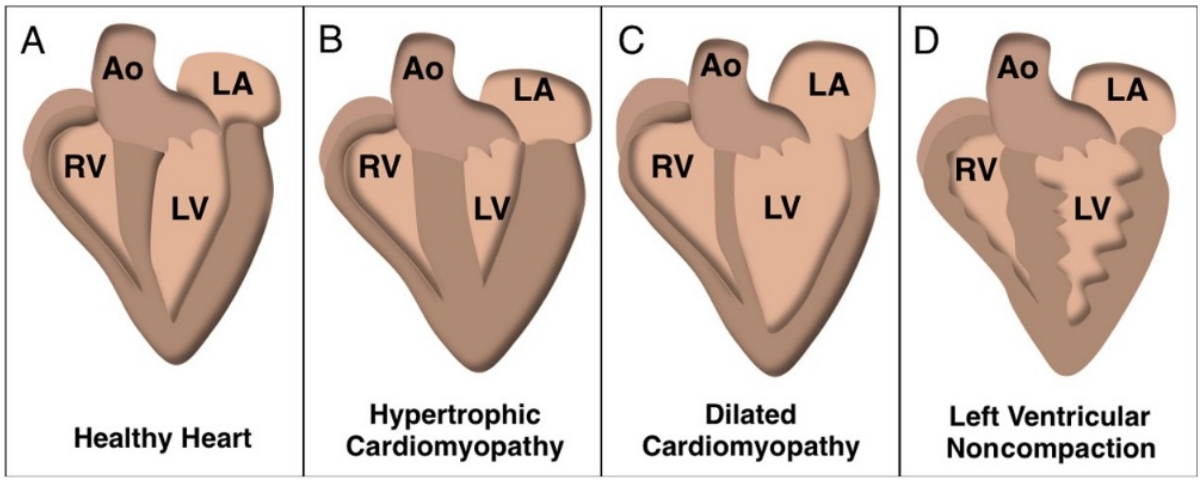

FIGURE 2.12 – An illustration of CMP types: A, Normal heart. B, Hypertrophic CMP with septum, posteriori and apex wall hyperothropy. C, Dilated CMP with wall thinning and enlarged LV and atria cavity volumes. D, abnormally trabeculated heart chambers (spongiform) [Harvey and Leinwand, 2011].

wall deformation. These include angiotensin II receptor antagonists and Ca^{2+} channel blockers. Implantable devices to regulate the chamber's contraction may also be used to reduce the progression of CMP [Rose et al., 2001]. However, there are no direct treatments for inherited CMPs, to address the cause rather than the reduction of symptoms, which include heart failure and mortality [Harvey and Leinwand, 2011].

LBBB

LBBB is a condition wherein the activation of the LV through the left bundle branch (Figure 2.4) is much delayed compared to that of the RV chamber and septal wall. The generated primary pressure from septal contraction increases the load on the lateral wall in addition to the blood pressure. As a result, the lateral wall must work harder than the septal wall to overcome such a workload, and it gradually becomes thicker. Statistically, 40% of patients with dilated CMP and congestive heart failure (*CHF*) have unsynchronized ventricular contraction. This remodelling of tissue (lateral wall) compared to the septal wall thickness can be seen in medical images as the pathology advances [Sugihara et al., 1997, Kasai et al., 2004, Mahrholdt et al., 2005].

In addition to detection by medical imaging, this contraction disorder is also visible in ECG clinical tests as a wide QRS complex. An efficient management of this pathology is cardiac resynchronization therapy (*CRT*). It involves a simultaneous pacing from a half dollar pacemaker that constantly monitors the patient's heartbeat and corrects this electrical delay by a tiny

electrical charge to result in a narrower (or normal) QRS complex [Shea and Sweeney, 2003]. Other possible treatments include medication which strengthens the heart muscle contraction and simplifies the heart's workload by relaxing blood vessels to reduce the resistance to blood pumping.

Ischaemic heart diseases and MI can also lead to abnormal conduction interfaces at the injured and border zones. Unfortunately, patients with MI and LBBB have a higher in-hospital death rate (34%) compared to patients with no bundle branch block or ST segment elevation [Go et al., 1998, Hamby et al., 1983].

In this Section, we reviewed heart function and several causes which lead to cardiac dysfunction. These pathologies have been studied in our FE setup to analyse myocardial behaviour, especially, for LBBB patients. MI and CMP are the associated pathologies of the LBBB patients that were obtained from medical imaging techniques (US). It has been also emphasized that the early detection of these pathologies is vital to reduce myocardial damage and the mortality of a patient. The next Section will introduce the myocardial behaviour from a mechanical point of view.

2.2 Constitutive modelling of passive myocardium

In order to quantify tissue deformation (*strain*) and associated forces (*stress*), it is necessary to briefly describe some concepts in material mechanics. The ability of a material specimen to regain its initial shape after application and removal of external forces is explained by elasticity theory. Robert Hook (1678), first identified the relationship (*constitutive equation*) between stress and strain in an elastic material body, and it is known as Hooke's law [Williams, 1956]. Later, experimental tests and development of constitutive assumptions resulted in deriving several so-called hyperelastic constitutive models which explain biological tissue behaviour as well [Fung, 1967,Ogden, 1984,Beatty, 1987,Macosko and Rheology, 1994,Ogden, 1997,Holzapfel, 2000, Holzapfel, 2002]. A common constitutive equation to explain the material behaviour is a strain energy density function (ψ). Several mechanical quantities derive from the strain energy equation, which can be a linear or nonlinear function describing material behaviour. In this Section, we offer an overview of several common strain energy functions to explain myocardial behaviour.

It has been mentioned before that the myocardium's behaviour is dependent on the fiber direction (means that the tissue is *anisotropic*). Understanding of such multiscale structure of cardiac function, from cell to the whole organ, requires a precise knowledge of material properties. Underling ventricular mechanics were not investigated using finite elasticity theory and suffered from the shortage of three dimensional (*3D*) constitutive equations until the late 20^{th} century by the work of Demiray [Demiray, 1976]. He proposed an isotropic model for myocardium by considering an idealized spherical geometry. This isotropic model improved to an isotropic transverse approach in the 1990s [Humphrey and Yin, 1987, Humphrey et al., 1990, Guccione et al., 1991, Costa et al., 1996] and later to orthotropic models [Usyk et al., 2000, Schmid et al., 2009, Holzapfel and Ogden, 2009, Pezzuto et al., 2014]. They often contain four to eight parameters to identify experimentally.

In this context, the biaxial response of a myocardial specimen is limited for describing passive transversely isotropic behaviour [Demer and Yin, 1983, Yin et al., 1987, Smaill and Hunter, 1991] whereas later shear tests conducted on myocardial specimens showed more orthotropic comportment [Dokos et al., 2002]. In Figure 2.13, the shear behaviour of myocardial tissue is shown in different directions. The tissue is more resistant to shear deformations and highly nonlinear in extension of the fiber directions (fs and fn). It has been also emphasized in the literature that the myocardium is 1.5 to 3 times stiffer in the fiber direction than in the sheet

and normal to fiber-sheet plane directions [Humphrey et al., 1990, Yin et al., 1987]. The other shear planes show lower nonlinearities, but they remain different. However, the planes with the extensions of normal to fiber-sheet planes (nf, ns) are the same and quasi-linear.

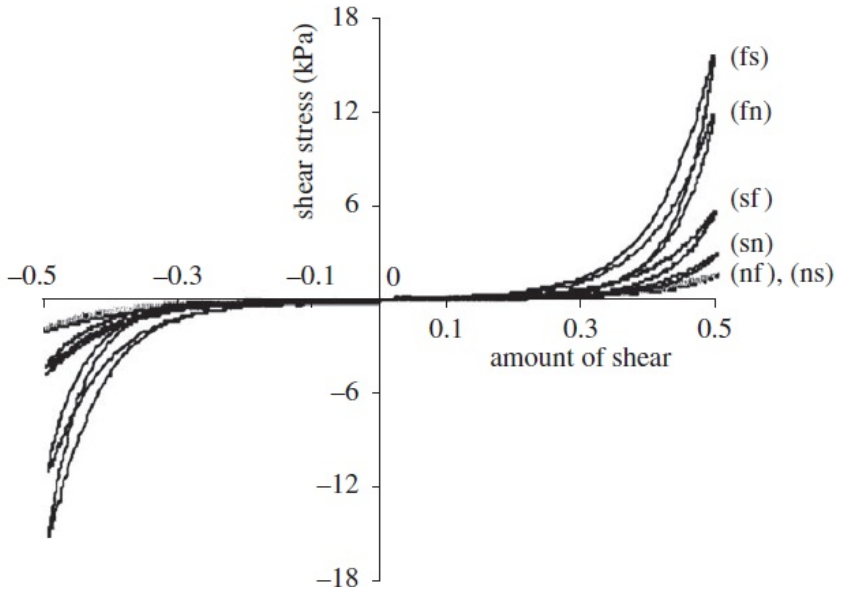

FIGURE 2.13 – This figure shows the shear stress responses of specimen to different amounts of shear [Dokos et al., 2002]. (f,s,n) stand for fiber, sheet, and normal to fiber-sheet plane, respectively.

This complex nonlinear behaviour of the myocardium is mostly expressed as an exponential or polynomial function and many of these models are based on a transverse isotropy assumption. Here, two widely used strain energy functions are introduced. [Guccione et al., 1991] proposed a Fung-type strain energy function (ψ) based on the Green-Lagrange strain tensor ($\mathbf{E}$) components, given as:

$$\psi = \frac{1}{2}c(exp(Q) - 1), \tag{2.1}$$

where

$$Q = b_3E_{ff}^2 + b_2(E_{ss}^2 + E_{nn}^2 + 2E_{sn}^2) + b_1(2E_{fs}^2 + 2E_{fn}^2), \tag{2.2}$$

where b_{ij} and c are the material parameters (MPs) to identify in an experimental test. Here, (f,s,n) stand for fiber, sheet, and normal to fiber-sheet plane directions.

This model has been widely used in MPs identification. However, the identified parameters are often different due to the experimental setup, loading conditions, identification method and given animal sample [Wang et al., 2013, Yettram and Beecham, 1998, Périé et al., 2013]. The change in tissue properties after death in in-vitro tests may not be an accurate estimation of

in-vivo myocardial properties. In addition, the parameters are highly coupled, which is very difficult to interpret. We will review these MPs in Chapter 2.

The second proposed strain energy function is the [Holzapfel and Ogden, 2009] model which expresses the collagen fiber contribution in myocardium as an orthotropic material (Equation 2.3). The authors considered three exponential terms to express the stiffening behaviour in the muscle fiber direction, the stiffening in the sheet direction associated with the collagen fibers, and the contribution of fiber shear planes in order to model the tension/compression behaviour of the material. In addition, the authors ensure that the use of invariants of tensors makes the model geometry independent and the only requirement will be the material preferred directions (which reduces the sensitivity to the MPs).

$$\psi = \frac{a}{2b} exp[b(I_1 - 3)] + \sum_{i=f,s} \frac{a_i}{2b_i}(exp[b_i(I_{4i} - 1)^2] - 1) + \frac{a_{fs}}{2b_{fs}}[exp(b_{fs}I_{8\,fs}^2) - 1]. \tag{2.3}$$

where

$$\begin{aligned} I_1 &= tr\mathbf{C}, \mathbf{C} = \mathbf{F}^T\mathbf{F}, \\ I_4 &= \vec{\mathbf{e}}_1.(\mathbf{C}\vec{\mathbf{e}}_1), \\ I_8 &= \vec{\mathbf{e}}_1.(\mathbf{C}\vec{\mathbf{e}}_2). \end{aligned} \tag{2.4}$$

where $a, b, a_f, a_s, b_f, b_s, a_{fs}$ and b_{fs} are material constants (positive values), the a parameters are having unit of stress and b parameters are dimensionless, $\mathbf{C}$ is the right Cauchy-Green tensor, $\mathbf{F}$ is the deformation gradient tensor, and $\vec{\mathbf{e}}_{1,2}$ are unit vectors in the preferred material directions (that can be fiber or sheet direction), introducing the anisotropy.

The third proposed strain energy function aims to reduce the complexity of cardiomyocyte contraction by considering the myocardium as an isotropic material. The isotropic strain energy functions have been also used in the literature to ease numerical simulations [Janz and Grimm, 1972, Bogen et al., 1980]. One example of such isotropic models is the work of [Marchesseau et al., 2013a]. They have identified the MPs for a Mooney-Rivlin strain energy function in an electromechanical simulation by customizing a healthy subject's heart to MRI images. They consider myocardium as quasi incompressible tissue; therefore, a volumetric part should be considered in the strain energy function as:

$$\psi = c_1(\bar{I}_1 - 3) + c_2(\bar{I}_2 - 3) + \frac{K}{2}(J - 1)^2. \tag{2.5}$$

where

$$
\begin{aligned}
&J = Det(\mathbf{F}),\\
&\bar{I}_1 = J^{-2/3} I_1,\\
&\bar{I}_2 = J^{-4/3} I_2, I_2 = \frac{1}{2}((tr\mathbf{C})^2 - tr\mathbf{C}^2).
\end{aligned}
\tag{2.6}
$$

where c_1, c_2 are the MPs having dimension of stress, J is the determinant of the deformation gradient, $\bar{I}_i$ are the isochoric invariants of the right Cauchy-Green tensor and K is the bulk modulus which represents the volumetric variation of the tissue with respect to pressure.

One difference between the strain energy functions in Equations 2.1 & 2.3 and Equation 2.5 is the assumption of incompressibility for cardiac tissue. A topic of debate is whether the myocardium should be considered a fully or quasi incompressible material. The fully incompressibility (Poisson's ratio $\nu = 0.5$) is established in the work of Vossoughi and coworkers by applying different hydrostatic pressures to a myocardial specimen [Vossoughi et al., 1980]. In contrast, Yin and coworkers concluded that perfused myocardium is compressible due to the displacement of blood in intra/extra-vascular during the systolic phase [Yin et al., 1996]. Tracing the evolution of LV tissue during a cardiac cycle in medical imaging techniques showed that the volume changes are no more than 4% [Vergroesen et al., 1987, Hoffman and Spaan, 1990, Judd and Levy, 1991, Liu et al., 1992], so the tissue can be quantified to be slightly compressible. The compressibility assumption appears in the strain energy function as a volumetric equation which contains the bulk modulus K, as shown in Equation 2.5.

The precise value of the bulk modulus for cardiac FE simulations is very important, as it improves the accuracy of a simulation's results. This value has been identified in a wide range in the literature during the relaxation phase (28 & 160 kPa) [Bettendorff-Bakman et al., 2006, Veress et al., 2005] and the contraction phase (380 & 600 kPa and 25 MPa) [Shim et al., 2012, Dorri et al., 2006, Marchesseau et al., 2013b]. It has been shown that this parameter varies for different pressure-volume curves and EF [Hassaballah et al., 2013]. In hypertrophic ventricle and cardiac amyloidosis, this parameter can increase up to ~ 3 GPa [Masugata et al., 2000].

Another mechanical property of myocardial tissue is that the unloaded myocardium is residually stressed. It is subjected to residual stresses as the organ grows during the embryo's development and these stresses are present during a lifetime in the healthy heart. The existence of these residual stresses have been proved experimentally from potassium-arrested rat heart and numerically from an open cylinder [Omens and Fung, 1990, Guccione et al., 1991]. At the macro scale, the endocardial and epicardial layers have been shown to be under compressive

and tensile residual stresses, respectively, in the circumferential direction. At the micro scale, the fiber and laminar myocardial sheet structure appears to bear these stresses in the myocardial midwall [Costa et al., 1997]. They may vary during the remodelling and growth in different pathology cases [Rodriguez et al., 1993,Rodriguez et al., 1994]. Incorporating this property into the constitutive formulations is a very complex problem and needs to be studied further for numerical simulations. However, other geometrical optimisations which are relatively simple to implement can help to reconstruct these 3D stresses at a certain precision [Riveros et al., 2013].

In this Section, we discussed the mechanical properties of myocardial tissue. Different proposed strain energy functions have been reviewed from available literature to explain myocardial nonlinear behaviour. The strain energy function is a part of a FE setup for cardiac simulation; the next natural step is to define the FE method. The next Section will review the available methods for computational modelling of the LV.

2.3 FE methods for LV simulation

FE simulations have shown great promise in heart function investigations for clinical purposes. A description of each event involved in a cardiac cycle has to deal with a complex coupling of multiphysics simulations, such as electricity, physical chemistry, solid mechanics, and fluid dynamics. In order to accurately model this series of events, excitation-contraction coupling of the myocyte, propagation of the action potential and relaxation of the human LV should all be taken into the account. However, incorporating all these phenomena is computationally expensive and very complex to implement, resulting in a variety of approaches. FE methods for cardiac simulations is a very wide area with incorporated complex multiphysics phenomena. Here, several methods for cardiac FE analysis, such as electromechanics simulation, active stress generation methods for contraction phase, and fluid-structure interaction simulations, are briefly discussed.

A method to model ventricular behaviour numerically is by electromechanical simulation. These models couple the electrophysiology and mechanical behaviours to reproduce a cardiac cycle [Humphrey et al., 1990, Hunter et al., 1997, Nash, 1998, Nash and Panfilov, 2004, Panfilov et al., 2007]. The available electromechanics models often differ in the choice of hyperelastic strain energy function, cell electrophysiology/mechanics and hemodynamic equations. A complete electromechanical model is shown in Figure 2.14. Generally, the total Cauchy stress is the sum of active and passive parallel components, where the active contraction stress is derived from several other control parameters along the sarcomere direction and the passive stress is the reaction of elastic bounds (titin) to active contractions from the strain energy function.

A method to generate active tension is to add a time varying stress (Figure 2.14) calculated from a cell model to the myocyte component of passive Cauchy stress tensor [Niederer and Smith, 2009, Vendelin et al., 2002, Hunter et al., 1998, Nash and Hunter, 2000]. Several active tension cell models have been developed in the literature [Bovendeerd, 1990, Guccione and McCulloch, 1993, Sachse, 2004], such as a simple linear model for active stress [Linge et al., 2005] or the more complex and advanced Hunter-McCulloch-terKeurs (HMT) model [Hunter et al., 1998]. The HMT model incorporates several chemical events at the cell scale during myocyte contraction. It contains the extracellular calcium concentration Ca^{2+}, the binding of Ca^{2+} to troponin C and its relaxation process, and so on. Normally, this active force is generated by an electrical wave propagated throughout the FE domain to the contract element in the fiber direction [Sermesant et al., 2001].

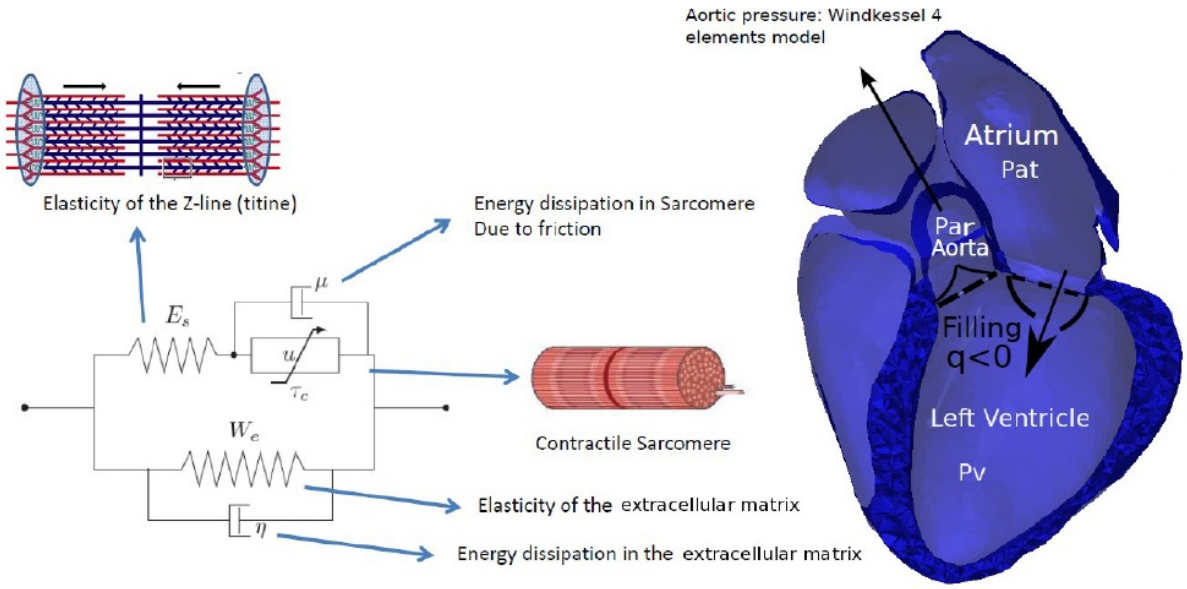

FIGURE 2.14 – Full electromechanical model including blood circulation system. Here, W_e is the strain energy of extracellular matrix with a dissipative term (η), u is the control parameter for contraction τ, μ is the friction in sarcomeres and E_s is to enforce elasticity of titin as a linear spring [Marchesseau et al., 2013a].

In addition, we can add other components in the principal directions (sheet and normal to fiber-sheet plane) to the active stress tensor. It has been shown that the active stresses in the fiber transverse direction (diagonal components) can be expressed as a function of fiber active Cauchy stress and 20% to 60% of its range [Lin and Yin, 1998, Mazhari and McCulloch, 1999, Usyk et al., 2000, Usyk and McCulloch, 2003].

Interaction of blood flow and the myocardium in the ventricles is considered a fluid-structure problem which has been investigated in the contraction and relaxation phases for in-vitro animal sample or simple tissue models. The fluid-structure coupling was described by [Peskin and McQueen, 1997, Kovács et al., 2001, Domenichini et al., 2005] for the filling phase of the LV. They considered the muscle fibers in the Lagrangian description by discretizing them very finely so that these contain no mass and volume for a continuum mechanical description of the tissue. Their equations of fluid mechanics were driven from Navier Stokes formulations in an Arbitrary Lagrangian Eulerian (ALE) framework for non-Newtonian blood properties. The complexity of hemodynamic flows often cause large distortion of the Lagrangian frame; therefore, it is more convenient to use a general ALE which is basically the derivatives with respect to the fixed coordinates [Nordsletten et al., 2011]. Furthermore, Lemmon and Yoganathan developed this model and applied it to an idealized LV during the diastolic phase. The authors examined

the validity and reliability of this model to pathological cases and their obtained results were promising for detection of ventricular dysfunction [Lemmon and Yoganathan, 2000a, Lemmon and Yoganathan, 2000b].

A frequently used hemodynamic framework is *KaHMo* (Karlsruhe Heart Model) which is used in fluid-structure interaction and muscular dynamics studies of LV [Doenst et al., 2009, Oertel and Krittian, 2011, Schenkel et al., 2009]. The KaHMo geometry is the endocardial layer of the LV obtained from MRI images through a cardiac cycle. A numerical simulation of a patient-specific intracavital flow in KaHMo is shown in Figure 2.15. The advances of these FE methods are very promising for treatments of different pathologies and Ventricular Assist Devices (*VAD*) applications.

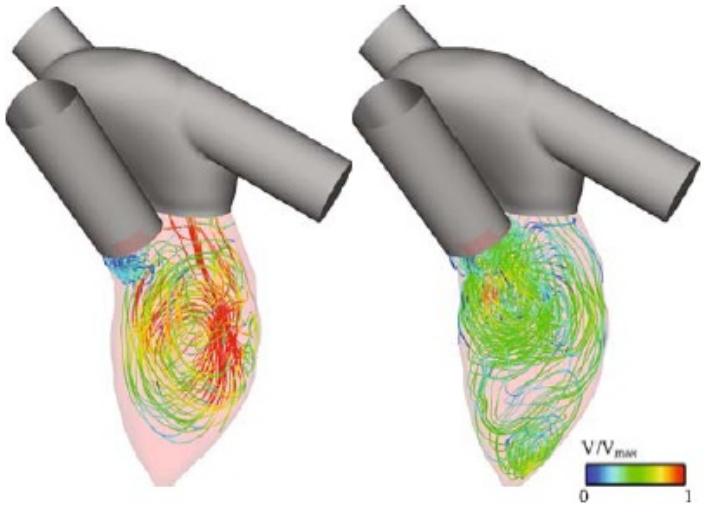

FIGURE 2.15 – KaHMo numerical simulation of flow structure in a healthy LV showing the velocity magnitude streamlines [Perschall et al., 2009].

As mentioned previously in this Section, incorporating all complex mechanical interactions for cardiac FE simulation is computationally expensive. Some assumptions should be taken into account in order to reduce the compute time and to enable real-time, clinically relevant, patient-specific simulations.

2.4 Toward LV automatic FE mesh generation

The first steps to define a FE setup have been explained in the last Sections. Each individual's LV differs in its material properties and geometry due to the size, gender, genetic disorders and so on. Therefore, a general FE setup may not describe the individual's LV mechanical behaviour sufficiently. In this situation, a *patient-specific* FE simulation which fulfils these requirements and customizes a FE setup in order to match to patient data becomes essential. This is possible by using the extracted movements of the geometry to identify the material parameters of the strain energy function and to perform FE simulation with the patient's own geometry from medical images.

The influence of geometry in the mechanical responses of patient-specific simulation has been studied previously [Miller and Lu, 2013, Mayeur et al., 2016, Joldes et al., 2016]. It has been shown that isotropic material models are insensitive to their MPs but coupled strongly to the FE geometry and wall thickness. However, the low resolution of clinical daily routine imaging modalities does not result in an accurate mechanical response due to their influences on the meshing algorithm's efficiency,. The advances in MRI imaging techniques seem very promising with respect to a precise acquisition of the human organ with high spatial resolution [Zerhouni et al., 1988, Axel and Dougherty, 1989, Pelc et al., 1991, Kim et al., 2004]. However, their routine use are limited due to the high expense and poor availability for clinical application, complexity method of acquisitions, the time consuming image processing and lack of direct automatic mesh generation tools [Buchalter et al., 1990, Shaw et al., 2008].

3D FE Mesh Generation

The precise geometries derived from standard-care should be considered for biomechanical research purposes and patient-specific diagnosis. However, the bridge between medical imaging data to FE simulation software is both time consuming and a real challenge given several steps for segmentation which often is (a) generating a binary template from morphology contours [Papademetris et al., 2002, Ecabert et al., 2008, Ordas et al., 2007, Zhuang et al., 2010], (b) rigid/nonrigid registration to align the principal axis of each shape [Makadia et al., 2006, Tam et al., 2013] and (c) mesh generation, often via tetrahedral elements [Löhner, 1997, Fernandez et al., 2004]. Nevertheless, tetrahedral elements in FE simulation can generate significant errors for quasi incompressible tissues [Pathmanathan et al., 2009]. In contrast, cubic Hermite elements provide more efficient and accurate results in comparison to tetrahedral elements in

the solid mechanics domain [Zienkiewicz et al., 1977]. This element type represents the 3D Cartesian coordinates and the derivatives of shape with respect to the local coordinates, which reduces the computational cost [Niederer et al., 2011]. Hexahedral elements also provide regular and good mesh quality, which helps in stability and convergence of FE simulations during large deformations.

Here, we focused on the LV geometry rather than biventricular meshes which are frequently used for electromechanical FE simulations [Hunter et al., 1991,Nielsen et al., 1991,Hunter et al., 2003,Boyett et al., 2005]. Tam and coworkers provided an interesting survey on the challenges of rigid and nonrigid registration methods to customize a reference mesh to a template geometry in the computer vision domain [Tam et al., 2013]. An example of such a mesh morphing method is the work of [Yeh et al., 2011], who use a tailored Laplacian process framework to fit one triangulated mesh to a very different triangulated target. These registration methods (volumetric version) are often integrated as automatic tools in some FE mesh generation software which may fail when geometries are very different. However, there are no previously developed automated tools to reconstruct and personalize a geometry with hexahedral element types for the heart shape [Lamata et al., 2011].

Automatic mesh generation is interesting when a large amount of image data needs to be processed, so it is often more efficient to customize a reference mesh, or NURBS/B-splines to a patient's geometry by optimisation or mesh morphing methods [Rueckert et al., 1999, Couteau et al., 2000, Barber and Hose, 2005, Sigal et al., 2008, Lamata et al., 2011, Staten et al., 2011, Papazov and Burschka, 2011]. These optimisation algorithms often fail (give unreliable results) to generate a structured mesh from a generic model for prolated spheroidal shapes as the LV [Tustison and Amini, 2006]. Bistoquet and coworkers proposed a set of mathematical equations for a deformable bulk model compatible with the anatomy of LV [Bistoquet et al., 2007] which can also follow the cardiac cycle. They segmented and generated the first geometry from MRI images and then deformed this model based on the information of a midwall surface transformation map to another instance of the cardiac cycle.

One developed *automatic* mesh morphing method is the work of Antigo for arteries [Antiga, 2002]. He proposed a novel *centerline* based method (Figure 2.16) to customize a reference shape to a defined artery by moving a sphere on the centreline of the artery and calculating the intersection of this sphere and the artery wall. The algorithm then deforms the generic mesh to the target artery based on the intersection coordinate information. This method works well for the arteries, but it has not yet been applied on bulk shapes such as LV. Therefore, the

automatic mesh morphing subject for the LV or the heart shapes needs further investigation and development. To the best of our knowledge, the centreline method for mesh morphing in the LV has not yet been developed.

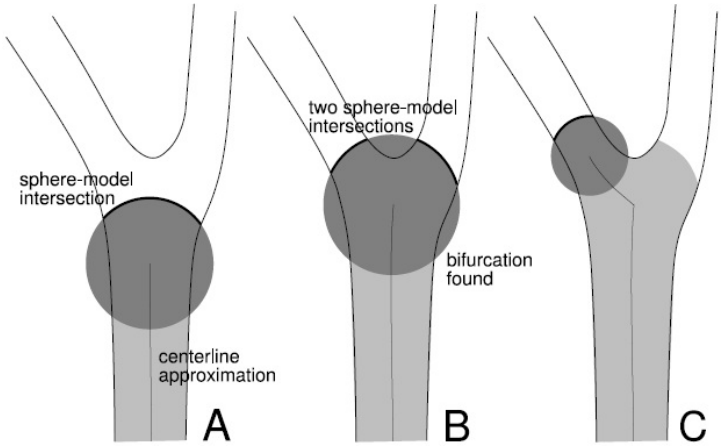

FIGURE 2.16 – Representation of the developed centreline method by [Antiga, 2002]. The intersection of the moving sphere on the artery's centreline is shown in this figure for one intersection (A), two intersections were detected (B) and at the detected bifurcation, one intersection profile is selected.

Quantitative Echocardiography for the Purpose of Mesh Generation

As mentioned before, MRI images are less accessible in the clinical daily routine and advanced MRI machines are often used for research purposes only. Another disadvantage of this imaging modality is the powerful magnetic field which can pull on any metal-containing instrument, such as prostheses or a heart pacemaker inside a human body, the breath-holding (at least $30s$) step during the acquisition to avoid artifacts and misalignments, and loud machine noise [Hartwig et al., 2009, Colletti et al., 2011]. Recently, advances in quantitative echocardiography (US) are becoming a valuable contribution to daily clinical needs [Willenheimer et al., 1997, Kimura et al., 1998, Jensen et al., 2004, Moore et al., 2002, Breitkreutz et al., 2007, Frederiksen et al., 2010]. A common interest among many research groups is to generate automatic 3D geometries from US images [Ledesma-Carbayo et al., 2004] and use these as a reference method in early detection of myocardial dysfunction.

In this context, GE Healthcare has developed a robust integrated software named EchoPac® to be used with their US System [Heimdal, 2011]. This software is an innovative technology to measure LV regional deformations based on the American Heart Association (AHA) standard (Figure 2.17) [Cerqueira et al., 2002] and to generate a mesh of the endocardial and epicardial surfaces (triangulated) at different instances of the cardiac cycle. The LV is divided into 17 re-

gions according to the AHA standard, in order to calculate LV regional (segment) deformations. This standard is used mostly in echocardiography to show real time LV regional deformation. The raw data which was used in the present PhD work was provided by a GE Healthcare US machine with integrated EchoPac® software.

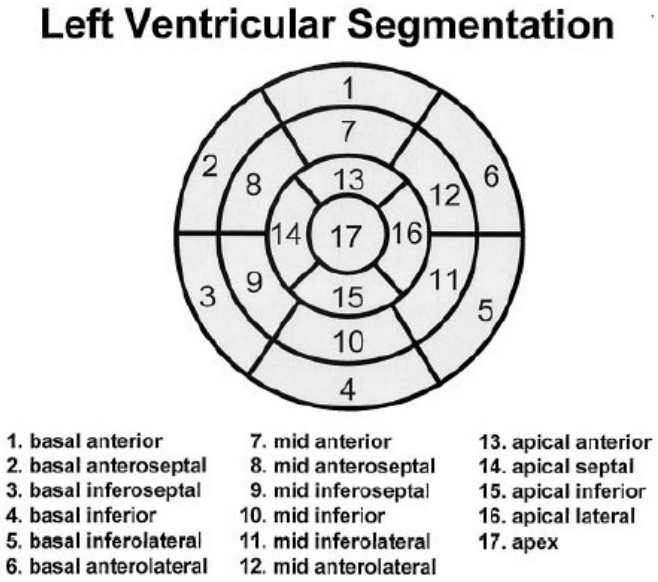

FIGURE 2.17 – Representation of the AHA standardized myocardial segmentation [Cerqueira et al., 2002] used in EchoPac® for US imaging analysis.

Here, we briefly explain the US method to capture in-vivo LV deformation. Essentially, any region in the myocardial wall has a unique natural acoustic reflection pattern. Each 20 to 40 pixels of stable patterns are named speckles or markers (spots generated by insonation and myocardial fiber interactions) as is shown in Figure 2.18 [Kaluzynski et al., 2001, D'hooge et al., 2002, Reisner et al., 2004, Leitman et al., 2004]. The speckle-tracking echocardiography technique as provided in EchoPac® allows the evaluation of global and regional myocardial function independent of the angle of insonation (US waves) and myocardial translational motion [Perk et al., 2007, Dandel et al., 2009, Blessberger and Binder, 2010, Geyer et al., 2010]. Tracking the displacement of speckles permits a semi-automated elaboration of their spatial deformation (strain) in three directions: longitudinal, circumferential and radial, the velocity of LV rotation, and the rate of deformation [Mondillo et al., 2011, Teske et al., 2007]. In order to avoid random noise, each sample of speckle analysis should be measured by averaging at least three consecutive cardiac cycles. The frame rate for acquisition is usually set to 60 to 110 frames per second for a better temporal resolution which enhances the feasibility for the frame-to-frame detection [Serri et al., 2006, Teske et al., 2007]. Previously, only tagging MRI enabled such an accurate detection

of myocardial movement (rotation and twisting) at this precision [Götte et al., 2006]. However, some consideration should be taken into account during image acquisition, such as breath-holding (this is also the case for tagged MRI), to capture true apical and short axis images, to avoid foreshortening of the myocardial tissue and to detect the endocardial border [Mondillo et al., 2011].

In order to calculate the LV regional deformation in the longitudinal, circumferential, radial and area, EchoPac® reconstructs a midwall (rule of thumb) for each of the 17 regions and follows the evolution of these meshes during a complete cycle [Orderud et al., 2008a]. The endocardial and epicardial surfaces are tracked frame-to-frame by an automatic algorithm of speckle-tracking which block match a defined region of interest (ROI) as is shown in Figure 2.19. This ROI is automatically defined at end-systole (ES) and updates follow LV motion through the cardiac cycle [Orderud et al., 2008b]. This task is very difficult, due to the low image quality in crucially ill patients (due to the posture of acquisition), positive pressure ventilation, wires, catheter, and so on [Bagger et al., 2012]. The segment markers can be modified (manually) in case of high error and deformation rejection of the detection algorithm in order to obtain an accurate deformation data. The frame rate must be more than 40% of the heart rate for the software to capture the marker movements in ROI (40 $frames/second$ for 100 $beats/minute$). It should be emphasized here that the extracted geometries are raw data to be later meshed with volumetric elements for use in FE software.

In this Section, we emphasised the needs and barriers to generate *automatic* FE meshes for real-time *patient-specific* simulation and explained available methods. In this thesis, we challenged several barriers to develop an automatic mesh generation tool for US data. Further, we will finish this Chapter by presenting the objectives of this PhD thesis.

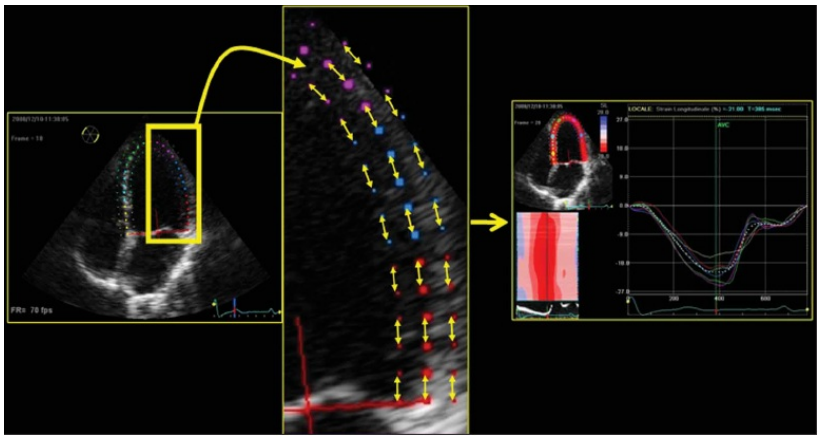

FIGURE 2.18 – Longitudinal strain measurements using the speckle-tracking echocardiography method [Heimdal et al., 1998].

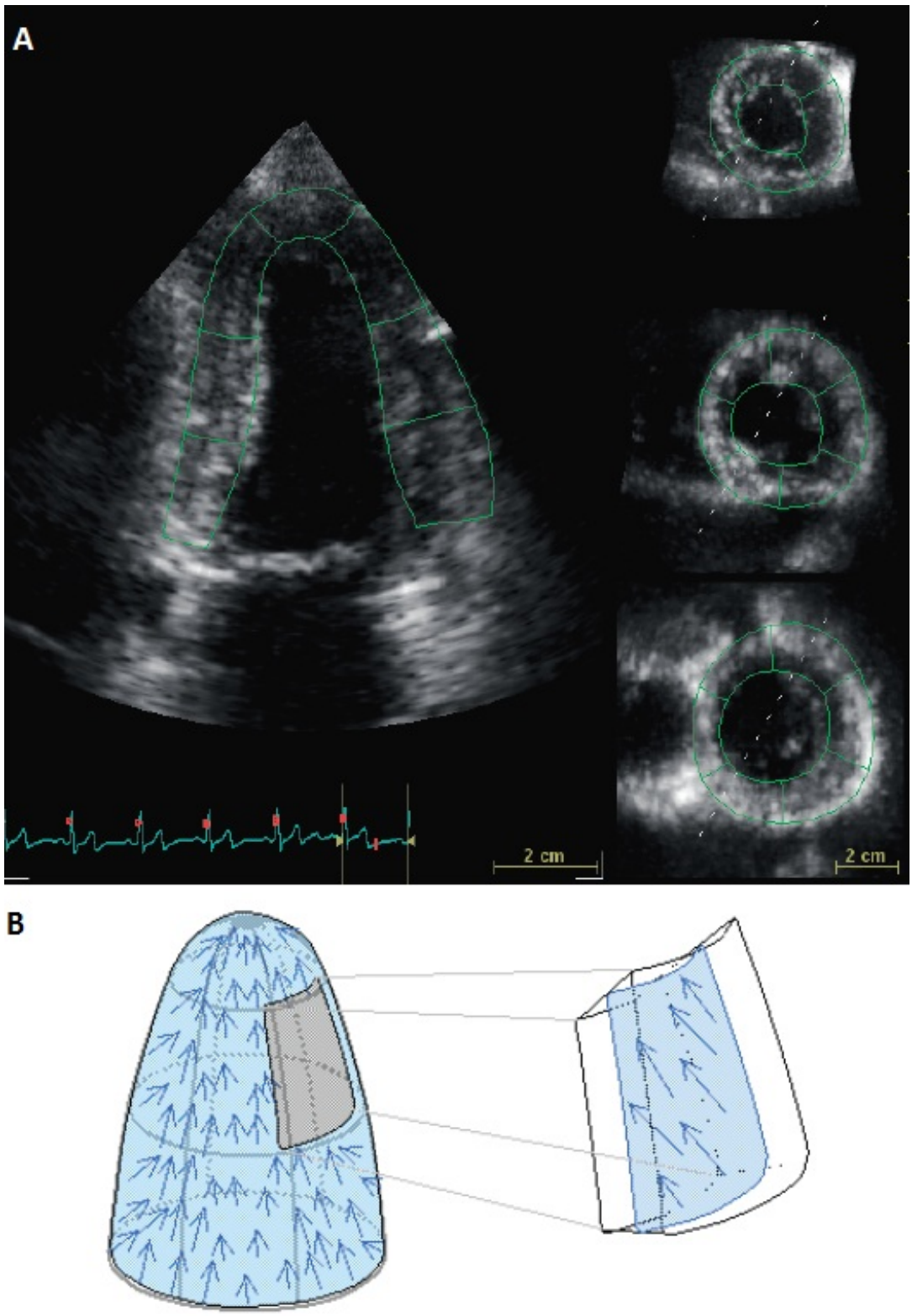

FIGURE 2.19 – This figure represents the considered ROI in longitudinal and three traverse slices of LV based on the speckle-tracking method in EchoPac® (A). In addition, the averaged myocardial surface mesh is calculated from the endocardial and the epicardial surfaces (B) [Heimdal, 2011].

2.5 Objectives of this PhD work

The literature review in this Chapter shows that, despite many decades of study on cardiac subjects, there is still potential to improve and develop novel methodologies for geometry acquisition and FE simulations.

For the purpose of this work, one LV from a healthy volunteer and eight LBBB patients data were provided by GE Healthcare to Simula Research Laboratory. Regional deformations, cavity volumes and pressures, and endocardial and epicardial surfaces were provided in ".h5" format for all LBBB patients.

Knowing the mechanical stresses can help in a better decision on the process of myocardial injection which can result in a series of geometrical adaptation which lead to increase the risk of heart failure [Kichula et al., 2014].

Several hypotheses and potential developments in cardiac FE simulations were studied with the provided data:

— Complex image-based models as well as detailed numerical simulations have been developed for the heart. However, the bridge between these two matters require further study. One of the major objectives of this PhD work is to connect image-based patient data to the numerical modelling of the heart.

— The geometry has more impact on the final Cauchy stress than the isotropic MPs in thin walled structures. This has not been examined for thick walled geometries as LV, and especially, for exponential strain energy functions. The objective here is to examine this assumption for LV.

— *Displacement-driven* simulations of type Dirichlet reduces the sensitivity of mechanical response in thin walled structures to MPs. This assumption has not yet been examined in thick walled structures. We will perform several FE analysis to examine this hypothesis for LV.

— An automatic volumetric mesh generation with hexahedral elements has not yet been developed. In the present work, we aimed to develop an approach for this purpose.

— Knowing the regional deformation, an average approximation of active stress and a simple isotropic material model, one can numerically represent the mechanical behaviour of a LBBB patient's myocardium. We plan to show that a homogeneous active contraction is sufficient for detection of abnormal tissue zone.

— Due to the complexity of cardiac simulations, the proper material models are not develo-

ped in most FE simulation software products. We developed an in-house subroutine code for Abaqus® FE software in order to perform the contraction phase for a transversely isotropic material model based on available literature and we tested it with a healthy LV.

2.6 Conclusion

This Chapter has reviewed the medical, numerical and scientific problems considered in this PhD thesis. The next Chapters will explain, in detail, the methods we have used to achieve these PhD objectives.

Chapitre 3

Impacts des paramètres du matériau et la fonction d'énergie de déformation sur les contraintes Cauchy de la paroi du VG

Dans ce chapitre, les impacts des paramètres du matériau sur la contrainte Cauchy dans la paroi du VG pour deux types de fonctions d'énergie de déformation hyperélastiques (isotrope et isotrope transverse) sont étudiés. Puis, les impacts des différentes conditions aux limites avec différents paramètres des matériaux est étudiés pour un modèle isotrope à la fin de la diastole. La géométrie de cette étude est le VG sain fourni par GE Healthcare. Les notations peuvent être différentes dans ce chapitre. Ce travail ayant été soumis dans le journal "CMBBE 2016" et a été présenté lors de la conférence internationale CMBBE2015 à Montréal. Le chapitre est rédigé sous la forme d'un article en anglais, précédé d'un préambule en français.

Sommaire

Préambule

Dans ce chapitre, la géométrie du VG sain a été utilisé pour étudier les impacts des paramètres des matériaux sur la contraintes Cauchy. GE a fourni les surfaces fermées du VG qui ont ensuite été coupées à la partie basale (en format *.stl*). Ensuite, la géométrie a été importé au logiciel Avizo® pour la transformer en images binaire. Ces images sont des coupes transversales de partie basal à l'apex avec $0,1$ mm dans la direction longitudinale. À partir de ces images, une géométrie a été généré en format *.IGES* pour importer dans le logiciel Abaqus®. La raison pour laquelle nous avons fait cette étape est, d'abord, de générer le format approprié pour le logiciel Abaqus® pour le mailler avec des éléments hexaèdre, puis régénérer la géométrie avec un nombre plus élevé de nœuds.

Avec ce modèle d'EFs, nous avons cherché à étudier les réponses de Cauchy à la fin de la diastole pour un modèle isotrope simple (Mooney-Rivlin) et un modèle isotrope transverse (Guccioné). Pour effectuer des simulations par EFs, l'algorithme proposé par [Riveros et al., 2013] pour générer la géométrie non-chargée a été utilisé. Cet algorithme, de manière itérative, gonfle la géométrie (avec 2 kPa), réduit ensuite le modèle initial pour finalement l'ajuster au modèle gonflé à la géométrie de la fin de diastole (données d'image). De cette façon, la contrainte de Cauchy est reconstituée et représente, peut-être, la géométrie chargé dans les données d'image (US). Nous avons effectué un grand nombre d'analyses pour les deux phases du cycle cardiaque en choisissant aléatoirement dans un intervalle les valeurs des paramètres hyperélastiques assignées au tissu cardiaque.

A la fin de la diastole, nous montrons que le VG est presque isostatique sous certaines hypothèses avec des propriétés hyperélastiques simples. De plus, il est plus sensible au modèle de matériaux complexe nonlinéaire et exponentiel. Le modèle de Guccioné est une subroutine qui a été développé pour le logiciel Abaqus® et est présenté dans le Chapitre 4.

Pour la systole, d'abord, les équations de la contraction systolique sont présentées. Puis pour le modèle de matériau isotrope simple, deux conditions sont étudiées pour analyser l'impact des conditions aux limites sur la surface de l'endocarde (la pression ou le déplacement) et sur la contrainte Cauchy en systole. À la fin de la systole, nous montrons que les contraintes passives deviennent négligeables par rapport aux contraintes actives et que ces derniers peuvent être directement attribués à un modèle par EFs du VG contracté.

Les simulations par EFs dans le logiciel Abaqus® pour la phase systolique sont effectuées avec des solveurs Explicite. De plus, pour les phases diastoliques, elles le sont avec des solveurs

Standard. Pour le solveur explicite, l'échelle du temps et la densité du matériau ont été choisis précisément pour éviter l'effet dynamique (l'énergie cinétique inférieure à 1% l'énergie de déformation).

3.1 Importance of material parameters and strain energy function on the wall stresses in the LV

Sareh Behdadfar, Laurent NAVARRO, Joakim SUNDNES, Molly MALECKAR, Stéphane AVRIL

Computer Methods in Biomechanics and Biomedical Engineering

ABSTRACT

Patient-specific estimates of the stress distribution in the left ventricles (LV) may have important applications for therapy planning, but computing the stress generally requires knowledge of the material behaviour. The passive stress-strain relation of myocardial tissue has been characterized by a number of models, but material parameters (MPs) remain difficult to estimate. The aim of this study is to implement a zero-pressure algorithm to reconstruct numerically the stress distribution in the LV without precise knowledge of MPs. We investigate the sensitivity of the stress distribution to variations in the different sets of constitutive parameters. We show that the sensitivity of the LV stresses to MPs can be marginal for an isotropic constitutive model. However, when using an anisotropic exponential strain energy function, the LV stresses become sensitive to MPs, especially to the linear elastic coefficient before the exponential function. This indicates that in-vivo identification efforts should focus mostly on this MP for the development of patient-specific finite-element analysis.

GRAPHICAL ABSTRACT

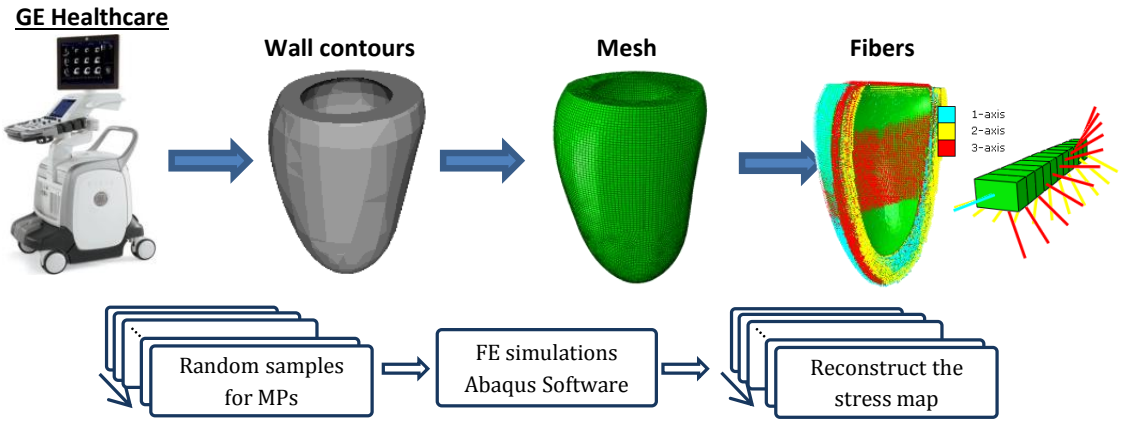

HIGHLIGHTS

— Two points in cardiac pressure-volume curve have been investigated by a FE model.

— Using an anisotropic exponential strain energy function, the LV stresses become sensitive to the choice of material parameters, especially to the linear elastic coefficient before the exponential function

— We conclude that in-vivo identification efforts should focus mostly on the linear elastic coefficient for the development of patient-specific finite-element analysis

KEY WORDS : cardiac mechanics ; strain energy function ; mechanical stresses ; inverse method ; mechanical properties.

3.1.1 Introduction

Nowadays, there is a growing interest in patient-specific finite-element (FE) stress analysis in many soft tissues [Wang et al., 2002, Wang et al., 2013]. It is known that in normal homeostatic conditions, tissues adapt, grow or remodel themselves in order to regulate the stresses [Humphrey, 2006, Graham Jr et al., 1968]. Consequently, the stress distribution may provide important indications about the mechanobiological function and metabolism of the tissue. As far as the left ventricle (LV) is concerned, geometrical adaptation may occur after myocardial infarction and also after myocardial injection when this treatment is employed to avoid possible risks of heart failure [Kichula et al., 2014]. In these different situations of adaptation, reconstructing the stress distribution may be very useful.

Researchers mostly focused their attention on the reconstruction of three dimensional strain maps throughout a cardiac cycle [Tustison and Amini, 2006, Spottiswoode et al., 2007] using medical imaging modalities such as gated MRI or ultrasound (US). To assess the wall stress distribution from these strain maps, it is necessary to know the constitutive material parameters (MPs) and initial stresses in the tissue.

Characterizing the MPs involves several difficulties. The MPs may be obtained using in-vitro experiments carried out on myocardial tissue collected on cadavers [Gee et al., 2010]. But the issue is that this method does not yield patient-specific MPs that can be used for clinical applications. Another approach is to calibrate a model against clinical data [Krishnamurthy et al., 2013, Klotz et al., 2006, Raghavan et al., 2006]. One has to define a cost function to minimize the differences between data and the model. It may be difficult though to ensure a unique solution to the minimization problem in case of inadequate clinical data.

However, stress analysis does not systematically require a precise knowledge of MPs, as [Miller and Lu, 2013] and [Joldes et al., 2016] have shown for arteries and brain tissue for which the numerical simulations are only weakly sensitive to the MPs. Based on this, [Lu et al., 2008] developed an inverse analyses method to reconstruct stress distributions in thin-walled biological organs. The point of their approach is that the stress field in a statically determinate problem only depends on the boundary conditions and on the geometry but not on the MPs. They showed an example of successful application on aortic aneurysm but they did not discuss possible applications on thick-walled geometries such as the LV.

The hypothesis of the present study is that this approach of stress estimation without knowing the MPs could be extended to the reconstruction of the stress distribution in the LV. We will assess the validity of this hypothesis first for a passive LV, both for a simple isotropic

material model and a more complex anisotropic model regarded as a realistic representation of passive myocardial tissue [Guccione et al., 1995]. Finally, we assess the hypothesis for a material model with active contraction, for reconstructing the systolic LV stress distribution. After giving the details for reconstructing end-diastolic (ED) and end-systolic (ES) stress distributions based on the proposed approach, we draw conclusions for potential future studies.

3.1.2 Materials and Methods

Geometrical Model

The LV of a healthy volunteer was segmented from a 4D US scan using the VTK library [Hansegård et al., 2009]. The mesh at ED was reconstructed with 8-noded linear brick elements (155,172 nodes and 141,405 elements, after performing a convergence study, see 3.1(a)). The nodes of the base were constrained to remain coplanar during the deformations. A local curvilinear coordinate system aligned along the fiber direction was considered [Bovendeerd et al., 1994]. Fiber directions varied from -70° at the epicardial surface to 60° at the endocardial surface, where 0° was the circumferential direction (Figure 3.2. At every element across the wall of the LV, we defined a local orthonormal basis denoted $(\vec{\mathbf{e}}_n, \vec{\mathbf{e}}_s, \vec{\mathbf{e}}_f)$, where $\vec{\mathbf{e}}_f$ is aligned with the local fiber orientation in the reference configuration

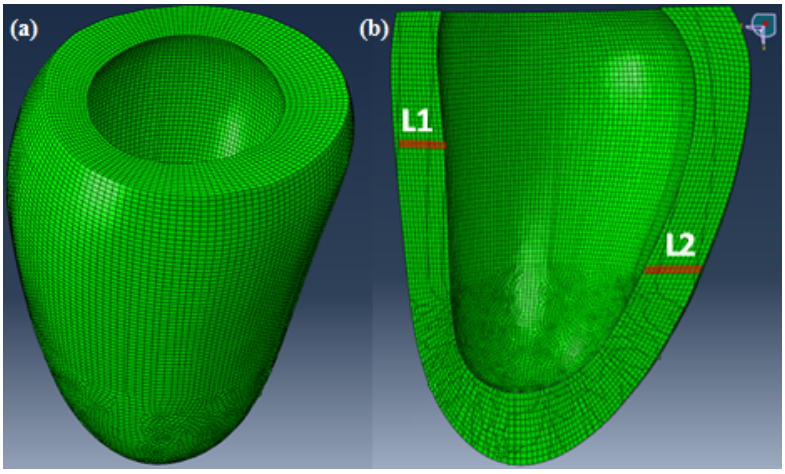

FIGURE 3.1 – (a) LV model meshed in Abaqus® software. (b) Selected paths across wall thickness used to study the stress variations across the thickness and the impact of MPs onto these stresses.

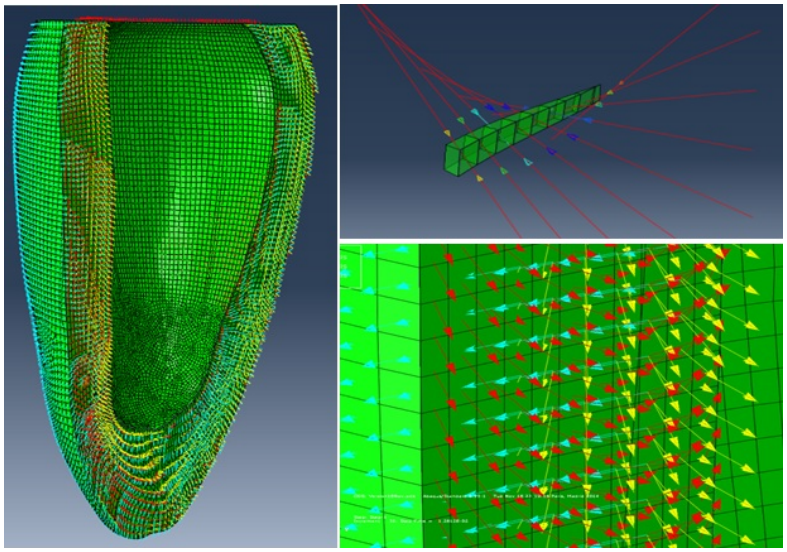

FIGURE 3.2 – Personalized LV model with fiber structure. The red streamlines are aligned along fiber directions in the local coordinate system.

Method for Numerical Stress Reconstruction at ED

The in-vivo heart is never unloaded, and the ED geometry extracted from US images corresponded to a non-zero cavity pressure. The unloaded geometry was reconstructed using the approach of [Riveros et al., 2013] ; we refer to this method as the zero-pressure algorithm [Trabelsi et al., 2015]. More specifically, we iteratively updated the unloaded geometry and computed its deformation upon pressurization (endocardial surface loaded with a 2 kPa pressure) until the deformed geometry matched the ED geometry (tolerance$\leq$0.028 mm) obtained from US images. The deviation between the deformed geometry and the US-derived ED geometry was obtained by calculating the absolute maximum nodal distance as illustrated in Figure 3.3.

After deriving the unloaded geometry, the Cauchy stresses at ED were deduced such as:

$$\sigma_{passive} = J^{-1}\mathbf{F}(\partial W/\partial \mathbf{E})\mathbf{F}^{T}. \tag{3.1}$$

where W is the strain energy function, $\mathbf{F}$ is the deformation gradient, $J = det(\mathbf{F})$ is the determinant of the deformation gradient, and $\mathbf{E}$ is the Green-Lagrange strain tensor.

In the literature, different strain energy functions have been proposed for the passive behaviour of cardiac tissue, as in [Holzapfel and Ogden, 2009], [Guccione et al., 1995] and [Usyk et al., 2000]. In order to investigate the impact of the strain energy function on the stress reconstruction, we used first a simple Mooney-Rivlin strain energy function as previously used

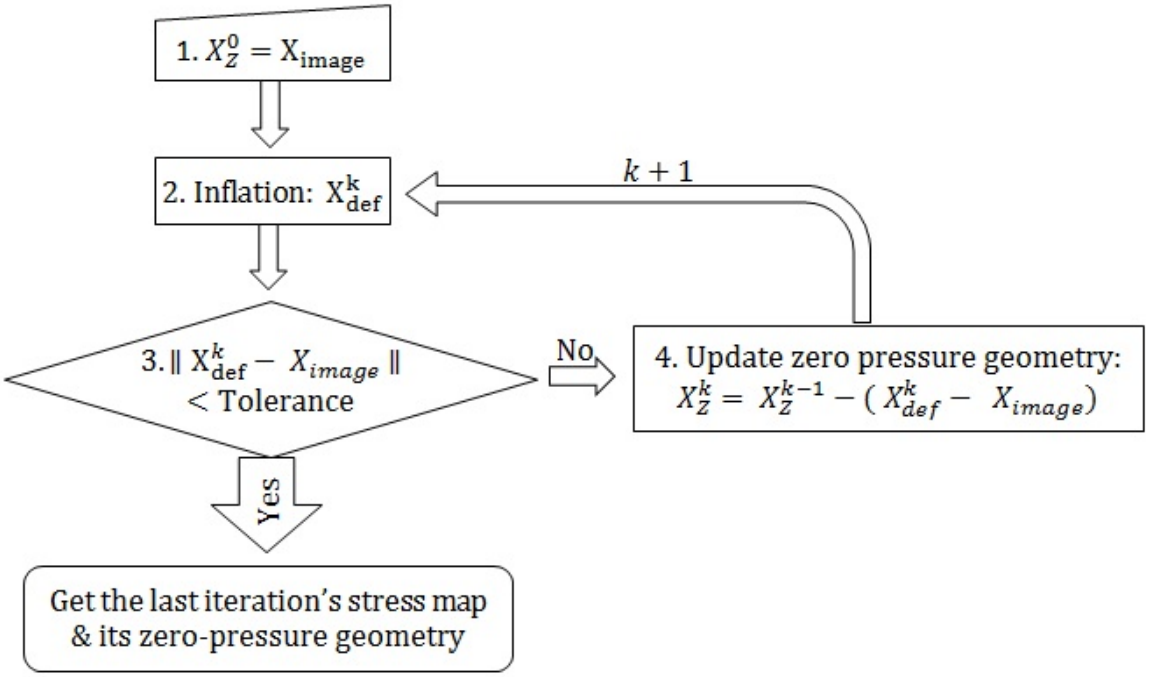

FIGURE 3.3 – Flowchart of the zero-pressure algorithm used to obtain the load-free geometry. The image-based geometry was considered as the initial loaded configuration. Then, the algorithm returned the unloaded geometry of this initial configuration.

by [Marchesseau et al., 2013a]:

$$W = c_1(\bar{I}_1 - 3) + c_2(\bar{I}_2 - 3) + K(J-1)^2. \tag{3.2}$$

where c_1 and c_2 are MPs, $\bar{I}_1$ and $\bar{I}_2$ are invariants of the right Cauchy-Green tensor and $K = 2/d_1$ is the bulk modulus, d_1 being the compressibility term.

In addition, we used the Fung-type strain energy function developed by [Guccione et al., 1995] (refer to Annexe A):

$$\begin{aligned} W &= \frac{1}{2}c(exp(Q) - 1) + K(J-1)^2, \\ Q &= b_3\bar{E}_{ff}^2 + b_2(\bar{E}_{ss}^2 + \bar{E}_{nn}^2 + 2\bar{E}_{sn}^2) + b_1(2\bar{E}_{fs}^2 + 2\bar{E}_{fn}^2). \end{aligned} \tag{3.3}$$

where W is a function of six independent components of isochoric Green-Lagrange strain tensor $\bar{E}_{ij}$ in *fiber (f)*, *sheet (s)* and *sheet-normal (n)* directions, and c and b_{1-3} are the four MP values.

Finally, we compared our approach to the method of [Joldes et al., 2016] for stress reconstruction, which consists in assigning very stiff linear elastic material properties (10 MPa and

0.49 as elastic modulus and Poisson's ratio) to the LV in its actual geometry at ED.

Method for Numerical Stress Reconstruction at ES

The Cauchy stress tensor at ES was defined as:

$$\sigma_{\mathbf{total}} = \sigma_{\mathbf{passve}} + \sigma_{\mathbf{active}}, \tag{3.4}$$

where $\sigma_{\mathbf{active}}$ is the contribution of myocyte contraction.

We denote by $\mathbf{R}_f$ the matrix of the covariant transformation from the global orthonormal to the local basis (refer to Section 3.1.2) :

$$\sigma_{\mathbf{active}} = J^{-1}\mathbf{F}\mathbf{R}_f{}^{-1}\begin{bmatrix}0 & 0 & 0\\ 0 & 0 & 0\\ 0 & 0 & a_f\end{bmatrix}\mathbf{R}_f\mathbf{F}^T, \tag{3.5}$$

where a_f is the active tension developed by the contracting fibers.

In physiological models, a_f is often computed by solving systems of ordinary differential equations describing cell electrophysiology and contraction [Nash and Panfilov, 2004]. Here, for the sake of simplification, we assigned a predefined value to a_f equal to 135 kPa as explained in [Walker et al., 2005b] and [Dorri et al., 2006]. In this condition, the only variations will be due to the MPs and not the active stress value. We performed FE analysis from ED to ES and estimated the induced Cauchy stress for different sets of MPs explained in the next subsection.

As the reference FE model is reconstructed at ED from US, we performed a forward simulation to obtain the reference geometry at ES. This computation is the response to a combination of ES pressure (11.24 kPa at ES) and the prestress of 135 kPa applied uniaxially along the fiber directions (refer to Section 3.1.2). This computation was the combination of systolic cavity pressure (11.24 kPa at ES) and the prestress of 135 kPa applied along the fiber directions with the following MP values for the Mooney-Rivlin strain energy function: $c_1 = 0.0176$, $c_2 = 0.0188$ and $d_1 = 0.1079$ in MPa.

Statistical Analysis

Several FE analyses (40) were performed by drawing randomly different MP sets with uniform distribution within the range of values of [Marchesseau et al., 2013a] in Table 3.1. For

each analysis, a random sample was drawn for each parameter (c_1, c_2 and d_1) to employ the zero-pressure algorithm with diastolic cavity pressure equal to 2 kPa. For the Guccione strain energy function, we collected 12 MPs obtained from literature (Table 3.2) and performed 12 FE analyses with the zero-pressure algorithm (2kPa).

FE analyses introduced in Section 3.1.2 and 3.1.2 were performed with the Abaqus® software on a local cluster (8-core Intel Xeon-E5530 2.4-GHz, 24-Go RAM).

TABLE 3.1 – MPs intervals for isotropic material model from [Marchesseau et al., 2013a].

c_1 (kPa)	c_2 (kPa)	d_1 (MPa)
$7-20$	$7-20$	$0.08-0.3$

3.1.3 Results

The zero-pressure algorithm was applied with 40 samples of MPs for the Mooney-Rivlin model at ED. The maximum nodal distance observed between the reference image data and the zero-pressure geometries (ZPGs) after loading was 0.027 ± 0.001 mm. The stress and strain results for the Mooney-Rivlin model are shown as colormaps in Figure 3.4. The Mooney-Rivlin stress values are also reported in Table 3.3 for different paths throughout the wall thickness (refer to Figure 3.1(b)). The circumferential stresses show larger values where the myocardial fibers are aligned in this direction. For all isotropic stress values, the standard deviation (SD) is one to two orders less compared to the mean stress. In addition, the results of 99% of total LV elements vary less than 2% in terms of maximum-principal Cauchy stresses.

The stress reconstruction obtained with the approach of [Joldes et al., 2016], using rigid elastic properties and linear infinitesimal resolution, is shown in Figure 3.5. It is consistent with the Mooney-Rivlin case.

The stress and strain results for the Guccione model are shown as colormaps in Figure 3.4 as well. The results with the Guccione material model are reported in Table 3.2, showing larger variations in fiber stresses than the Mooney-Rivlin model (Figure 3.4). The mean value for maximum distance between the reference image-based geometry and the ZPGs geometry after loading is $0.0281 \pm 8e-04$ mm. The correlation coefficients between MPs and the fiber stresses obtained from FE analyses are shown in Table 3.4. There is a correlation of approximately 0.8 at ED between the linear coefficient and fiber stresses (Table 3.4). There is only a moderate correlation between the exponential coefficients and the fiber and sheet stresses. Actually, the

variation of stresses is fairly low for a number of sets of MPs.

The simulated reference contraction Figure 3.6 produced an ejection fraction of 33.83%, a wall thickness change of 18.7% and Von-Mises stresses in the range of $100 - 150$ kPa, which are all reasonable values for LV contraction [Dorri et al., 2006, Hunter et al., 1998].

Stress maps reconstructed in the equatorial plane (Mooney-Rivlin passive model) are displayed in Figure 3.7, while the stress values are reported in Table 3.5, for the transmural paths in Figure 3.1(b). Here, it can be noticed that the Von-Mises stress increases from epicardium to endocardium. For all stress values, the SD is one order of magnitude lower than the mean value.

TABLE 3.2 – The Fiber and Sheet stress results across the equatorial plane in LV model for the Guccione strain energy function at ED in kPa. The stress values at the equatorial plane show higher average values in comparison to the isotopic stress results at the equatorial plane (Figure 3.4).

	c kPa	b_3	b_2	b_1	$MeanFiber$	$MeanSheet$
1. [Okamoto et al., 2000]	0.512	67.1	24.2	21.6	4.48	2.1
2. [Keldermann et al., 2010]	1.2	26.7	13.5	14.7	43	2.5
3. [Wenk et al., 2009]	0.33	49.3	19.3	17.4	4.3	2.2
4. [Walker et al., 2005b]	0.128	53.7	21.3	17.3	4.2	2.4
5. [Walker et al., 2005b]	0.146	67.1	26.6	21.6	4.2	2.3
6. [Walker et al., 2005b]	0.233	49.3	19.3	17.4	4.3	2.3
7. [Xi et al., 2011]	0.189	29.9	13.5	13.3	4.1	2.6
8. [Augenstein et al., 2005]	3	11.1	1.8	10	5.4	1
9. [Land et al., 2012]	1.662	14.3	4.5	10	4.6	1.8
10. [Omens et al., 1991]	2.4	26.7	2	14.7	6.2	0.2
11. [Walker et al., 2005b]	0.359	67.1	24.2	21.6	4.4	2.1
12. [Omens et al., 1993]	2.2	9.2	2	3.7	5.2	1.34

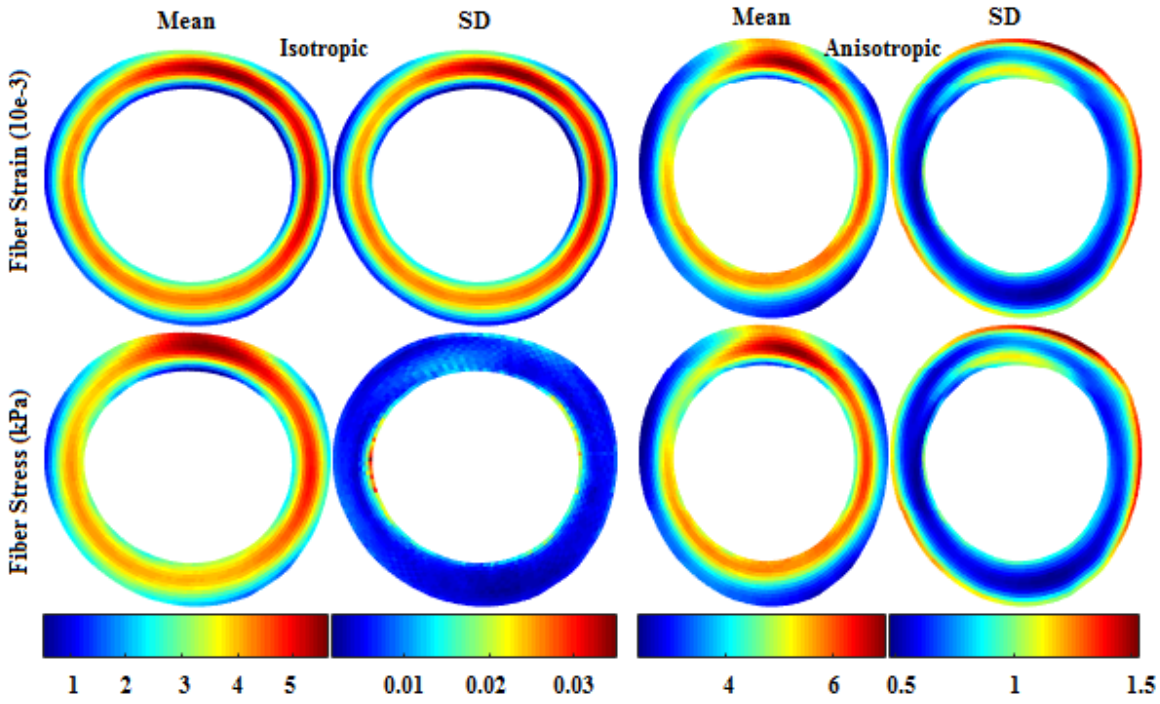

FIGURE 3.4 – Mean and standard deviation of the fiber stress and strain for 40 isotropic and 12 anisotropic models.

TABLE 3.3 – The Fiber stress and strain results through wall thickness from epicardium to endocardium along two paths (L1 and L2) at ED. The stress and strain results are concentrated where the fibers are aligned with the circumferential direction. In inflation loading, the circumferential direction is naturally the direction of the major principal stress.

Fiber stress (kPa)												
L1	Position	1	2	3	4	5	6	7	8	9	10	11
	Mean	2.58	3.16	3.77	4.35	4.75	4.91	4.77	4.34	3.73	3.01	2.48
	SD (10-3)	7	5	6	4	6	4	6	8	8	13	22
L2	Mean	1.61	1.96	2.45	2.99	3.47	3.8	3.89	3.7	3.24	2.61	1.75
	SD (10-3)	3	4	4	5	3	3	3	5	11	12	21
Fiber strain												
L1	Mean (10-3)	5	10	15.4	20	23.9	25.1	23.6	19.6	13.7	7	1
	SD (10-3)	1	1	2	3	4	4	4	3	2	1	0
L2	Mean (10-3)	2.2	5	9	13	17	20	20	18	13	7	0
	SD (10-3)	0.4	0.9	1	2	3	3	3	3	2	1	0

TABLE 3.4 – Values of correlation coefficients for four MPs and Cauchy Fiber stress values (kPa) at ED obtained with the Guccione material model after application of zero-pressure algorithm. This table shows a strong correlation of the fiber stress results to the linear coefficient before the exponential term of the strain energy function.

	$Meanfiber$	$Meansheet$
c	0.82	-0.86
b_3	-0.5	0.52
b_2	-0.72	0.74
b_1	-0.44	0.45

TABLE 3.5 – Fiber stress across wall thickness from epicardium to endocardium along two paths (L1 and L2) at ES. Along L1, which is perpendicular to the applied cavity pressure, the fiber stresses are higher at the epicardial surface whereas along L2 the maximum values are observed closer to the endocardial surface.

		Fiber stress (kPa)										
	Position	1	2	3	4	5	6	7	8	9	10	11
L1	Mean	89.9	91.4	91.3	88.4	81.9	73.5	64.5	58.1	54.4	57	61.6
	SD	6.4	6.2	5.5	4.3	3.1	2.9	3.5	4	4.1	4	3.8
L2	Mean	35.1	40.6	46.2	54.2	67.3	82.2	90.1	80.2	58.7	32.7	9.5
	SD	4.2	3.8	3.5	3.1	2.5	2.6	3.4	2.8	3	3.7	3.5

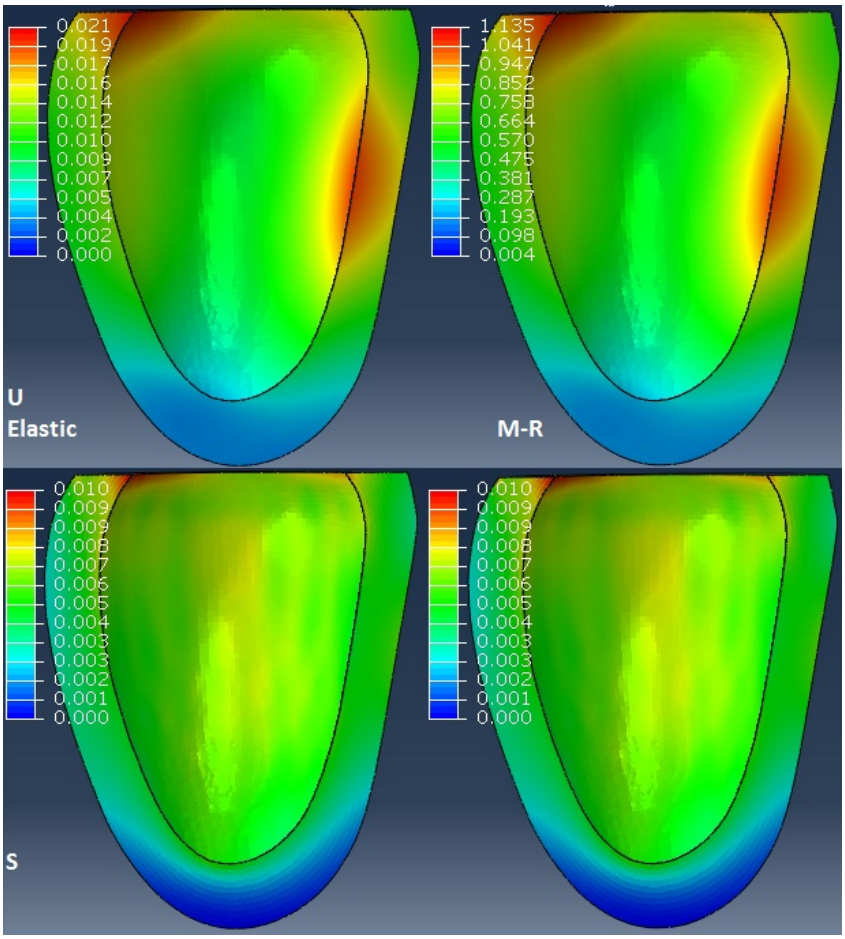

FIGURE 3.5 – Forward elastic simulation of the ED geometry using a linear elastic infinitesimal resolution with rigid parameters (10 MPa and 0.49 as elastic modulus and Poisson's ratio). The obtained results at ED (displacement and Von-Mises stress on the left hand side) are compared with the ones (right hand side) using the zero-pressure algorithm with the Mooney-Rivlin material model (for $c_1 = 0.0117$, $c_2 = 0.0182$ and $d_1 = 0.1591$). The displacements U are in mm and the Von-Mises stresses in MPa.

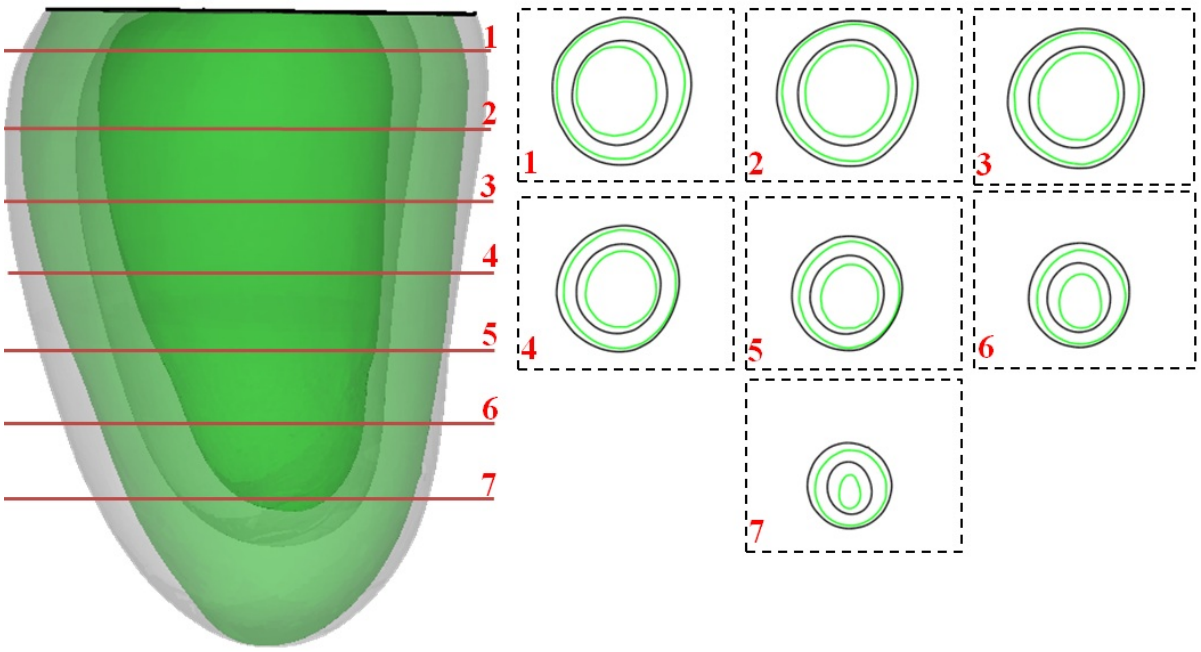

FIGURE 3.6 – Reference ES geometry (green shaded) overlaid onto the ED initial configuration (grey shaded) in 3D representation and at different transversal cross sections. The simulation with active contraction produced an ejection fraction of 33.83% and a wall thickness change of 18.7%.

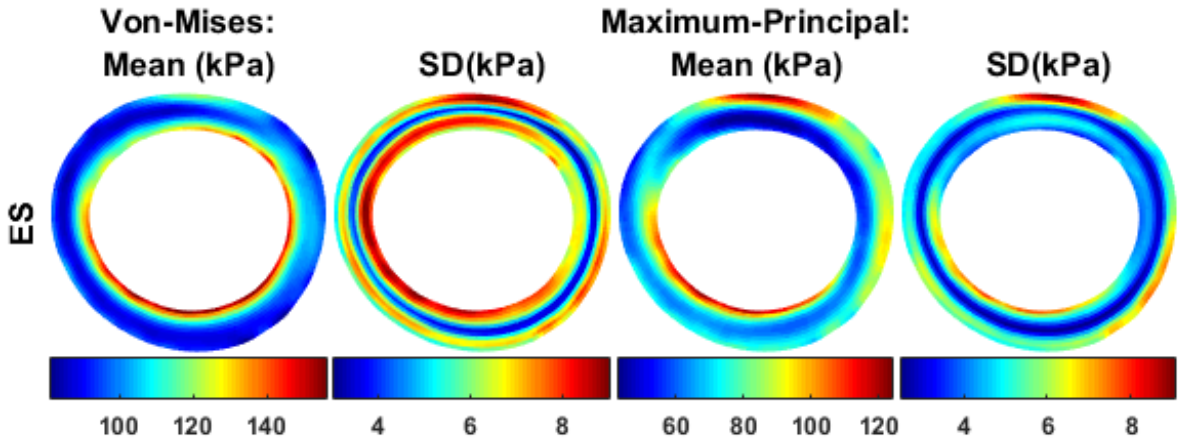

FIGURE 3.7 – Mean and standard deviation of Maximum-Principal and Von-Mises stress results reconstructed at ES taking into account the active contraction. The stresses increase from the pressurized endocardial surface to the epicardial surface.

3.1.4 Discussion

Reconstructing the stress distribution in the LV using the zero-pressure algorithm proposed by [Riveros et al., 2013], we have shown that the LV stresses can be reconstructed relatively independently of MPs.

This result is significant as in normal homeostatic conditions, tissues adapt, grow or remodel themselves in order to regulate the stresses [Humphrey, 2006, Graham Jr et al., 1968]. As far as the LV is concerned, geometrical adaptation may occur after myocardial infarction and also after myocardial injection when this treatment is employed to avoid possible risks of heart failure [Kichula et al., 2014]. In these different situations of adaptation, reconstructing the stress distribution using the Laplace law is not accurate enough [HUISMAN et al., 1980, Yin, 1984] and it is interesting to have a patient-specific method which does not require to identify all the sets of MPs for every patient.

We varied the MPs either by drawing them randomly or by testing different sets of values available in the literature. None of the tested values were the actual MPs of our subject's myocardium. The goal was only to achieve different virtual experiments in order to emphasize that knowing all the MPs of a given subject is not required to reconstruct the LV stress distribution.

In our analysis, we performed some of the stress reconstructions using isotropic strain energy function. Although it is well known that the myocardium is anisotropic, we showed that the reconstructed stress obtained with the isotropic model is a rather good approximation of the same reconstructed stress obtained with an anisotropic model.

Results in Figure 3.4 and Table 3.3 show a very low correlation between passive stresses and MPs in case of isotropy. This is consistent with the results obtained on other soft tissues by [Miller and Lu, 2013]. They showed that MPs have a marginal impact on the stress distribution of inflated geometries. In that case, stress distributions can be reconstructed using a simple linear infinitesimal approach as introduced by [Joldes et al., 2016].

With the commonly used Guccione model, which accounts for anisotropy, among all the MPs, only variations of the c as the linear and b_2 coefficient parameters had significant impact on the reconstructed stress distributions. We can even see in Table 3.4 that the calculated fiber and sheet stresses are strongly coupled to c. The dependence between the reconstructed stress distributions and c points out the scaling role of the linear coefficient in Fung-like strain energy functions. This also indicates that the stress can be reconstructed fairly independently of the exponential coefficients of the Guccione model. This is also a significant result as no

efficient method exist for the moment to derive non-invasively and patient-specifically all the parameters of the Guccione model in vivo.

We also reconstructed stresses at ES with a combination of passive and active contributions. The active contribution mostly depends on a_f and the passive contribution depends on the deformation from ED to ES, which takes the tissue from a state of circumferential tension to compression. We showed eventually in Figure 3.7 that passive MPs marginally impact the reconstructed stress at ES, but this is induced by the small level of passive stresses compared to active stresses at ES.

3.1.5 Limitations and Perspective

The objective of this paper was to be able to reconstruct numerically the stress distribution in the LV without knowing the MPs of myocardial tissue. While promising, there are several limitations to the approach.

The active contraction model applied for the ES data is a simplification compared with the state-of-the-art models. Another limitation is that we did not study the effect of fiber orientations on the stress reconstructions (we used always the same orientations in all our analyses). However, due to the form of the Guccione strain energy at ED, we expect that fiber orientations have a similar effect on the stresses as varying the exponential coefficients. We showed that this effect was marginal.

Another limitation to be mentioned is that the US images were captured from the basal part and other tissues such as valves, papillary muscles and irregularities were removed. The presence of all these features may affect the local distribution of stresses, meaning that most of the conclusions of this study would not hold at a local scale where these features would be resolved.

3.1.6 Conclusion

In this study, we showed that it is possible to reconstruct numerically the stress distribution in the LV without precise knowledge of MPs of myocardial tissue. However a patient-specific geometry of the LV is always required, which highlights the importance of patient-specific FE model morphology over the MPs. Only the linear elastic coefficient of the Guccione strain energy function may be required to have an accurate stress reconstruction. This implies that the effort should focus mostly on the identification of this MP for patient-specific stress reconstructions. It is also important to continue exploring more realistic models for ES, to determine whether

the same relations hold.

3.1.7 Appendix

Calculate ES blood pressure for this Article

From [Dorri et al., 2006] : $P_{LV} = -944t^2 + 245t. \rightarrow 0 \leq t \leq 0.2s$

$t = 0.2 \rightarrow P = 11.24.$

Complementary Data

Figure 3.8(b) is an example of the reconstructed unloaded geometry superimposed with image-based ED.

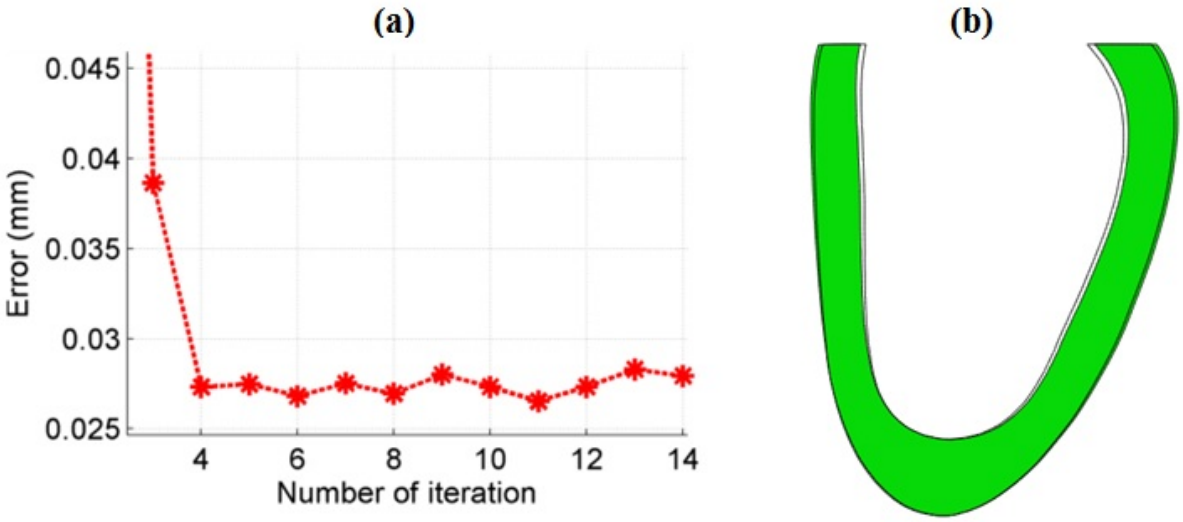

FIGURE 3.8 – (a) The error trends for one random sample of MPs to obtain the ZPG. (b) The ZPG (black wireframe) and loaded configuration (shaded in green).

The six components of strain tensor are displayed in equatorial level of LV in Figure 3.9 in local direction for one material sample. This Figure shows that the strains are consistent with experimental results available in the literature by [Guccione et al., 1995, Omens et al., 1991, Costa et al., 2001] through wall thickness.

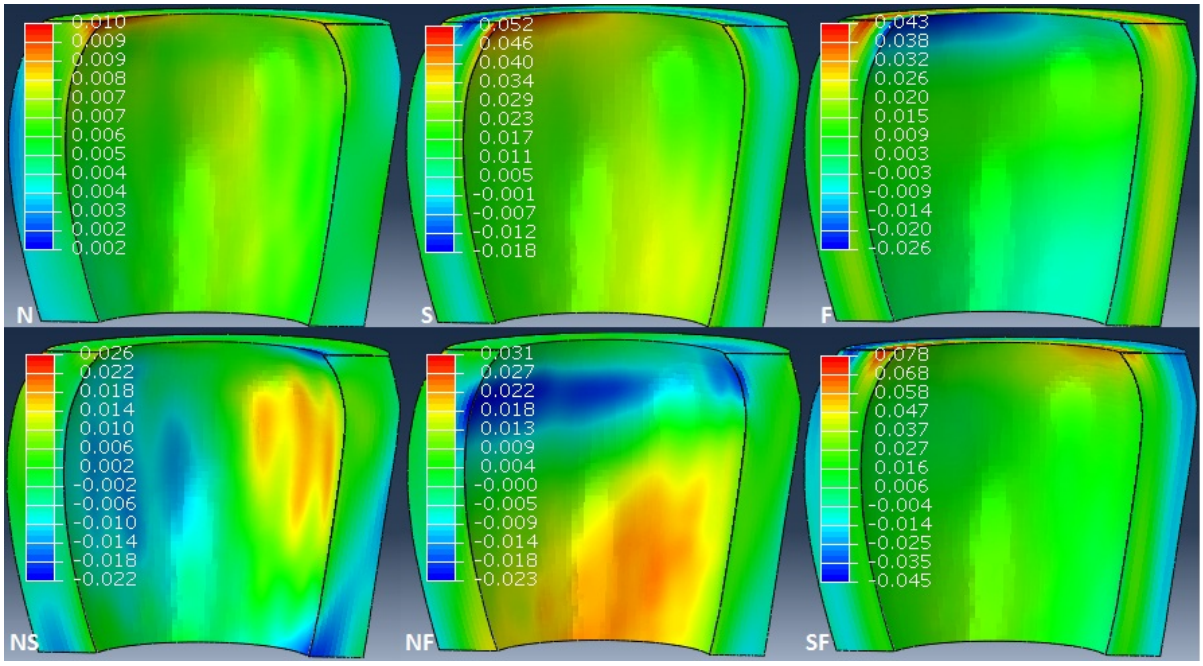

FIGURE 3.9 – Local strains of LV model for the reference random sample of MPs. (N, S, F) stand for normal, sheet and fiber directions.

Other Limitations to this Study

Experimentally, it has been shown that the unloaded myocardium tissue, is residually stressed [Omens and Fung, 1990, Costa et al., 1997]. [Costa et al., 1997] showed that there are little residual stresses along the muscle fiber directions in myocardium mid-wall which is difficult to quantify in 3D space. As a result in this method we ignored these residual stresses which should be explored further.

The main motivation for choosing a simplified model was to limit the number of parameters under study for ES, and thereby facilitate a more detailed analysis. However, [Miller and Lu, 2013] showed that the uncertainties in the organ geometry reconstruction have more dominant effect on deformation than uncertainties on the constitutive model and its MPs for a simple model.

In addition, [Young et al., 2008] suggest that the deformation is insensitive to the mesh density and highly influenced by the accuracy of reconstructed geometry. Our results show that for this simplified model the stress field is, under certain conditions, insensitive to the MPs.

Displacement-driven Simulations

We compared these results (refer to Figure 3.7) with displacement-driven FE analyses results at ES where the displacements of endocardium were extracted from the reference systolic simulation. We propose two methods for ES FE analysis : *displacement-driven* (Dirichlet-type problem) and *pressure-driven* where the pressure is applied on the endocardial surface as mentioned in the article (refer to 3.1.2). To perform displacement-driven FE analysis, we assigned the reference displacement vectors at endocardial boundary nodes (*option 1*) or both at endocardial and epicardial boundary nodes (*option 2*). These approaches could be applied similarly using the deformations from ED to ES that could be measured using a medical imaging technique [Wang and Amini, 2012, Seo et al., 2014]. One may notice that the displacement-driven approach makes the stress maximally sensitive to the MPs which is a correct assumption in general case, but it is not our case because of the active stress presence.

We performed FE analyses for displacement-drive and pressure-driven from ED to ES and estimated the induced Cauchy stress for different sets of MPs (refer to Section 3.1.2) with Mooney-Rivlin strain energy function. Here, it can be expected a significant effect of varying the MPs on the reconstructed passive stress but our objective is to compare the effect of active stress with simple model (Mooney-Rivlin) for more quantitative analysis. Our assumption is that most of the ES blood pressure is balanced by the contractile forces created by myocytes

during systole and then the passive stresses are negligible at ES, whatever the values of MPs used in the model.

Figure 3.10 shows the nodal displacements vectors of LV cavity extracted from the reference FE analysis in mm. We varied MPs (Table 3.1) and performed 40 displacement-driven ES simulations. Figure 3.11 shows lower SD to the variation of MPs in comparison to the pressure-driven case in Figure 3.10. This low variation is due to the unique displacement field that has been applied to the endocardial surface. In this case, the active stress influence less from the variation of MPs and so the SD reduces. It has been also mentioned in detail such simulations without active stress in [Miller and Lu, 2013] for displacement-driven simulations and statistically determinate problems.

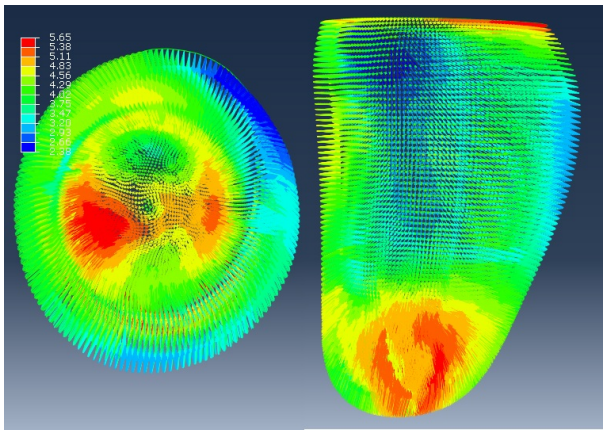

FIGURE 3.10 – The displacement vectors assigned to each node for displacement-driven simulations in mm.

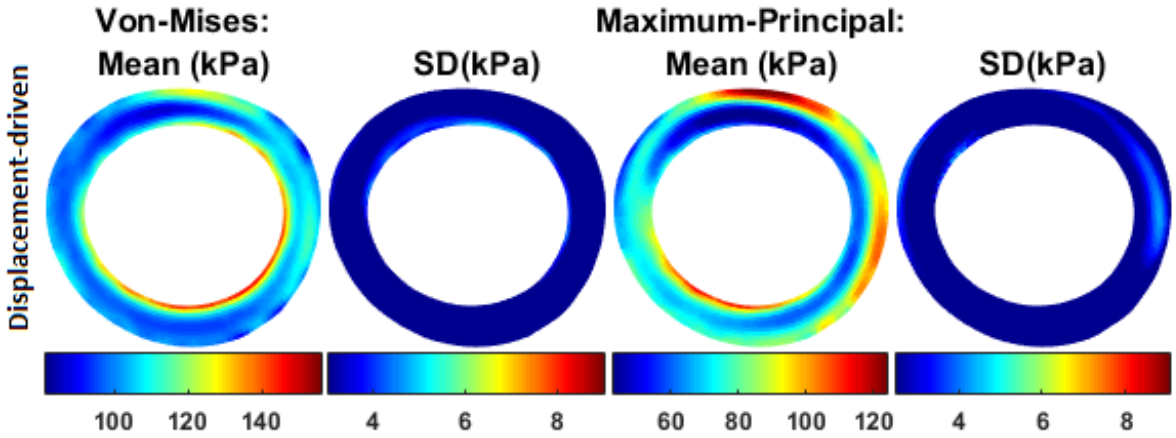

FIGURE 3.11 – The means and SDs of Maximum-Principal and Von-Mises stress results. The displacement-driven ES case where the nodal displacement vectors are prescribed on the endocardium surface.

In our displacement-driven simulations (*option 1*), we always assigned the same deformation to the LV cavity, constraining the passive contribution to remain almost constant whatever the chosen MPs. The SDs of these 40 simulations with random drawings of MPs remain lower than 3% of the actual stresses in terms of Von-Mises and Maximum-Principal stresses.

With *option 2*, in displacement-driven simulations (the results are not shown), the Von-Mises stresses stay insensitive to the variations of MPs, but we observed an increase in SDs for Maximum-Principal equal to 12% of the actual stress results. This increase in stress is due to the compensation of the LV tissue incompressibility which is trapped between two layers with displacement boundary conditions.

These observations confirm the necessity of reconstructing the stress using displacement-driven FE analysis with displacement information in order to minimize the sensitivity to MPs. It is also a validation for displacement-driven simulations of active tissue which shows that it is minimally sensitive to the mechanical parameters in an isotropic material model.

Assigning a deformation to the FE analysis from ED to ES is not a common approach in the literature. It was suggested by [Miller and Lu, 2013, Ciarlet and Mardare, 2009] that displacement-driven FE analysis are insensitive to MPs but require an imaging modality to calibrate the boundary conditions. Such imaging modalities are commonplace in cardiac imaging as deformations from ED to ES could be measured using MRI tagging, dense MRI or US with tracking methods [Frangi et al., 2001, Wang and Amini, 2012, Seo et al., 2014].

Chapitre 4

Générer des maillages spécifiques aux patients à partir d'un modèle de référence

Le travail de ce chapitre concerne une méthode semi-automatique pour générer un maillage personnalisé à partir d'un maillage cible de référence. Les notations peuvent être différentes dans ce chapitre. Ce travail a été soumis dans le journal "IEEE Transactions on Biomedical Engineering2016" et a été présenté lors de la conférence internationale ECCOMAS2016 en Crête et ESB2016 à Lyon. Cette partie est constituée de l'article en anglais, accompagné d'un préambule en français.

Sommaire

Préambule

La génération d'un maillage en hexaèdre est un problème récurrent en vision par ordinateur et en modélisation numérique de tissu mou. Ca peut même devenir un problème difficile, en particulier, quand on veut développer un modèle spécifique au patient du VG pour un calcul d'EFs où seules les images à faible résolution sont disponibles. Dans ce chapitre, un algorithme rapide et efficace est présenté et ensuite testé pour répondre à de telles situations.

L'algorithme peut adapter une géométrie du VG sain (maillée en élément de type hexaèdre) à des géométries de patients qui souffrent de BBG. Il projette les nœuds de l'endocarde et l'epicarde du modèle de référence à la surface (triangulaire) de la géométrie du patient (cible) en utilisant deux types de systèmes de coordonnées (cylindriques et sphériques). Puis avec les informations de ces déplacements, un calcul d'EFs peut déformer les surfaces du modèle de référence avec ses nœuds internes. De cette façon, le modèle de référence va s'adapter à la géométrie de sa cible. Cet algorithme a été appliquée sur huit géométries pour vérifier sa répétabilité et sa faisabilité. Les géométries du patient sont obtenus à l'aide d'un algorithme intégré (EchoPac®) la machine à US de GE Healthcare.

Pour chaque patient, la pression sanguine a été mesurée à l'intérieur du VG. Cette pression a été appliquée sur la surface de l'endocarde pour effectuer une simulation diastolique afin d'analyser la contrainte induite dans la paroi ventriculaire. Cela permet de vérifier la certitude de la méthode appliquée. Les résultats montrent une très bonne carte de contraintes (homogène) pour chaque patient qui montre l'aptitude de cet algorithme. Pour la phase de diastole, le solveur Standard d'Abaqus a été utilisé. Cet algorithme rapide et peu coûteux peut être très prometteur pour les futurs modèles spécifiques aux patients avec des potentiels pour d'autres organes.

4.1 A centerline based mesh morphing algorithm for patient-specific FE modelling of the left ventricle

Sareh Behdadfar, Laurent NAVARRO, Joakim SUNDNES, Molly MALECKAR, Stian ROSS, Hans Henrik ODLAND and Stéphane AVRIL

IEEE Transactions on Biomedical Engineering

ABSTRACT

Objective: Hexahedral automatic mesh generation is a recurrent problem in computer vision and computational biomechanics. It may even become a challenging problem when one wants to develop a patient-specific finite-element (FE) model of the left ventricle (LV), particularly when only low resolution images are available. In the present study, a fast and efficient algorithm is presented and tested to address such a situation. Methods: A template FE hexahedral mesh was created for a LV geometry using a GE ultrasound (US) system. A system of centerline was considered for this LV mesh. Then, the nodes located over the endocardial and epicardial surfaces are respectively projected from this *centerline* onto the actual endocardial and epicardial surfaces reconstructed from a patient's US data. Finally, the position of the internal nodes is derived by finding the deformations with minimal elastic energy. This approach was applied to eight patients suffering from congestive heart disease. A FE analysis was performed to derive the stress induced in the LV tissue by intracavital blood pressure on each of them. Results: Our mesh morphing algorithm was applied successfully and the obtained meshes showed only marginal mismatches when compared to the corresponding US geometries. The FE analyses were successfully performed in seven patients to derive the distribution of principal stresses. Conclusion: The novel mesh morphing algorithm was fast, robust and with small computational cost. Significance: This low cost mesh morphing algorithm may be highly beneficial for future patient-specific reduced-order modelling of the LV with potential application to other crucial organs.

GRAPHICAL ABSTRACT

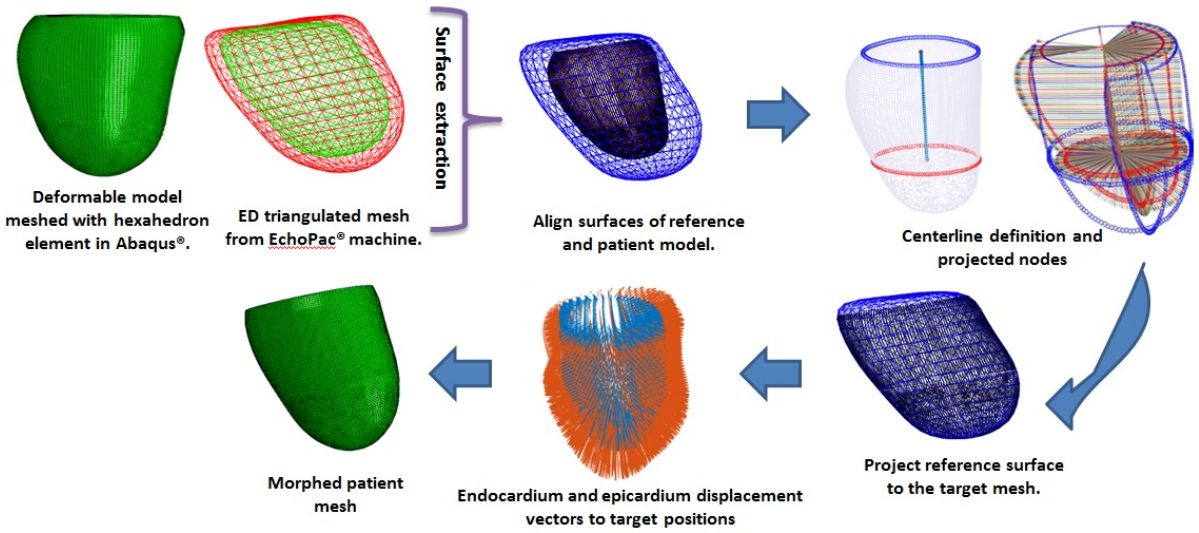

HIGHLIGHTS

— Semi-automatic algorithm to customize a reference fine mesh to a coarse triangulated surface.

— Simple and efficient algorithm for morphing a reference mesh to a target or destination geometry.

— Possible future work: develop the capacity for use in tandem with echocardiography for direct fine FE mesh generation.

KEY WORDS: Mesh morphing ; left ventricle ; GE Healthcare US ; EchoPac® ; cardiac mechanics ; prolated spheroidal shapes.

4.1.1 Introduction

In spite of recent advances in medical imaging and image processing, constructing a patient-specific finite element (FE) mesh of the left ventricle (LV) remains daunting. In addition to the challenges of accurately reconstructing patient anatomy, numerical simulations of cardiac mechanics put strict demands on mesh quality and regularity, as illustrated in [Lamata et al., 2011]. Another issue is that automatic geometry extraction usually provides surface data (stl format). Often, the volume surrounded by this surface can be simply meshed with tetrahedral elements. One example of such method is integrated in GE Healthcare US system named EchoPac® software. The LV is reconstructed in triangulated elements which can be easily converted into tetrahedral meshes [Hansegård et al., 2009].

However, a critical problem arises in meshing an organ with hexahedral elements, the standard choice in 3D solids thanks to their numerical and computational efficiency and accuracy, especially if a large number of patients have to be processed within a reasonable timeframe. Their shape functions, directional sizing without loss, accurate connectivity and decrease in overall elements population in comparison to tetrahedral meshes are the proven essential properties of such elements [Blacker, 2000, Benzley et al., 1995]. In addition, it is easy to consider a local coordinate system for such elements to determine the anisotropic material behaviour of the LV in FE codes. However, automatic mesh generation with hexahedral elements requires a precise knowledge of element shape functions and nodal connectivities in mesh domain which might not be available.

In addition, NURBS-based elements may also be employed with great potential [Marin and Brankov, 2010].An example of such methods was previously developed to reconstruct personalized meshes using cubic elements with a Hermite shape function [Lamata et al., 2011]. The proposed method wraps a predefined NURBS-based high quality template mesh onto the registered images. This interpolation requires a wrapping field from nodal positions and the derivatives of shape function to the local coordinates [Lamata et al., 2010]. However, the success of mesh wrapping intrinsically depends both on the level of image resolution as well as the number of control points appropriately employed. Bad image quality, wrong choice of control points, presence of noise and inaccurate wrapping field may be possible causes of failure or overfitting. We suggest a new approach which overcomes these difficulties for low resolution images by directly projecting a template mesh, called the reference deformable FE (*RDFE*) mesh from a *centerline*, onto a subject's geometry.

The rest of this paper is organised as following: next, the description of this centerline ap-

proach appears. In Section 4.1.3, this original method is used to morph a deformable LV model meshed in hexahedral elements onto the geometry of eight subjects for whom US images were acquired in triangulated surfaces. In Section IV, the FE models reconstructed for these subjects are employed to derive the distribution of principal stresses in the LV wall. Finally, the potential benefits and also some limitations of the presented method are discussed in Section 4.1.5 before concluding in Section 4.1.6.

4.1.2 Methods

General Principle of Mesh Morphing

Mesh morphing and deformable shape registration [Mitra et al., 2007, Huang et al., 2008, Li et al., 2008a] are commonplace in medical computational modelling [Audette et al., 2000, Liu, 2007] and computer vision [Tam et al., 2013]. They must always be preceded by a rigid registration of the target image onto the template. Rigid registration is defined by a translation and a rotation [Tam et al., 2013]. The translation is deduced at the center of gravity whereas the rotation is obtained from the corresponding positions of at least three landmarks using different techniques such as singular value decomposition (SVD).

After the rigid registration, one has to deform the template mesh or the template geometry onto generic 3D data [Papazov and Burschka, 2011, Barber et al., 2007, Couteau et al., 2000, Gibson et al., 2003, Fernandez et al., 2004, Bucki et al., 2010, Li and Guskov, 2005, Sigal et al., 2008]. This can be achieved in three steps:

1. Selection of corresponding landmarks [Van Kaick et al., 2011, Myronenko and Song, 2010],
2. Definition of an objective function and constraints,
3. Optimization of the landmarks' deviations.

A common approach of steps 2 and 3 is the Iterative Closest Point (ICP) algorithm [Liu, 2007, Rusinkiewicz and Levoy, 2001, Amberg et al., 2007]. However, it generally requires the template and subject's geometries to have the same number of nodes [Lamata et al., 2011], which is not always possible to achieve (as in our case).

Therefore, we developed a promising algorithm which can address situations in which the template mesh and the target geometry have a differing structure which is more actual for medical use. This approach deals with the applications on LV shape. We considered an available healthy geometry of LV for this purpose instead of a truncated ellipsoid or other generic data as this method is insensitive to the topology of the reference geometry. Thus, starting from a

simpler model instead of a real LV shape would not change the final results.

Essentially, situations where there is a dense template RDFE mesh for refined FE analyses and a coarse subject's model provided from US images, for instance.

Three stages of this method are to (outlined in Figure 4.1):

1. Align basal surfaces as rigid transformation step.
2. Register only the nodes located on the boundaries of the template RDFE mesh.
3. Register all the intermediate nodes.

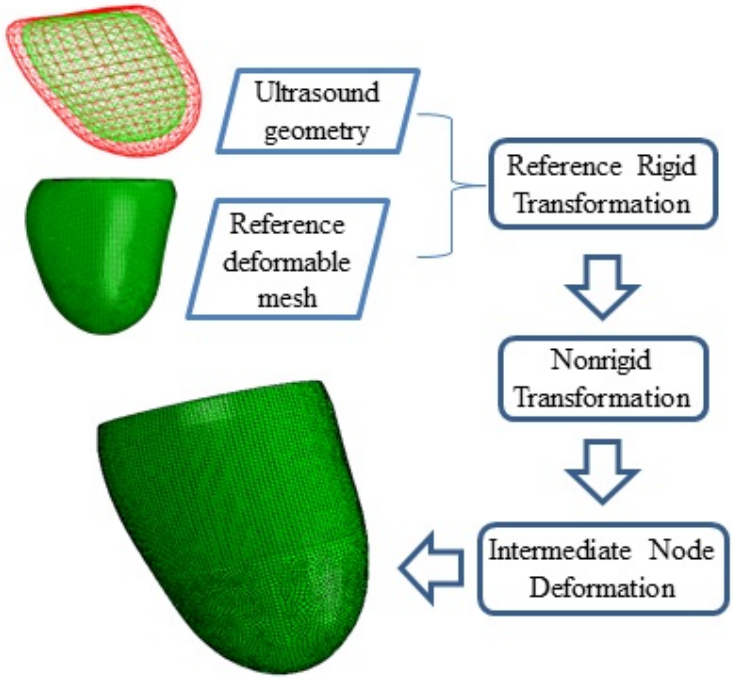

FIGURE 4.1 – Mesh morphing pipeline outlining the three steps of rigid and nonrigid transformation.

Rigid Body Registration Method

We consider two geometries: a RDFE meshed in hexahedral elements (bulk) and a subject's geometry meshed in triangle elements (surface). The approach for registering the boundaries of these geometries consists first in a rigid registration, and then in a projection of nodal positions onto the target surfaces.

Let's consider the endocardial surface of these LV meshes cut at basal surface (refer to Figure 4.2). The template RDFE surface is of size h elements with N number of nodes. Let

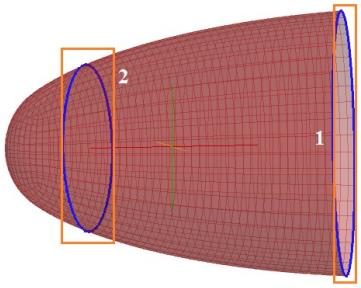

FIGURE 4.2 – An illustration of cut planes for LV geometry. The equatorial plane 1 forms base surface and plane 2 defines the spherical part (apex).

$\mathbf{P}_i{}^h$ ($i \in [1,3]$) be the position vectors of a set of nodes defining a triangle on its basal surface -made of 3 nodes $\mathbf{P}_1$, $\mathbf{P}_2$ and $\mathbf{P}_3$-, then we define the unit normal vector as:

$$\mathbf{N}^h = (\mathbf{P}_2{}^h - \mathbf{P}_1{}^h) \times (\mathbf{P}_3{}^h - \mathbf{P}_1{}^h). \tag{4.1}$$

The target surface is of size h' elements with N' number of nodes. Let $\mathbf{P}_i{}^{'h'}$, be the position vectors of a set of nodes defining a triangle on its basal plain, -made of 3 nodes $\mathbf{P}_1{}'$, $\mathbf{P}_2{}'$ and $\mathbf{P}_3{}'$- then we define the unit normal vector such as:

$$\mathbf{N}'^h = (\mathbf{P}_2{}'^{h'} - \mathbf{P}_1{}'^{h'}) \times (\mathbf{P}_3{}'^{h'} - \mathbf{P}_1{}'^{h'}). \tag{4.2}$$

We have: $h' \ll h$ and $N' \ll N$.

Therefore, the rotation matrix $\mathbf{R}$, the normalized rotation vector of basal normals (axis of rotation) $\mathbf{RV}$, the cross product matrix ($\overline{\mathbf{RV}}$), and the anticlockwise angle θ about the axis ($\overline{\mathbf{RV}}$) can be defined as follows using Rodrigue's formula [Rodrigues, 1840]:

$$\mathbf{RV} = -(\mathbf{N}'^{h'} \times \mathbf{N}^h)/||\mathbf{N}'^{h'} \times \mathbf{N}^h||, \tag{4.3}$$

$$\overline{\mathbf{RV}} = \begin{bmatrix} 0 & -RV(3) & RV(2) \\ RV(3) & 0 & -RV(1) \\ -RV(2) & RV(1) & 0 \end{bmatrix}, \tag{4.4}$$

$$cos\theta = (\mathbf{N}'^{h'}.\mathbf{N}^h)/(||\mathbf{N}'^{h'}.\mathbf{N}^h)||, \tag{4.5}$$

$$\mathbf{R} = \mathbf{I} + sin\theta\overline{\mathbf{RV}} + (1 - cos\theta)\overline{\mathbf{RV}}^2. \tag{4.6}$$

where $\mathbf{I}$ is the identity matrix.

The rotation matrix $\mathbf{R}$ contains an angle θ from $\mathbf{N}'^{h'}$ towards $\mathbf{N}^h$ anticlockwise around the

rotation vector **RV** which reconstructs the unique matrix $\overline{\mathbf{RV}}$. Then we rotate the RDFE rigid body with this **R** matrix to the target mesh.

Nonrigid Registration Method for the Boundaries

We select two points to define a centerline for the RDFE endocardial surface: the first one on the barycenter of RDFE base surface and the second one on the barycenter of apex (refer to Figure 4.2). The centerline is defined on the RDFE mesh since the projection happens from RDFE to the target surface.

From this *centerline*, we consider another vector which starts from this centerline (normal to the centerline) and passes through the RDFE nodes which we denote it as **Ray**. This **Ray** points towards the correct trajectory from the RDFE node to the target surface.

For each RDFE node, we derive the intersection of **Ray** and the target surface based on the **Ray**/triangle intersection algorithm proposed by [Möller and Trumbore, 2005]. This algorithm takes the vertices $\mathbf{T}(\mathbf{V}_1, \mathbf{V}_2, \mathbf{V}_3)$ of each triangle from the target surface and examines whether the current **Ray** from the RDFE centerline to the RDFE current node intersects any triangle on the target or not.

We know that the intersection point of **Ray** and the triangle, denoted by **Int**, should lie in the plane of the triangle. Therefore, we can write a system of equations (4.7) and (4.8).

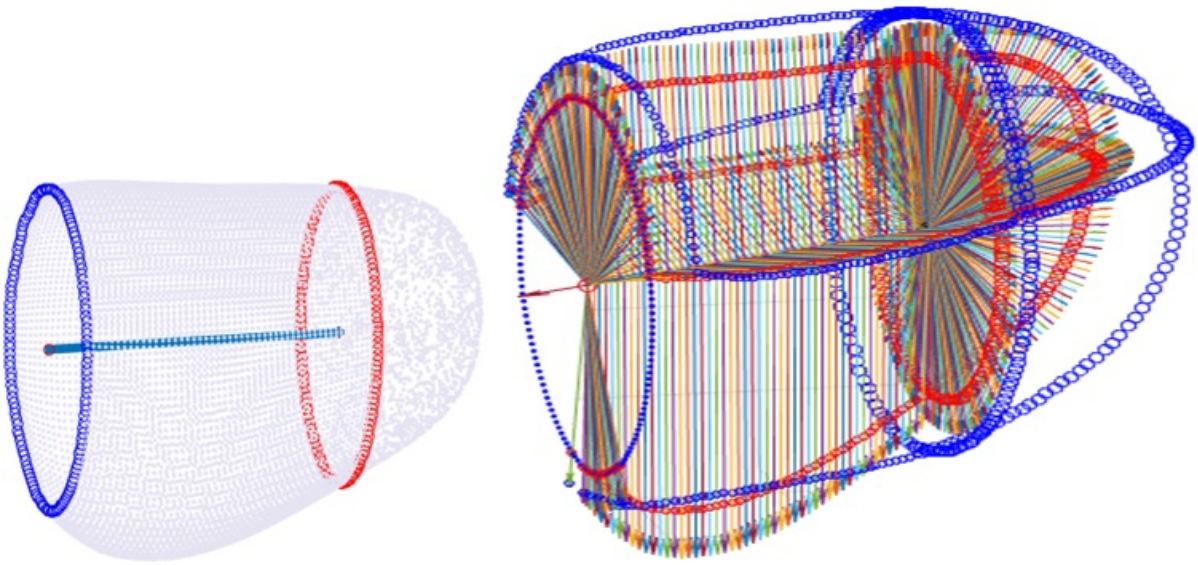

FIGURE 4.3 – The figure shows: left, the centerline which connects the center of apex edge of LV to the center of basal part. Right, several projections of reference nodes in red to the target surface in blue from defined centerline.

$$\mathbf{T}(a,b) = (1-a-b)\mathbf{V}_1 + a\mathbf{V}_2 + b\mathbf{V}_3, \tag{4.7}$$

$$\mathbf{Int} = O + t\mathbf{D}. \tag{4.8}$$

where $\mathbf{T}(a,b)$ is the barycenter coordinates of the current triangle ; t is the distance (unknown) from the **Ray** origin (**O**) to the intersection point **Int** with direction **D**.

Then we need to solve the equation $\mathbf{T}(a,b) = \mathbf{Int}$:

$$O + t\mathbf{D} = (1-a-b)\mathbf{V}_1 + a\mathbf{V}_2 + b\mathbf{V}_3, \tag{4.9}$$

Denoting $\mathbf{e}_1 = \mathbf{V}_2 - \mathbf{V}_1$ and $\mathbf{e}_2 = \mathbf{V}_3 - \mathbf{V}_1$, 4.9 can be rewritten such as:

$$\begin{bmatrix} \mathbf{D} & \mathbf{e}_1 & \mathbf{e}_2 \end{bmatrix} \begin{bmatrix} t \\ a \\ b \end{bmatrix} = O - \mathbf{V}_1, \tag{4.10}$$

Based on Cramer's rule:

$$\begin{bmatrix} t \\ a \\ b \end{bmatrix} = 1/(\begin{vmatrix} \mathbf{D} & \mathbf{e}_1 & \mathbf{e}_2 \end{vmatrix} \begin{bmatrix} \mathbf{S} & \mathbf{e}_1 & \mathbf{e}_2 \\ \mathbf{-D} & \mathbf{S} & \mathbf{e}_2 \\ \mathbf{-D} & \mathbf{e}_1 & \mathbf{S} \end{bmatrix}). \tag{4.11}$$

where $\mathbf{S} = \mathbf{O} - \mathbf{V}_1$.

Solving (4.11) gives three parameters (t,a,b) which should fulfil several conditions. The first condition is that **Ray** should intersect the triangle. We begin by calculating the determinant $det = \mathbf{e}_1.(\mathbf{Ray} \times \mathbf{e}_2)$ and if the determinant is below $1e-5$, the **Ray** is parallel to the triangle.

Then, we calculate $u = det^{-1}(\mathbf{Ray} \times \mathbf{e}_2).(\mathbf{Ray}_{origin} - \mathbf{V}_1)$ and $v = det^{-1}\mathbf{Ray}.((\mathbf{Ray}_{origin} - \mathbf{V}_1) \times \mathbf{e}_1)$. If $(u,v) < 0$ and $(u, u+v) > 1$, then the intersection lies outside of the triangle. Finally, two triangles are found candidates which one is on the correct direction of the current **Ray**. The correct intersection position should be on the line from centerline to the RDFE node ($t > 0$). This process is repeated for all the RDFE surface nodes and the 3D coordinates of intersection points are saved (Figure 4.3). The epicardial RDFE surface nodes were also projected on the respective target surface.

The presented approach in Sections 4.1.2-4.1.2 was developed using an in-house program coded in Matlab®.

Registration Method Across the Bulk Volume

In order to deform the intermediate nodes across the bulk, the displacements of the RDFE boundaries are used to define a classical linear elastic Dirichlet problem on the continuous RDFE 3D volume. We refer to Hooke's law of basic continuum mechanics [Holzapfel, 2002, Bonet and Wood, 1997]:

$$\sigma = \mathcal{C}\varepsilon. \tag{4.12}$$

where $\mathcal{C}$ is the fourth-order elasticity tensor, ε is the elastic deformation and σ is the Cauchy stress tensor.

Boundary conditions for the Dirichlet problem are the known displacements of the RDFE surface determined as explained in the previous section:

$$\mathbf{u} = \overline{\mathbf{u}}. \tag{4.13}$$

where $\overline{\mathbf{u}}$ is the prescribed displacement vector on the boundaries $\partial\Omega_{\mathbf{u}}$.

4.1.3 Application on Cohort Data

To validate our approach we applied it to the LV of eight patients and performed FE stress analyses with the obtained morphed meshes.

Data Acquisition

To reconstruct the RDFE geometry, the LV of a healthy volunteer was segmented at ED from EchoPac® US scan (GE Healthcare) [Hansegård et al., 2009]. Then, the RDFE mesh was precisely created with 8-noded linear brick (hexahedral) elements with $N = 155172$ nodes and $h = 141405$ elements by Abaqus® software tools.

Imaging data from eight heart failure patients with left bundle branch block (LBBB) eligible for cardiac resynchronization therapy (CRT) were obtained from the Impact study [CCI-Impact, 2016]. LV geometries (Figure 4.4) were measured throughout the cardiac cycle with cardiac US, and post processing of the US images were performed in the Echopacc® Software (GE Healthcare) at admission to the Hospital. Pressure curves were acquired during the implantation procedure of the CRT with an indwelling left ventricular transcutaneous intracardiac pressure catheter (MicroCath, Millar Instruments). Pressure curves were stored in the LabChart data acquisition software (Adinstruments Inc.).

The target geometries were closed surfaces of endocardium and epicardium which were

meshed with triangulation algorithm in EchoPac® [Hansegård et al., 2009]. The formal is: $N' = 1282$ nodes and $h' = 2558$ elements. This is the situation that we described in Section 4.1.2: $h' \ll h$ and $N' \ll N$.

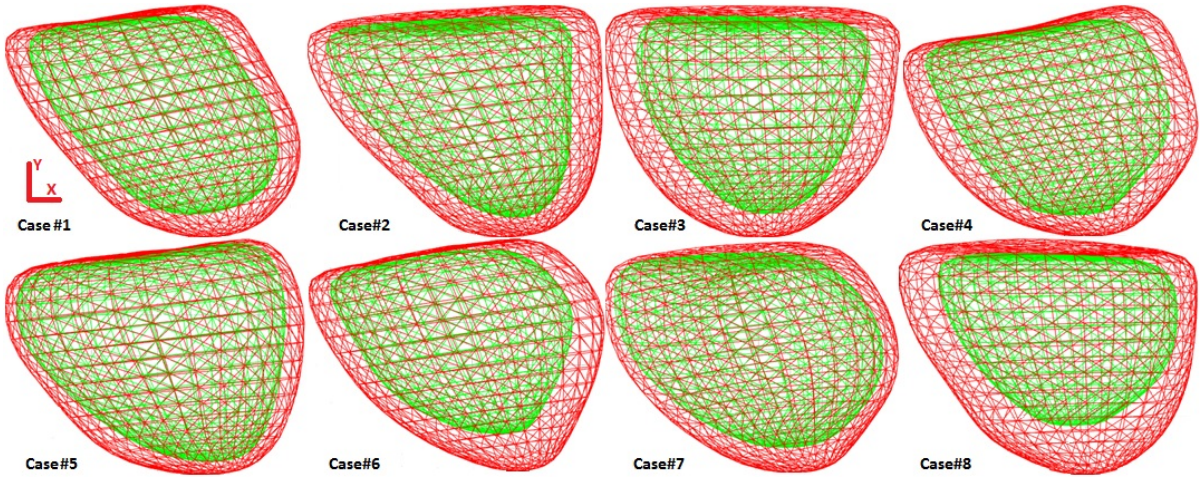

FIGURE 4.4 – The LBBB patient geometries obtained from EchoPac® postprocessing on GE US data. Endocardium and epicardium shown in green and red, respectively

Mesh Morphing Method Application on Cohort

We registered and projected the RDFE boundaries to each patient as previously explained above (Sections 4.1.2-4.1.2). The continuum deformation of intermediate nodes is modelled with elastic properties of Young's modulus and Poisson's ratio equal to $2e06$ MPa and 0.35, respectively. These material parameters provided a reasonable deformation of RDFE 3D model to the target geometries. For this, we ran several simulations with different Young's moduli and Poisson's ratios to study the deformation of deformed RDFE mesh and compared the morphed results with patient geometry. This process was performed using FE Abaqus® software.

As the RDFE geometry is an open cavity surface, the final result that should be expected is a morphed open cavity with bulk LV tissue for morphed patient data.

Cohort Diastolic Phase FE Simulation

We applied the developed mesh morphing method on all patient's geometries at the end-systole (ES) and end-diastole (ED) phase (see Figure 4.5 for ED) in their pressure-volume curve.

For diastolic phase, we used the Guccione strain energy function W for a nearly incompressible and transversal isotropic material model [Guccione et al., 1991] that has been developed

in Abaqus® software with parameters in Table 4.1 [Okamoto et al., 2000].

$$W = \frac{1}{2}c(exp(Q) - 1) + U(J), \tag{4.14}$$

where Q is:

$$Q = b_1\overline{E}_{ff}^2 + b_2(\overline{E}_{ss}^2 + \overline{E}_{nn}^2 + 2\overline{E}_{sn}^2) + b_3(2\overline{E}_{fs}^2 + 2\overline{E}_{fn}^2), \tag{4.15}$$

where, c and b_{1-3} are the material parameters, $\overline{E}_{ij}$ are the components of the distortional Green-Lagrange strain tensor in the local coordinate system in *fiber, sheet* and *normal to sheet* directions, and $U(J)$ is the volumetric part of the strain energy function [Ateshian and Costa, 2009].

$U(J)$ in the FE simulation was defined as a function of bulk modulus K and with J being the determinant of the deformation gradient.

$$U(J) = K(\frac{(J^2 - 1)}{2} - ln(J))/2. \tag{4.16}$$

A local curvilinear coordinate system aligned along the fiber direction was considered to model myocyte contraction [Huyghe et al., 1992]. Fiber directions varied from -70° at the endocardial surface to 60° at the epicardial surface, where 0° is the circumferential direction.

In order to avoid the rigid body motion in FE simulations, the basal nodes were allowed to deform radially. We applied the corresponding patient's cavity pressure (refer to Table 4.2) from ES to the ED to the endocardial surface and performed diastolic simulations.

TABLE 4.1 – Material parameters proposed in [Okamoto et al., 2000].

$c(Pa)$	b_1	b_2	b_3	$K(kPa)$
512	67.1	24.2	21.6	0.1

TABLE 4.2 – Cavity pressure obtained from LBBB patients.

Case	♯1	♯2	♯3	♯4	♯5	♯6	♯7	♯8
Pressure (kPa)	3.2	4	1.333	3.2	0.4	3.6	1.84	3.466

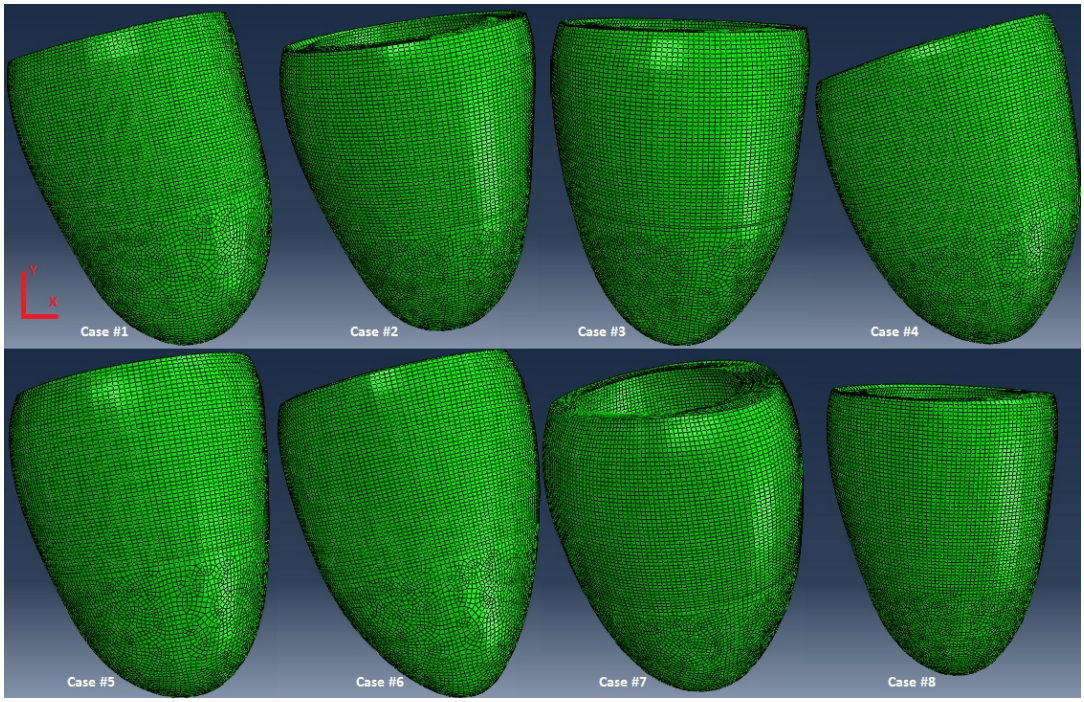

FIGURE 4.5 – The figure shows the application of developed mesh morphing method on LBBB patient geometries obtained from EchoPac® US.

4.1.4 Results

The method outlined in Figure 4.1 was applied for all patients in Figure 4.4, as shown in Figure 4.5. The boxplot in Figure 4.6 illustrates the nodal error for projected nodes and deformed surfaces as in Section 4.1.2. This error is the distance difference between projected nodes on the target surface and the result after intermediate nodes FE deformation. The results demonstrate a minimum error for the Cases ♯1, ♯2, and ♯4 to ♯8 with less than 0.1 mm of median error. The residual error observed is quite small which is related to the machine error. The registration and projection method for each surface (Matlab®) took less than 10 min on a 2 core PC (Intel $i5-4590$ 3.3 GHz 8Go RAM) and the intermediate deformation (Abaqus®) takes about 5 min on 8 cores (Intel Xeon X5650 2.67 GHz 24Go RAM). The total process for each patient uses approximately 25 min of wall time.

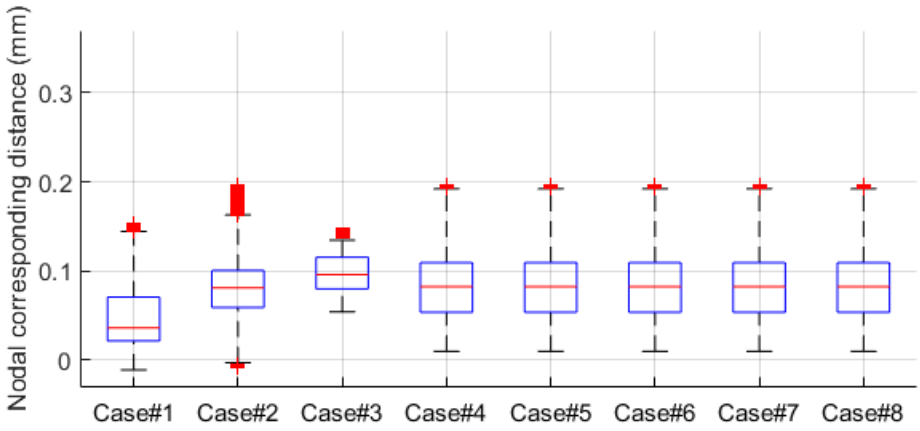

FIGURE 4.6 – The boxplot is the error between projected nodal positions on the target and the results after application of intermediate node deformation step in Abaqus® software. The error is the Eulerian distance.

An illustration of the diastolic phase is shown in Figure 4.7. For Case ♯1, ♯2, ♯4, ♯6, and ♯8, we observed a homogeneous distribution of principal stresses through the wall thickness which highlights the high quality of the morphed meshes. In Case ♯3 and ♯5 we have noticed several elements at both base and apex which have different values than their surroundings. This shows that the methodology can be sensitive to the conical shape of the apex in terms of quality of deformed elements. The basal differences in this cases might be due to the applied boundary conditions to the basal nodes which limit some degrees of freedom for rigid body deformation. Case ♯7 had no convergence success.

Table 4.3 contains the intracavital volume obtained from FE ED simulations and patient's

data. There are small differences in final intracavital volume which is due to the tissue material parameters.

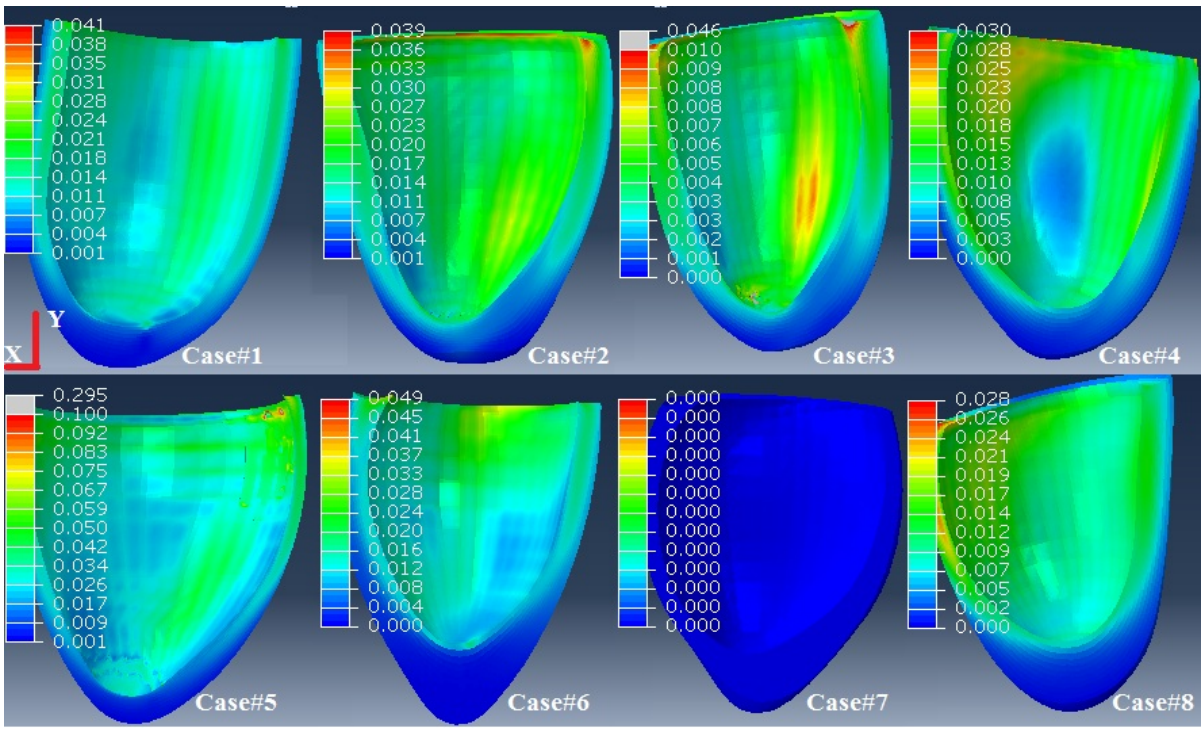

FIGURE 4.7 – The principal stresses results of ED FE simulations. Case ♯7 has not been converged in these FE simulations.

TABLE 4.3 – ES and ED cavity volume.

Volume(ml)/Case	♯1	♯2	♯3	♯4	♯5	♯6	♯8
ED (EchoPac®)	163	168	168	154	319	151	112
ED(FE)	166	164	167	128	266	174	98
ES	113	144	133	106	233	103	78

4.1.5 Discussion

In general, nonrigid registration is a challenging problem and it is dependent on the input data. It is also treated as a nonlinear optimization problem [Lorusso et al., 1995], [Sahillioğlu and Yemez, 2012], [Myronenko and Song, 2010]. However, the local optimization methods may become stuck in local optima if not properly initialized. A better option can be a global optimization algorithm that does a complete search to find a global solution.

Here, we developed a novel approach for simple patient-specific nonrigid transformation of biological organs without considering it as an optimization problem. We avoid these optimization difficulties and overfitting problems as discussed in [Lamata et al., 2011]. The advantage is that our algorithm did not need physical correspondence on both geometries for projection and additionally produced meaningful, physiologically relevant results. It also does not require a priori assumption or constraints to project the RDFE 3D surface to the target surface. However, the optimization methods become more interesting where the reference geometry is too coarse and its topology does not precisely representing the target geometry. The ability to ignore target mesh problems as gaps, overlaps and holes is one of the important properties of this developed approach.

We have developed a method to morph a deformable LV model to the patient LV data in the case where RDFE and target meshes are very different in density. Previously, [Huyghe et al., 1992] developed a centerline method for arteries. It worked by moving a Voronoi sphere on the average centerline of the artery and finding the intersect positions of this sphere with the target shape. Their developed approach is valid on topologies close to the arteries and it is not applicable to conical shapes such as the LV. Our developed method is also based on the centerline of the LV, but instead we project the RDFE nodes from this centerline to the target surface.

The application of this method is fast, efficient, and simple to implement as a pipeline. It takes less than 25 minutes to morph a RDFE model to the target surfaces with the help of Matlab® and Abaqus® software.

Several methods have been developed for volumetric deformation, such as different models of heat kernel signature or heat diffusion processes on a shape [Sun et al., 2009, Ovsjanikov et al., 2010,Bronstein and Kokkinos, 2010,Raviv et al., 2010], wave heat kernel signature based on quantum mechanics [Aubry et al., 2011] and differential deformation scheme [Zhang et al., 2008]. These methods require a sufficient knowledge of these fields for their correct applications.

The linear elastic transformation method has been used previously for this purpose in lite-

rature [Broit, 1981, Bajcsy et al., 1983, Davatzikos and Bryan, 1996, Davatzikos, 1997]. Authors of [Holden, 2008] reviewed and compared the application of elastic transformation in medical imaging and continuum mechanics problems. In order to deform the RDFE solid model with intermediate nodes, we used elastic body deformation using FE simulation. It is applicable using any FE software and simple to develop without precise knowledge of continuum mechanics and FE simulation.

Material parameters were chosen to obtain the best intermediate node deformation. The Young's modulus and Poisson's ratio have an important impact on the model behavior of the FE geometry. If the material is compliant, the boundaries deform and the internal nodes remain at their initial positions. The FE elastic simulation had the best results with high Young ?s modulus and relatively small Poisson ?s ratio values.

Limitations and Future Work

One disadvantage of this method is that during the elastic deformation, some elements lost their volume due to the variation in wall thickness and the nature of RDFE element type (hexahedral). In the intermediate node deformation, we perform a FE simulation once and the model deforms. In this case, the elements can reach their limits of deformation or can become smaller due to the low Poisson's ratio value. It is not critical itself, but becomes critical if another FE simulation is started from this resulting mesh in which the morphed geometry can fail to achieve FE convergence. It was necessary, in this case, to remove these elements which were concentrated on the endocardial apex and basal boundaries manually as a post-processing step for FE simulations of diastole. This choice is justified due to the importance of elements at domain boundaries for intracavital applied pressure which are highly sensitive to the element's quality. This issue has been observed in [Lamata et al., 2011] as well. It is also the cause for generated stress heterogeneities at the apex and basal regions in Cases ♯3, ♯5 and ♯6. We have noticed that the zones related to the removed elements fits to these heterogeneities.

Another limitation is this the method is based on a centerline projection ; so, if the geometry has several layers, they should be treated separately with their RDFE corresponding surfaces. In this paper, we treated the endocardium and epicardium surfaces separately from their reference centerlines to the target surfaces.

As future work, one might apply this method on biventricular or complete heart meshes to verify the feasibility and reproducibility of this method in shape analysis and computer vision problems. In case of biventricular geometries, a potential improvement is to define two

centerlines each for the LV and right ventricle for both endocardium and epicardium, and then to project the reference surfaces. This will be much more challenging if the complete heart is considered, due to the importance of the centerline definition. Then, one could define a complex network of centerlines in a complete heart. Here, we examined the developed methodology specifically on LV morphology alone.

Another improvement may be to identify the strain energy function material parameters for each patient with their pressure volume curves to achieve more meaningful results during the diastolic FE application. Lack of constraint in this manner likely explains differences in the final ED volume from patient's data and the FE simulations at ED in Table 4.3.

4.1.6 Conclusion

In this paper, a new methodology was presented to morph a deformable generic mesh onto a patient-specific geometry in the case where the density of the generic mesh is at least 10 times larger than the density of the available nodes for the patient-specific geometry. The method showed very promising results for patient-specific FE analyses of the LV on a cohort of 8 patients suffering from LBBB disease. It is now ready to be used in a patient-specific simulation pipeline based on medical imaging techniques. It could also be applied to different organ systems such as arteries, brain, and bones.

Acknowledgements

The authors gratefully acknowledge the support and data provided by the Center for Cardiological Innovation, funded by the Research Council of Norway.

Chapitre 5

Détection de la zone de tissu anormal et estimation de la contrainte moyenne active chez les patients présentant un dysfonctionnement du VG

Dans ce chapitre, la contrainte moyenne active est identifiée pour une cohorte de 8 patients BBG. Un post-traitement permet de reconstruire des cartes de contraintes et de déformation permettant une analyse des effets de la pathologie sur le remodelage de la paroi du VG. Ce travail a été présenté lors de la conférence internationale ECCOMAS2016 en Crête et ESB2016 à Lyon. Le chapitre est rédigé sous la forme d'un article en anglais, précédé d'un préambule en français.

Préambule

Ce travail tente d'explorer le comportement mécanique de la paroi du VG chez une cohorte de 8 patients 15 jours après avoir subi un traitement de resynchronisation cardiaque. L'objectif est de détecter des zones encore potentiellement infarctées. Les patients ont été recrutés après consentement éclairé au Rikshospitalet, Oslo, Norvège. La géométrie du VG, les déformations régionales et les courbes volume-pression ont été mesurées tout au long du cycle cardiaque en utilisant l'échographe 4D EchoPac de GE Healthcare ® suivant les normes de l'AHA.

Le bloc de branche gauche (BBG) est un trouble de la conduction cardiaque qui se manifeste par un retard dans la contraction du VG par rapport à la contraction du ventricule droit. L'électrocardiogramme est un outil couramment utilisé pour détecter cette dysfonction qui provoque un élargissement du QRS. Le BBG est dit complet si le QRS est élargi de $t > 0,12$ seconde et incomplet si la durée de QRS est de $0.09 < t < 0,12$ seconde. Le traitement préconisé pour les patients atteints de BBG est souvent la resynchronisation cardiaque.

Des analyses de contraintes par la méthodes des EF ont été réalisées sur Abaqus® pour étudier le comportement du VG. Les maillages de chaque patient ont été obtenus par une approche de morphing qui déforme un maillage de référence formé d'éléments hexaèdres pour l'adapter à la géométrie de chaque patient et pour chaque étape du cycle cardiaque pour lesquels des géométries ont été acquises par échographie. Les nœuds du maillage déformable ont d'abord été projetés sur des surfaces cibles. Ensuite, le calcul des contraintes a été réalisé. La loi de comportement du tissu cardiaque a été représentée par un modèle hyperélastique.

Le comportement actif a été modélisé par une précontrainte appliquée selon les orientations des fibres à travers l'épaisseur du myocarde. La détection des zones potentiellement infarctées a été réalisée en trois étapes : 1. Identification d'une précontrainte moyenne qui équilibre la pression intracavitaire à la fin de la systole. 2. Prédiction de la déformation induite par une telle précontrainte lorsqu'elle est appliquée au modèle pour prédire l'état du myocarde en fin de systole. 3. Comparaison des déformations ainsi estimées aux déformations régionales mesurées en fin de systole par le système échographique.

Dans un premier temps, la méthode de détection des zones potentiellement infarctées a été validée avec succès sur des données synthétiques simulant une ischémie aiguë. Elle a révélé les zones infarctées avec un contraste bien supérieur à celui observé sur les cartes de déformation de l'échographie. Elle a ensuite été appliquée sur les 8 patients atteint de BBG. Les résultats révèlent des zones d'hétérogénéités modérées qui correspondent également à des hétérogénéités

de la déformation radiale mesurée en échographie. Les hétérogénéités étaient moins prononcées que celles qui révélées pour les cas simulés d'ischémie aiguë. Ces zones sont souvent de plus faible épaisseur et la méthode a bien révélé un mouvement anormal du myocarde dans les régions concernées. La méthode a également révélé que le tissu tend à être plus rigide dans la paroi latérale des patients étudiés. Des limites à la méthode ont toutefois été mises en évidence, notamment le fait que d'autres hétérogénéités de type artefacts puissent apparaître à cause de la géométrie du myocarde de certains patients ou à cause des variations d'épaisseur de paroi.

En conclusion, cette étude a illustré l'importance des géométries patient-spécifiques pour réaliser des simulations réalistes. L'utilisation d'un méthode simple a permis d'identifier rapidement les hétérogénéités de la contrainte active. Il serait intéressant pour la suite de comparer les reconstructions faites à différents stades de remodelage après le traitement de resynchronisation cardiaque.

5.1 Abnormal tissue zone detection and average active stress estimation in patients with LV dysfunction

Sareh Behdadfar, Laurent NAVARRO, Joakim SUNDNES, Molly MALECKAR,
Hans Henrik Odlan and Stéphane AVRIL

ABSTRACT

Detection of ventricular dysfunction is a challenging problem. In this context, image-based finite-element (FE) simulations become a leading tool to detect the abnormal movement in the left ventricle (LV). The objective of this study is to present an efficient method for this purpose and apply it in different pathological cases using Ultrasound (US) technique. Our hypothesis is that a homogeneous contraction is a sufficient assumption for a healthy LV, therefore, the region with maximum deviations between image-based measured deformation and the FE simulation results might be related to an abnormal zone. Our detection method of potentially injured areas, based on this hypothesis, was carried out in three stages : 1. Identification of an average prestress which balances the intracavity pressure at the end-systole (ES). 2. Estimation, numerically, the deformation induced by such prestress when applied to the myocardium tissue at end-diastole to ES. 3. Comparison of the deformations thus estimated with the regional deformations measured at ES by the US system.

As the first step, the method for detecting potentially infarcted areas was successfully validated on synthetic data simulating an acute ischemia. It revealed the infarcted areas with a contrast much higher than that observed on the deformation maps.

For this purpose, a cohort of eight left bundle branch block (LBBB) patients was available from Rikshospitalet, Oslo, Norway. This work attempts to explore the mechanical behaviour of the LV wall and to detect potentially infarcted areas in this cohort 15 days after undergoing cardiac resynchronization therapy. The LV geometries, regional strains and volume-pressure curves were measured throughout a cardiac cycle using the GE Healthcare 4D tracking EchoPac® US system following American Heart Association (AHA) standards.

We morphed a deformable mesh onto the geometry of each patient for two phases of cardiac cycle where US geometries were acquired. For this, nodes of the deformable mesh were projected onto the target surfaces. Efficient and fast patient-specific FE simulations were performed in Abaqus® software. The constitutive properties were assigned to the tissue by modelling the

material as hyperelastic. The contraction behaviour was modelled through active stress assigned with appropriate fiber orientations at each layer of FE across the myocardium thickness. The results revealed zones of moderate heterogeneities which also corresponded to heterogeneities of the radial strain measured with the US system. The heterogeneities were significantly less pronounced than that revealed for the synthetic cases of acute ischemia. They were often in areas of smaller thickness and the method revealed well the abnormal movement of the myocardium in the concerned regions. The method also revealed that the tissue tends to be stiffer in the lateral wall of LBBB patients. Limitations to the method have, however, been demonstrated, including the fact that other artefact-type heterogeneities may occur due to the myocardial geometry of some patients or due to variations in wall thickness.

In conclusion, this study illustrated the importance of patient-specific simulations in cardiac biomechanics. The use of a simple method permitted to quickly identify the heterogeneities of the active stress in acute ischemia case. Further work is required to transfer the promising synthetic results to real acute ischemic patient cases. In the future, it would be interesting to compare the reconstructions made at different stages of remodelling after the cardiac resynchronization treatment.

GRAPHICAL ABSTRACT

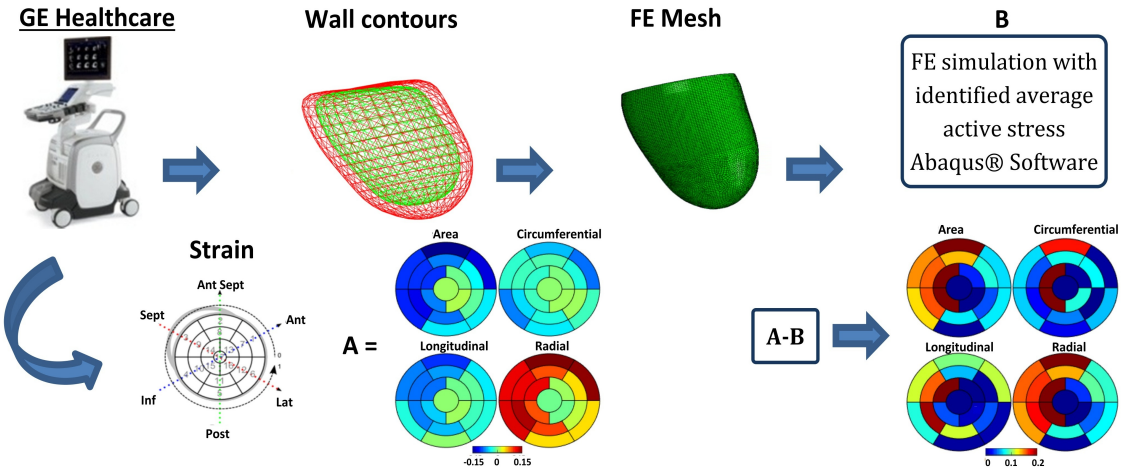

HIGHLIGHTS

— Efficient patient-specific finite-element simulations of left ventricle deformations for a cohort of patients.

— Fast identification of the heterogeneities of the active stress corresponding to abnormal tissue areas in LV.

— Tissue tends to be stiffer in the lateral wall of LBBB patients.

KEY WORDS : Acute ischemia ; left ventricle ; cardiac mechanics ; GE Healthcare US ; EchoPac® ; cardiac mechanics.

5.1.1 Introduction

Realistic finite element (FE) simulation of regional defects caused by pathologies such as acute ischemia remains a significant problem for physiologically based FE analysis of the heart. From the moment that the cell death starts to the thinning and the expansion of the scar surface of myocardium tissue, it lasts approximately 21 days before the remodelling phase starts [Fishbein et al., 1978]. Therefore, an accessible method to detect and characterize the influenced region can provide a better plan for diagnosis of these patients with medications and myocardial injection to avoid tissue progressive remodelling [Sabbah et al., 2013, Lee et al., 2013].

Tracking the deformation of the LV has been actively pursued for the last decades, but important information is lacking about in-vivo wall stress reconstruction in medical imaging modalities for computational purpose [Veress et al., 2011]. However, precise FE models stay limited to the medical imaging research with high resolution multimodalities machines which are often not accessible to clinical routines.

Generally, the primary tool for ischemia detection is the analysis of standard Electrocardiogram (ECG) signals. The majority of research focus for mathematical and computational tools of ischemic zone detection were addressed by electro-physiology models [Sundnes et al., 2006, Sundnes et al., 2007, Zemzemi, 2009, Shi et al., 2010, Oduneye et al., 2015]. An alternative method for ischemia detection is to assess cardiac function with magnetic resonance imaging (MRI) modalities. However, the abnormal zone detection in MRI modalities is limited and remains a challenging problem [Underwood et al., 1986, Wael et al., 2016, Ibrahim, 2011]. In this context, the speckle tracking technique which employs the non-invasive ultrasound (US) [Okrasinski et al., 2012] has became a much used technique in clinical daily practice [Dandel and Hetzer, 2009] due to the accessibility of this system.

In this paper, we study the possibilities of computing a region of abnormal function from 4D strain acquired with the EchoPac® system. The strain estimates are based on speckle tracking, and capture 3D strain through time for 17 LV regions based on the standardized segments of the American Heart Association (AHA), [Cerqueira et al., 2002].

Coupling US data with computations based on the FE method may provide more detailed information about the mechanical state of the patient's heart. The purpose of the present paper is to apply FE simulations to detect regions of abnormal function in the LV, based on the hypothesis that a homogeneous contraction is a regional assumption for a healthy LV, and large deviation between measured deformations and FE simulations based on homogeneous

contraction will correspond to an abnormal region. We aim to investigate the validity of this hypothesis using the 4D strain data acquired with EchoPac®.

The paper is organized as follows. First, we present an overview of our pipeline and of the equations for the systolic phase of the heart cycle. Next, we test the accuracy of the method using synthetic data, simulating zones of acute ischemia in the LV. Finally, the methodology is applied to the cohort patients with left bundle branch block (LBBB), and we discuss the results and the strengths and limitations of the proposed method.

5.1.2 Material and Method

Akinetic or dyskinetic regions such as ischemic regions or infarcts may be detected in medical images as regions of abnormal deformation. However, healthy tissue surrounding a pathological region may also show abnormal patterns of deformation, which makes it challenging to locate the pathological region. The purpose of the present paper is to investigate an alternative method for detecting abnormal regions, by comparing measured strains with strains resulting from a homogeneous contraction. As noted above, the underlying hypothesis is that the healthy contraction is approximately homogeneous [McVeigh et al., 1998, Wyman et al., 1999], and the largest deviation will therefore be associated with the pathological region. To test our hypothesis, we propose to :

1. Build a patient-specific mesh from the images (using an in-house mesh morphing method),
2. Apply a uniform contraction and tune this to give the closest match to the patient's strain data,
3. Evaluate the spatial deviations, and compare the region of largest deviation to the (known) regions of abnormalities.

These main steps of the methodology are also illustrated in Figure 5.1. When applying the algorithm to the patient data, it is necessary to generate a patient-specific FE mesh for each individual case. This task is accomplished by a previously developed mesh morphing method, which takes a generic LV mesh and adapts it to the patients' image data. For each patient specific mesh, the algorithm assumes a constant value for actively generated stress, denoted average active stress (AAS), and performs a systolic FE simulation. Then, the resulting regional strains are compared with the patient's data, and a minimization procedure is performed to minimize the deviation between measured and simulated regional strains. The final, minimized, deviation

is then visualized and analysed in order to locate regions of dysfunctional LV segments.

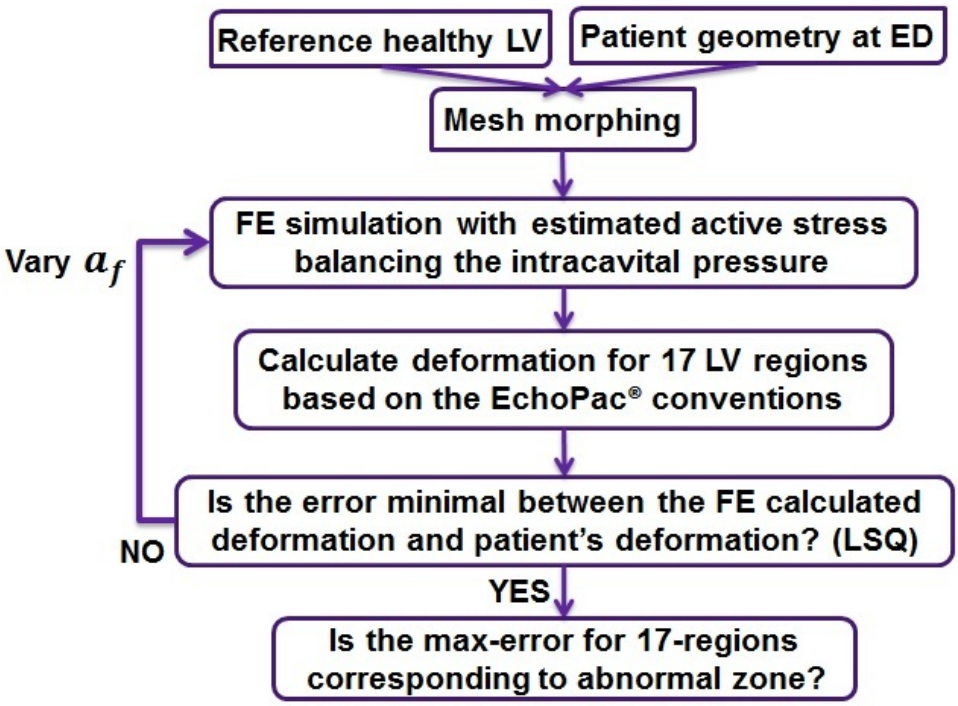

FIGURE 5.1 – The developed patient-specific pipeline. First, we morph a reference FE mesh to the patient data, and then we estimate an AAS to minimize the deviations between FE simulation and the patient data. Finally, we compare these results to detect the abnormal zone.

The main reason why we focus on the systolic phase is that in acute ischemia, the passive behaviour of abnormal zone during diastolic phase stays intact whereas the first appearance of defected region is during the active contraction [Veress et al., 2011]. As a result, remodelling of abnormal tissue leaves a different deformation due to the average stress in regional LV motion.

Reference FE Simulation Model for Systolic phase

To examine the abnormal tissue size effects on the global and regional deformation, we need to explain the model which was used for FE systolic phase. We employed a healthy volunteer LV extracted from 4D US [Hansegård et al., 2009] at end-diastole (ED). The 3D mesh with 8-noded linear hexahedral elements was created using Abaqus® mesh generation software (Figure 3.1). The reference mesh had 155172 nodes and 141405 elements.

To incorporate the known material anisotropy of the LV during the systolic phase, we defined a local curvilinear coordinate system aligned with the local fiber orientation, to model

myocyte contraction [Huyghe et al., 1992, Bovendeerd et al., 1994]. We assumed a helical fiber distribution, with a helical angle varying from -70° at the endocardial surface to 60° at the epicardial surface (0° is the circumferential direction). At each point we defined a local orthonormal basis as $(\vec{\mathbf{e}}_n, \vec{\mathbf{e}}_s, \vec{\mathbf{e}}_f)$, where $\vec{\mathbf{e}}_f$ is aligned with the local fiber (Figure 3.2).

We were interested in computing the mechanical state of the tissue at end-systole (ES). The tissue deformation in the systolic phase results from a combination of active and passive mechanical properties. We modelled this interaction using a so-called active stress approach, where the total tissue stress is decomposed into an active ($\sigma_{\mathbf{active}}$) and a passive ($\sigma_{\mathbf{passive}}$) part.

$$\sigma_{\mathbf{total}} = \sigma_{\mathbf{passive}} + \sigma_{\mathbf{active}}, \tag{5.1}$$

Introducing $\mathbf{R}_f$ as the matrix of transformation from global to local coordinate system, $\mathbf{F}$ as the deformation gradient, and $J = det(\mathbf{F})$ ($J = 1$ for incompressible tissue), the active stress in global coordinates can be expressed as

$$\sigma_{\mathbf{active}} = J^{-1}\mathbf{F}{\mathbf{R}_f}^{-1}\begin{bmatrix} 0 & 0 & 0 \\ 0 & 0 & 0 \\ 0 & 0 & a_f \end{bmatrix}\mathbf{R}_f\mathbf{F}^T, \tag{5.2}$$

where a_f is the active tension developed by the contracting fibers.

Following our assumption of homogeneous contraction, the value of a_f is assumed constant in space, and is tuned to provide the best possible match with the measured strain data for each patient. The chosen maximum value for a_f was set to 135 kPa [Walker et al., 2005b, Dorri et al., 2006]. The passive component in (5.1) was modelled as hyperelastic, with stress derived from a strain energy function W ;

$$\sigma_{\mathbf{passive}} = J^{-1}\mathbf{F}(\partial W/\partial \mathbf{E})\mathbf{F}^T. \tag{5.3}$$

Here $\mathbf{E}$ is the Green-Lagrange deformation tensor.

In the literature, different strain energy functions have been proposed for the cardiac tissue as in [Holzapfel and Ogden, 2009], [Guccione et al., 1995] and [Usyk et al., 2000]. To reduce the complexity and number of parameters in the model, and based on the assumption that at ES the tissue stress is dominated by the active component, we used a simple Mooney-Rivlin strain energy model, as previously used in [Marchesseau et al., 2013a]:

$$W = c_1(\bar{I}_1 - 3) + c_2(\bar{I}_2 - 3) + K(J-1)^2. \tag{5.4}$$

Here c_1, c_2 are material parameters (MPs), $\bar{I}_1$ and $\bar{I}_2$ are the invariants of Right Cauchy Green tensor and $K = 2/d_1$ is the bulk modulus.

We performed a reference FE simulation using MPs $c_1 = 0.0187$ MPa, $c_2 = 0.0198$ MPa, $d_1 = 0.1697$ MPa, and the contraction model outlined above. The boundary conditions were as follow ; a pressure of 11.24 kPa was applied to the endocardial surface [Dorri et al., 2006], the epicardial surface was unloaded, and the basal nodes were assigned to remain coplanar during deformation [Marchesseau et al., 2013a]. This reference FE simulation was compared with results reported in [Dorri et al., 2006] and showed good agreement in terms of LV EF (33.83%), wall thickness change (18.7%) and Von-Mises stresses which are in the range of $100-150$ kPa [Dorri et al., 2006,McCulloch et al., 1991,Guccione and McCulloch, 1993,Hunter et al., 1998].

We used these boundary conditions, MPs and contraction model for the *patient-specific* FE simulations of provided cohort with Abaqus® software solver.

Application on Synthetic Acute Ischemia

Two reference meshes have been used for application of our developed pipeline.

Ellipsoid Reference Mesh

An truncated ellipsoid mesh has been generated using Abaqus® software. The height of the mesh was 9 cm, and the wall thickness was 1 cm. The fiber directions were assigned as outlined above. We defined a small zone at the equatorial level of the septal wall, see Figure 5.2, as acutely ischemic, i.e. non-contractile. The active stress in this region was set to zero, while the rest of the reference FE model, $a_f = 160$ kPa was attributed. The same condition as explained in Section 5.1.2 in terms of boundary conditions, ES pressure, contraction model and MPs were used to perform this model. In order to relate the results to the echo images, we defined a mid-wall surface mesh that was slit into 17 segments as shown in Figure 5.3 [Cerqueira et al., 2002]. We will refer to this mesh as the midwall mesh throughout this paper. Regional deformations were calculated by as average strains in each segments (longitudinal, circumferential and area strain), similar to the output of the EchoPac strain analysis.

To provide a first test of the hypothesis underlying this paper, we performed a FE simulation with a homogeneous active stress (AAS), and tuned the active stress parameter to match the

strains of the synthetic reference model as closely as possible. The cost function was defined as the sum of squared differences (LSQ) between the AAS strains and the reference strains, and performed a simple minimization by gradually increasing a_f from 90 kPa to 180 kPa in 5 kPa steps. The smallest cost function obtained with this procedure was used as the closest match.

Healthy Reference Mesh

The healthy mesh obtained from US imaging in Section (5.1.2) was used in this study case. The abnormal zone for this mesh was defined on mid-cavity Anterior wall (Figure 5.2). The boundary condition, systolic blood pressure, contraction model, and the MPs were attributed as ellipsoid study case. The midwall regions were also generated in order to follow the regional deformations through systolic phase. Reorientation of the fiber directions in abnormal LV tissue is an open question [Holmes et al., 1997, Holmes et al., 2005, Walker et al., 2005a, Chen et al., 2003]. Therefore, we leave the fibers unchanged in the abnormal zone as defined for a healthy LV case in Section (5.1.2).

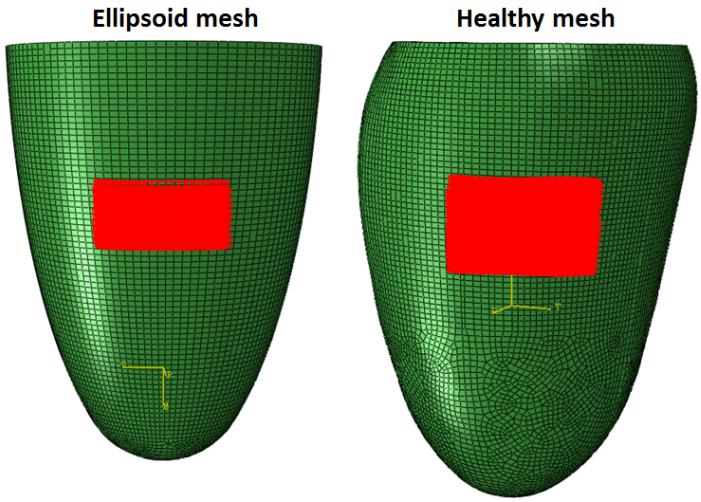

FIGURE 5.2 – The synthetic acute ischemia generated on ellipsoid and healthy LV obtained from US images. The elements highlighted in red show the considered zone for zero active stress while other elements in green are having a homogeneous active contraction value (160 kPa). Here, the systolic pressure was defined to 11.24 kPa.

Prediction of Abnormal Tissue Zone for LBBB Patient

A cohort of patients suffering from LBBB was available for studying our proposed method (refer to Figure 5.1) for abnormal zone detection (with chronic infarcts). It is a cardiac conduction abnormality which causes the LV to contract later than the right ventricle. We presented,

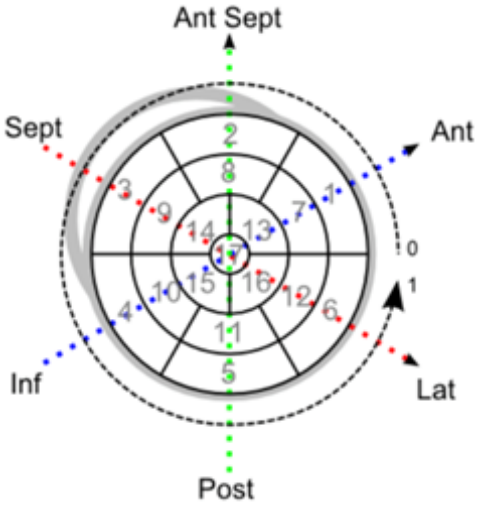

FIGURE 5.3 – The AHA convention which describes the LV model in 17 regions. The study cases were divided into 4 separate regions as basal, mid-cavity, apical, and apical cap. These regions were again split into several slices to build 17 regions. Copyrights reserved to GE Healthcare for this illustration of AHA regions.

previously, our FE method for a healthy LV contraction. In order to introduce the patient data to the FE software, we developed an in-house code to morph the reference FE mesh to the patient geometries. We demonstrated the steps for estimating a homogeneous active contraction value data of acute ischemia in Section 5.1.2.

Eight LBBB patients were recruited after informed consent at Rikshospitalet, Oslo, Norway. LV triangulated mesh geometries were acquired by a standard GE Healthcare echocardiography examination (Figure 4.4). The patient's LV cavity pressures were measured via an aortic catheter inside the ventricle's cavity (Figure 5.4). The 17 regional strains were measured using 4D strain tracking EchoPac® US system manufactured by GE Healthcare [Heimdal, 2011]. EchoPac® algorithm calculates the classical longitudinal, circumferential and area strains for each segment at the midwall between endocardial and epicardial surfaces from the segment's dimensions [Heimdal, 2011] (Figure 5.5).

From area strain (AS), we can calculate the radial strain (RS) as detailed in [Heimdal, 2011] from the incompressibility assumption (R=Volume/Area) of the cardiac tissue :

$$RS = -\frac{\frac{AS_{ES}-AS_{ED}}{AS_{ED}}}{\frac{AS_{ES}-AS_{ED}}{AS_{ED}+1}}. \tag{5.5}$$

We morphed the reference mesh (refer to Section 5.1.2) onto the geometry of each patient at ED time step for which US geometries were acquired. For this, endocardial and epicardial nodes

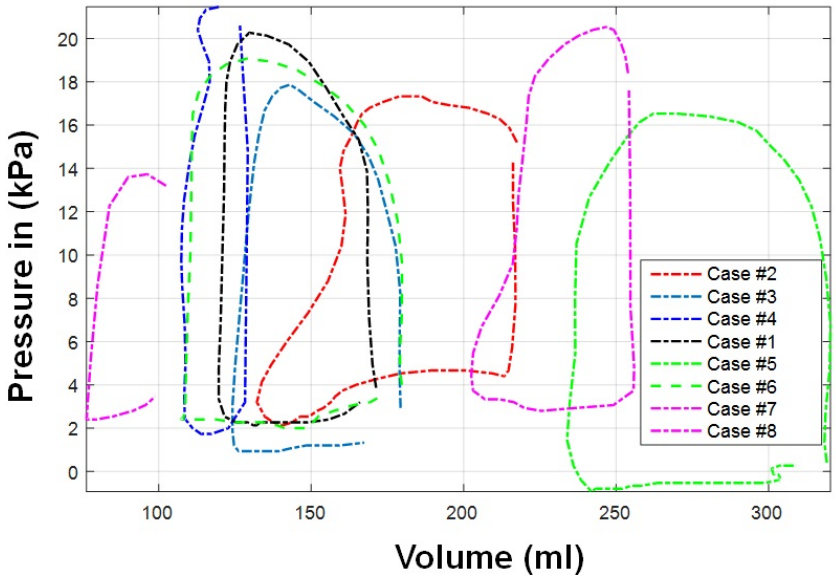

FIGURE 5.4 – The pressure-volume curves for LBBB patients obtained from US and aortic catheterization.

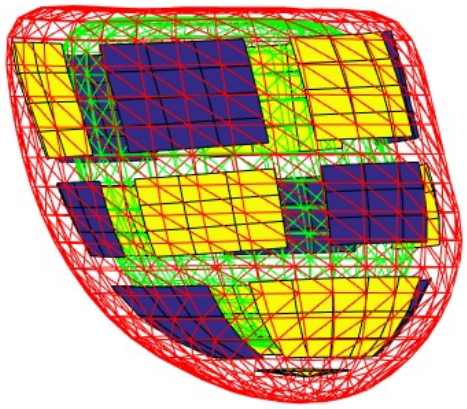

FIGURE 5.5 – The midwall mesh example for a patient obtained from EchoPac®. The red and green triangles are the epicardium and endocardium surfaces, respectively. The yellow and purple meshes are segment's midwall mesh. These meshes permit us to follow the LV deformation through a cardiac cycle.

of the deformable mesh were projected onto the patient triangulated surfaces from a defined LV *centerline* (Figure 4.3) with rigid and non-rigid transformation methods employing an in-house developed Matlab® code. In order to deform the reference bulk model with intermediate nodes, we used FE elastic rigid body deformation employing the displacement vectors obtained from boundaries projection trajectories (Figure 4.3). An in-house program coded in Matlab® found the closest nodes to the midwall mesh nodal positions obtained from EchoPac® system for each patient at ED. Therefore, we can follow the evolution of LV during its systolic phase

by calculating the deformations of each segment's mesh in area, radial circumferential and longitudinal strains.

For each patient after application of mesh morphing method, we employed the pressure values at ES from pressure-volume curves obtained during the medical intervention (Table 5.1). This cavity pressure was applied as the boundary condition on the endocardial surface as previously mentioned in Section 5.1.2. For the sake of simulation costs, for each patient we considered a set of values for a_f which starts at 60 kPa to 280 kPa with 5 kPa of intervals. Then, simply the LSQ takes the a_f which returns the minimum cost value.

TABLE 5.1 – The ES pressure values for LBBB patients measured through aortic valves.

Case	♯1	♯2	♯3	♯4	♯5	♯6	♯7	♯8
ES pressure (kPa)	16,8	14	14.27	15,47	12,67	16.53	14.53	8,666

5.1.3 Results

The focus of the following work is to describe and potentially detect the abnormal LV tissue by its application on different healthy and pathological study cases.

Study Cases

The closest match for ellipsoid mesh has achieved at 155 kPa for 0.0096 of cost value. The EF for acute ischemia was 41.32% and the closest match 43%. Figure 5.6 shows the result of the pipeline application which successfully detected the injured tissue zone at mid-cavity Septal wall.

Figure 5.7 shows the results of our developed pipeline on the synthetic acute ischemia on the LV body. The algorithm has successfully detected the abnormal zone at mid-Anterior wall. The AAS estimated for the closest midwall match deformation was 130 kPa for 0.0387 cost value. The EF was 35% for acute case and 20% for the closest match.

Application on LBBB Patients Data

We applied the mesh morphing method (explained in Section 5.1.2) to reconstruct the FE meshes of cohort data and the results are shown in Figure 4.5. The Table 5.2 shows the minimum cost value and the AAS for this minimum. In addition, the patient and the FE simulation cavity volumes which were measured from EchoPac® system and FE simulation software are shown at ED and ES in ml as well as the EF values.

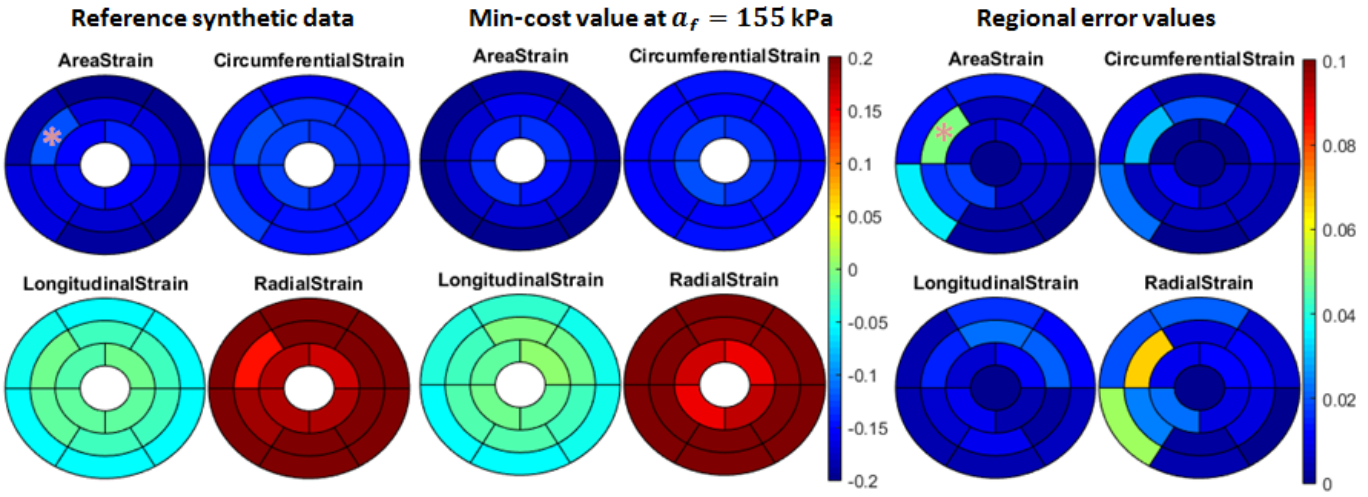

FIGURE 5.6 – The regional deformations resulted from FE simulation and synthetic acute ischemia for ellipsoid based on AHA standards. The ellipsoid reference synthetic acute ischemia, the closest match for regional deformation as well as the error are presented in this figure. The algorithm has successfully detected the abnormal zone at mid-cavity (stared) as well as its impact on the neighbouring tissue (Basal inferior).

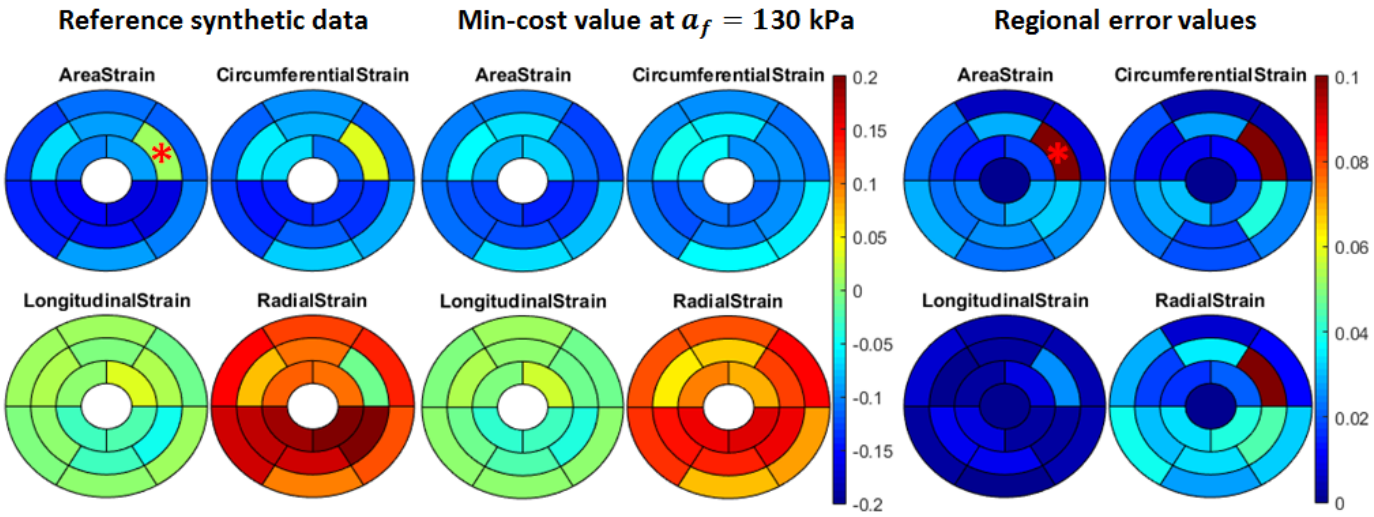

FIGURE 5.7 – The healthy FE simulations and the regional deformation results based on AHA standards are shown in this figure. The results are presented for the reference generated acute ischemia, the closest match and the regional errors. The stared region is the actual generated zone with zero active stress value (mid-Anterior wall).

The deformations obtained from US are in circumferential, longitudinal, and area strain of the midwall mesh. Then, the RS was obtained by incompressibility hypothesis of the LV segments as explained in [Heimdal, 2011]. The radial, circumferential and longitudinal strains are shown in Figure 5.8 for patients 4 and 7 where the pipeline detected the abnormal zone. The FE strain results has been subtracted from the patient's respective data and are shown in

TABLE 5.2 – The LBBB patients data measured (-P) and the FE results (-S). The ED volume (EDV), ES volume (ESV), LSQ cost value, optimized active stress (a_f) and EF are shown in this table. Patient 5 had no convergence success.

Case	*CostValue*	$a_f(kPa)$	$EDV-S(ml)$	$ESV-S(ml)$	$EF-S\%$	$EDV-P(ml)$	$ESV-P(ml)$	$EF-P\%$
♯1	0.5279	130	160.764	139.827	13.02	171.3	121.8	28.72
♯2	0.1960	135	196.815	140.20	28.76	215.9	159.4	26.16
♯3	0.1298	135	179.602	161.53	10	179.3	131.3	26.77
♯4	0.1686	95	120.082	124.195	Inflated	128.3	111.7	12.93
♯5	-	-	-	-	-	319.1	241.2	24,41
♯6	0.3358	180	168.118	132.808	21	179.7	111.2	38.11
♯7	0.7901	175	242.429	273.670	Inflated	255.7	219.4	14.19
♯8	0.1616	75	99.594	87.167	12.47	98.78	79.98	19

this figure as well.

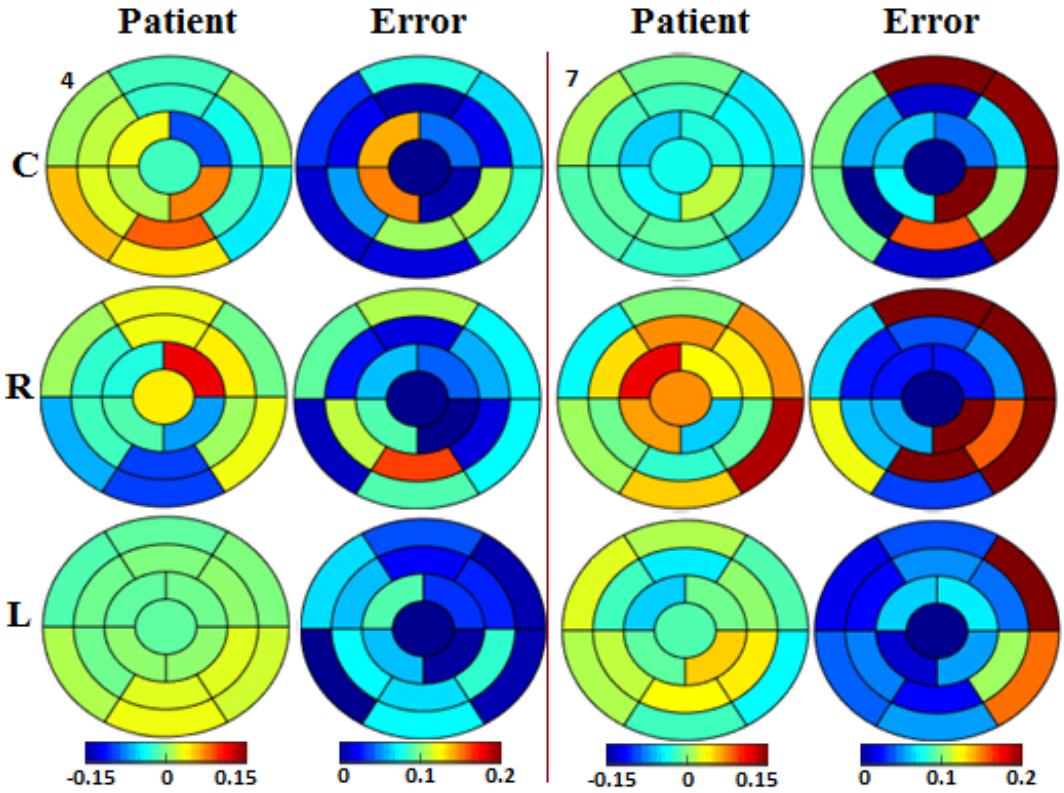

FIGURE 5.8 – The figure shows the LBBB patient's circumferential (C), radial (R) and longitudinal (L) strains at ES provided by EchoPac® US system. The deformation differences between patient's data and the FE results from LSQ application under AHA standards are also shown. In this figure, we can observe that the maximum/minimum value (left column) of the 4-Posterior, and 7-Lateral regions which are also the regions of maximum deviations observed in the FE results (right column), respectively.

Figure 5.9 is showing the transversal and longitudinal cuts of LBBB patient's geometries

superimposed by the FE simulation results for the optimal AAS. These cuts are tuned to show the maximum error zone (from 17 segments), obtained from LSQ application of regional deformation. The patient 5 had no convergence success and was not considered for further study.

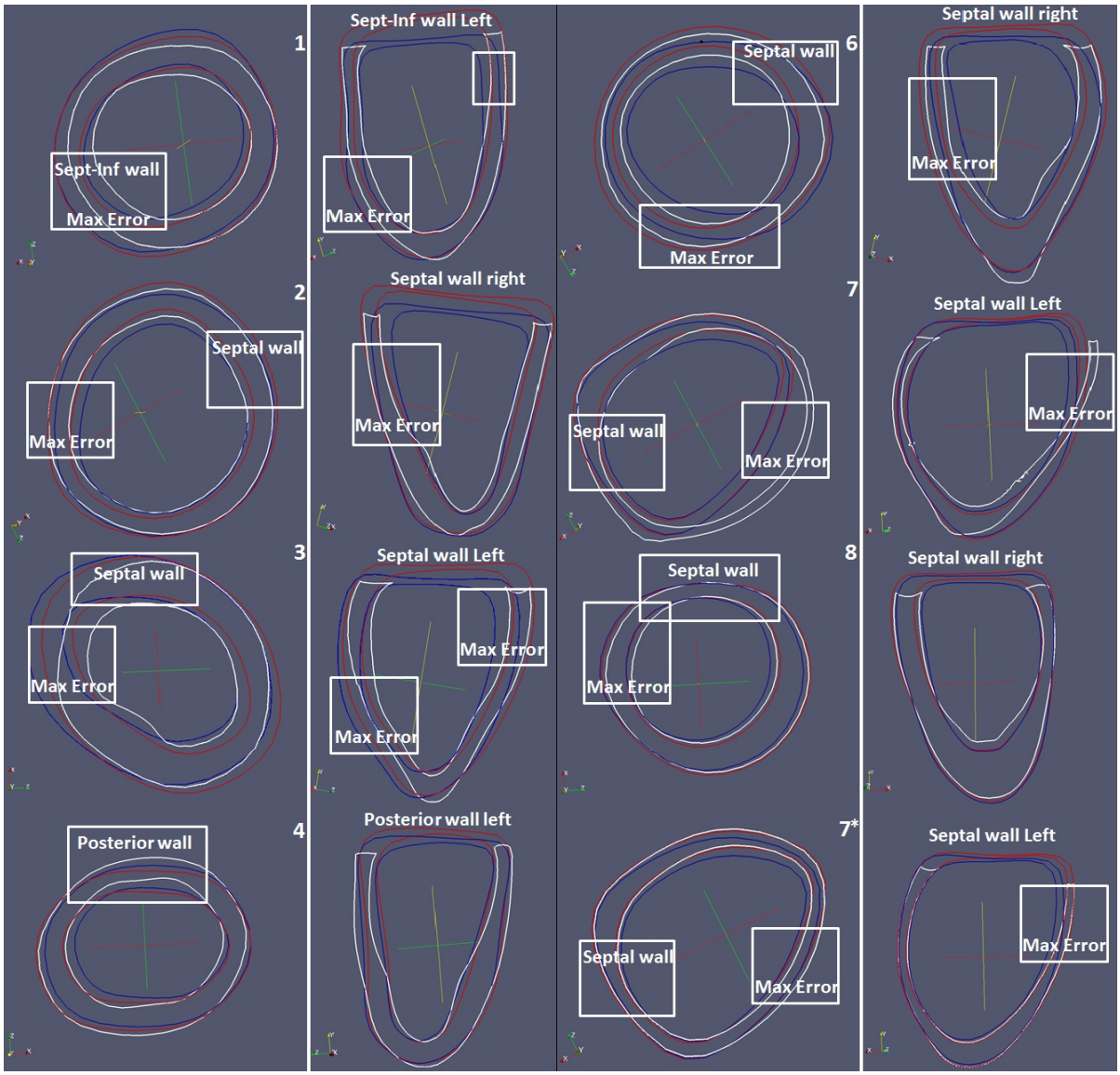

FIGURE 5.9 – The figure shows the transversal (first and third columns) and longitudinal (second and fourth columns) cuts of LBBB patient geometries (1-8) obtained from EchoPac® US system at ED (red lines) and ES (blue lines). The patient's data were superimposed with the FE simulation geometry for optimal AAS at ES (white lines). In this case, if the maximum error happened to be at Septal wall segment, the cut (longitudinal and transversal) passes through this segment in FE simulation and patient's geometry. The results for increasing MPs by 12 times are also shown here (7*). The patient 5 had no convergence success in this study.

5.1.4 Discussion

In this study, a new approach for detecting potentially infarcted areas was first validated on synthetic data and then applied to a cohort of 8 LBBB patients 15 days after their CRT. The results revealed zones of moderate heterogeneities which were often of smaller thickness but the heterogeneities were significantly less pronounced than that revealed for a synthetic case of acute ischemia. The method also revealed that the tissue tends to be stiffer in the lateral wall of LBBB patients. This is not very often that such a refined analysis is performed on the effect of CRT onto LBBB using FE analysis. It is very interesting to notice that the obtained results confirm what was already observed by other researchers using standard medical imaging. More specifically, [Veress et al., 2011] also showed the typical septum-related abnormal wall motion and impairment of wall thickening during systole which caused LV remodelling. Often, technologies such as MRI or PET were used to characterize the infarct heterogeneities as well as histological images [Walker et al., 2008, Arevalo et al., 2016, Pop et al., 2009]. We examined if such ability to detect abnormal tissue can stand for novel 4D strain EchoPac® system.

In order to detect the abnormal tissue, we identified an AAS for all FE meshes which was the closest match to the patient's midwall mesh deformation (Figure 5.1). This AAS represents a homogeneous contraction for each patient [McVeigh et al., 1998] and [Wyman et al., 1999]. In this condition it is expected that for a healthy and homogeneous contraction, the FE deformation responses be different in abnormal tissue than the rest of LV model. In addition, this value represents the average movement of remote (uninfarcted) and injured tissue.

Often, the patients suffering from abnormal contractility are evaluated by an optimized gradient of activation stress map. [Wenk et al., 2011] have developed an animal-specific FE model for such reconstruction by minimizing the regional deformation error between experimental data and FE model. In this study, a border zone was considered for early stage of tissue damaging process (due to calcium concentrations) which relates the injured to the remote tissue. They confirm that the infarct zone has no contractile action (zero active value).

Impact of MPs on the FE LV Deformation

[Wenk et al., 2011] have observed from tagging MRI images that the average infarct deformation tends to be zero (or positive) value while the border zone and remote strains are one and two order higher. In this study we have noticed the same issue. In Table 5.2, the AASs are mentioned for optimal cost values. These identified values are strongly coupled to the wall thickness, the blood pressure and the cavity volume. The FE results are based on the midwall

strain deformation which is not representative data for the complete wall motion and might be affected by artefacts. Some meshes are inflated such as in cases 4 and 7 in Table 5.2, even if, these cases are the most successful results of the abnormal tissue detection. The reason for this inflation might be the compliance MPs for the studied case. To study this hypothesis, we increased the elastic parameters (c_1 and c_2) by factors $[2, 4, 6, 8, 10, 12]$ to analyse the behaviour of the patient FE simulation to this increase in tissue rigidity.

For this test, patient 7 has been selected that the Posterior and neighbouring walls were deformed dramatically in FE simulation while this wall has not been moved during ED to ES movement. The cost value for this test from 0.7901 with 175 kPa of AAS was reduced to $[0.1893, 0.0775, 0.0626, 0.0592, 0.0591, 0.0564]$, respectively, and it is shown in Figure 5.9 for factor 12 (c_1 and c_2) in 7*. [Novak et al., 1994] showed that the aneurysmal wall is stiffer than the remote tissue as well. In this test, we observed that the results (7*) were improved by increasing the rigidity of the tissue MPs. It has been previously investigated, with mathematical model and experimental tests, that the infarct tissue stiffen (despite dilated infarctions) [Kelley et al., 1999]. However, the infarct tissue properties are still under investigation for various accompanying pathologies such as LBBB.

The Figure 5.9 shows several successful zone detection wherein the maximum error happens to be at the abnormal region. In case 1, the maximum deformation was observed at the Inf-Sept-AntSept regions where this neighbourhood wall slightly inflates (blue lines at Max-error in longitudinal cut) and the method detected this region successfully. However, in case 6, the inhomogeneous strain was observed at the Septal wall wherein the method detected the posterior wall as the maximum error. These results show that the strain data in some cases can be difficult to be judged on the detected zone and is subjective to the visual detection of the patient's strain and geometry data. However, a FE simulation of pathology cases permit us to narrow down the potential defeated zone to less regions, especially, in case 4 and 7 in Figure 5.8 and to study the mechanical state of the cardiac tissue by analysing the wall stress as a post-processing step.

The results showed a good agreement with several patient deformations in RS which has been showed to be a good indicator, than circumferential or longitudinal due to the homogeneous distribution of these deformation values, for discrimination of possible heterogeneities in the active stress and abnormal tissue movement. We observed that the identified active stress is highly coupled to the patient geometry and wall thickness [Götte et al., 2001]. This is the advantage of the new generations of US system in extracting the RS from measuring the surface

of a given segment that is not possible for modalities such as tagging MRI [Denney et al., 2003].

Remodelling in LBBB Patients and its Impact on the Pipeline Results

The LBBB, itself, causes tissue remodelling due to the redistribution of LV workload in the long run, especially, in circumferential shortening, cardiac mass, septal hypoperfusion and myocardial blood flow [Kasai et al., 2004, Mahrholdt et al., 2005, Sugihara et al., 1997, Vernooy et al., 2005]. However, this pathology is, often, the result of other cardiac diseases. Statistically, 40% of the patients with cardiomyopathy (CMP), weakening of the heart muscle and congestive heart failure (CHF) have unsynchronized ventricular contraction. The CRT procedure helps in reverse remodelling and hospitalization-free survival rate of 70% to 90% in these patients [Prinzen et al., 1995, Breithardt et al., 2003, Ypenburg et al., 2009]. This abnormal redistribution has been also noticed in our cohort.

The observed regional differences were not the case for the ellipsoid and healthy mesh illustrated previously, where the wall thickness is nearly homogeneous. The change in MPs or wall thickness in LBBB patients with previous infarct history, reduced the efficiency of this method for some patients with high heterogeneity in the wall deformation due to the tissue remodelling. In the Figure 5.9 and the Table 5.2, we can observe that the FE simulation response in the maximum differences is mostly over/under estimates the tissue deformation which is at the high heterogeneities in wall thickness.

Patient 5 had no convergence success due to the large cavity volume ($319ml$ at ED) and the thin wall thickness (remodelled tissue). The large cavity volume is related to an aneurysmal bulging which made contraction simulation fail to reach a solution.

Several studies showed that the LBBB patients respond poorly (30%) to CRT procedure and cases with developed scared tissue tend to not respond at all [Auricchio et al., 2002, Abraham et al., 2002, Kerckhoffs et al., 2009]. This study is a tool for patient cases which are not yet subjected to this remodelling phase and are in early stages of LBBB pathology wherein it is difficult to observe deformation's anomaly using medical imaging techniques. Knowing the infarct region, by detection methods, in patient's LV is a helpful information in planning for CRT procedure [Constantino et al., 2012].

Limitations and Future Work

One major limitation in this study is the choice of material and contraction models to simplify the complexity and computational costs. In addition, we defined a vector for a_f value

which is also a brutal simplification for AAS identification procedure. However, with all this simplifications the time of each simulation on a 12-core system was 72 hours in average. One issue might be the small elements generated by developed mesh morphing procedure that reduced the time steps in FE solver. One natural step can be improving the material model to anisotropic from the state-of-the-art [Holzapfel and Ogden, 2009]. The mesh morphing method should also be improved to reduce the computational costs in the further work.

Another limitation is the lack of patient's history information. In this study, the patients are known to have LBBB pathology with infarct history but there is no information about other accompanying pathology which may cause the uncoordinated ventricles. The large cavity volume, low EF and low wall thickness can be related to various pathologies such as dilated CMP, and CHF due to the ischemic ventricle. So in this work, it is not possible to categorize the patients with their pathologies (such as patient 5) and the identified AAS. We considered a stress-free configuration to simulate the systolic phase for our cohort so this issue should be further addressed.

One other improvement is to reconstruct the patient fiber orientations from MRI imaging modalities such as diffusion tensor and tagging MRI to improve the deformation trajectories during contraction [Wu et al., 2006]. The possibility to compare this study results with cardiac MRI for identifying the abnormal tissue is also an interesting future step.

5.1.5 Conclusion

In this study, a new approach for detecting potentially infarcted areas was introduced, validated and then applied onto a cohort of 8 LBBB patients 15 days after their cardiac resynchronisation therapy. The results revealed zones of moderate heterogeneities which were often of regions of thinner wall. However the heterogeneities were significantly less pronounced that revealed for a synthetic case of acute ischemia, which we interpreted as an effect of remodelling induced by the therapy. The method also revealed that the tissue tends to be stiffer in the lateral wall of LBBB patients even 15 days after their therapy. This study is promising which interested in these effects of cardiac resynchronisation therapy onto LBBB and its quantification using FE simulations. Finally, this illustrates the importance of patient-specific FE simulations in the domain of cardiac biomechanics. In the future, it would be interesting to compare the reconstructions made with our methodology on LBBB patients at different stages of remodelling after the cardiac resynchronization treatment. In addition, further work is required to transfer the promising synthetic results to real acute ischemic patient cases.

Conclusion générale

Préambule

Cette thèse, effectuée dans le cadre d'une collaboration entre Simula et le CIS de Mines Saint-Étienne, avait pour objectifs de contribuer au développement d'outils de médecine prédictive pour affiner le diagnostic des pathologies cardiaques par reconstruction précise des cartes de contrainte dans le tissu du VG.

Dans un premier temps, nous avons étudié, dans un VG sain en phases actives et passives du cycle cardiaque, l'impact des modèles de comportement et de leurs paramètres sur le champ de contrainte. Nous avons montré que pour un modèle hyperélastique isotrope, la carte de contraintes Cauchy dans chaque phase dépend très modérément des paramètres matériaux. Les contraintes de Cauchy dans le muscle contracté restent peu impactées par les paramètres matériaux en raison de la faiblesse des contraintes passives au regard des contraintes actives. Dans le cas de modèle hyperélastique anisotrope (modèle de Guccione), l'impact des paramètres hyperélastique est maximal à l'état relâché. C'est surtout le module élastique de la matrice qui a le plus d'influence sur le résultat, alors que la sensibilité aux paramètres des exponentielles, pilotant le comportement des fibres, a moins d'impact.

Dans un second temps, nous avons utilisé un modèle EFs du VG pour retrouver les zones de dysfonction dans des tissus pathologiques. La méthode de détection des zones potentiellement infarctées a été validée avec succès sur des données synthétiques simulant une ischémie aiguë. Pour la cohorte, nous avons d'abord développé une approche permettant de générer rapidement et directement des maillages volumiques à partir des données US de GE Healthcare chez les patients BBG. Ensuite, nous avons réussi à reproduire la déformation régionale des géométries de 8 patients en recalant à partir de données US la contrainte active de contraction des fibres cardiaques et le modèle élastique d'un modèle hyperélastique Mooney-Rivlin. Cela montre que même un modèle du matériau isotrope peut être représentatif du tissu myocarde sous certaines conditions. Nous avons également observé que ce recalage d'un modèle moyen permettait en-

suite de détecter les zones ayant un écart important à la moyenne pour les données synthétiques simulant une ischémie aiguë. Cet écart a été constaté localement pour les déformations radiales, qui constituent donc un bon indicateur pour une contraction malsaine. La méthode a été moins réussie pour les cas de cohorte BBG, par conséquent, un travail supplémentaire est nécessaire pour transférer ces résultats prometteurs synthétiques de ischémie aiguë à des cas de patients réels.

Finalement, la modélisation par EFs du myocarde associée aux technologies d'imagerie telles que l'échographie GE Healthcare s'est montrée très importante pour la détection non-invasive des mouvements anormaux provoqués par une pathologie cardiaque en phase de diagnostic.

Plusieurs pistes de poursuite de ce travail sont envisagées afin d'en améliorer les débouchés :

1. Améliorer le modèle de comportement qui a été utilisé pour l'identification de la contrainte moyenne active chez les patients BBG. Un modèle isotrope a été utilisé. Il a déjà été utilisé par d'autres auteurs de la littérature, mais il sera utile de le remplacer par un modèle matériau anisotrope afin de le rendre plus précis. Néanmoins, nous avons déjà montré que ce modèle simple est efficace pour décrire correctement la contrainte moyenne active. Des travaux supplémentaires sont nécessaires pour transférer les résultats synthétiques prometteurs à des cas réels de patients. Le travail pour passer à un modèle isotrope transverse a été initié dans cette thèse et est synthétisé en Annexe A. A l'avenir, ce modèle pourra être utilisé pour des simulations patients-spécifiques dans des cas pathologiques. Il pourra encore être sophistiqué d'avantage en le rendant complètement orthotrope. Néanmoins, le manque d'études concernant l'identification des paramètres d'un modèle complètement orthotrope constitue un frein à ce développement.

2. Une application naturelle de l'algorithme de morphing serait de reconstruire le mouvement du VG à partir des données US en temps réel pour analyser les dysfonctions en cours d'examen.

3. Une amélioration qui reste à implémenter concerne aussi l'orientation des fibres du tissu dans le modèle. Pour l'instant nous avons paramétré des orientations génériques sans prendre en compte d'éventuelles hétérogénéités.

4. Enfin, le découplage entre les contraintes actives et passives est une simplification qui peut constituer une limite. Un modèle de contraction active plus sophistiqué [Marchesseau et al., 2013a, Niederer and Smith, 2009, Vendelin et al., 2002, Hunter et al., 1998, Nash and Hunter, 2000, Sundnes et al., 2007] pourra être développé pour valider la pertinence des méthodes que nous avons mises en œuvre pour la détection non-invasive des mouvements

anormaux provoqués par une pathologie cardiaque en phase de diagnostic.

Conclusions and Perspectives

The collaboration between Simula Research Laboratory and Mines Saint Etienne for this thesis, has been established to develop predictive medical tools available for diagnosis of cardiac pathologies by reconstructing the stress map of left ventricular wall tissue.

We, first, studied the impact of different constitutive models and their parameters on the stress field reconstructed for a healthy LV in active and passive instances of cardiac cycle. We have shown that for an isotropic hyperelastic model, the Cauchy stress map in each phase is moderately dependant on the MPs. The Cauchy stress in the contracted muscle are marginally affected by the MPs because of the low impact of passive to active stresses. In the case of anisotropic material model (Guccione), the impact of MPs is maximum at the relaxation phase. This is, especially, the influence of elastic modulus of the matrix on the stress results, while the sensitivity to the parameters of exponential power, which conduct the fiber behaviour, has less impact.

Then, we used a FE model of LV to detect the abnormal zones of the ventricular tissue in a pathological cohort. The detection method of potentially infarcted areas has been validated successfully on synthetic data simulating acute ischemia. For cohort data we, first, developed an approach to generate fast and direct FE bulk meshes from US data provided by GE Healthcare. Then, we successfully reproduced the regional deformation of 8 patients geometries obtained from US data by tuning, a homogeneous active contraction for cardiac fibers and the elastic properties of a hyperelastic model (Mooney-Rivlin). This shows that even a model of isotropic material may be representative of myocardial tissue under certain conditions. We also observed that the homogeneous active contraction assumption result in detection of areas with a significant deviation from the neighbouring tissue. This difference was found locally more significant for radial deformations, which are therefore a good indicator of an unhealthy contraction. The method has been less successful for LBBB cohort cases, therefore, further work is required to transfer this promising synthetic results of acute ischemia to real patient cases.

Finally, the FE modelling of myocardial tissue associated with medical imaging techniques, such as GE Healthcare US, are very important for non-invasive detection of the ventricular abnormal movements caused by cardiac pathologies under diagnostic procedure.

Several future works are envisaged to continue this PhD work which can improve our results :

1. Improve the material model which has been used in the homogeneous active contraction

identification for LBBB patients. An isotropic material model has been used for this purpose. This model has been used, previously, by other authors in the literature, but this should be improved to anisotropic material model to provide a precise FE simulation. However, we have already shown that this simple material model is adequate enough to describe myocardial tissue and to model active contraction. The improvements to this model to a transversely isotropic material has been initiated and described in Annexe A. As a future work, this model can be used to perform patient-specific simulations for various ventricular pathologies. It may even be sophisticated to advantage by making it completely orthotrope. Nevertheless, the lack of studies on the MPs identification of such complete orthotropic model limit this development.

2. A natural application of our mesh morphing method will be to reconstruct the ventricular movements from US data in real time to analyse the dysfunctions under clinical examinations.

3. One improvement that remains undone is to implement the orientation of cardiac fibers in the FE model. For the moment, we consider synthetic fiber orientations in the ventricular wall without taking into account the possible inhomogeneities.

4. Finally, the coupling of the active and passive is a brutal simplification and a major barrier. As a future work, a sophisticated model of active contraction based on the available literature [Marchesseau et al., 2013a, Niederer and Smith, 2009, Vendelin et al., 2002, Hunter et al., 1998, Nash and Hunter, 2000, Sundnes et al., 2007], should be developed to validate the relevance of the methods we have implemented for non-invasive detection of abnormal movements caused by cardiac pathology under diagnostic phase.

We would like to thank Simula Research Laboratory for financing this PhD and GE Healthcare to provide the US data that has been used in this thesis.

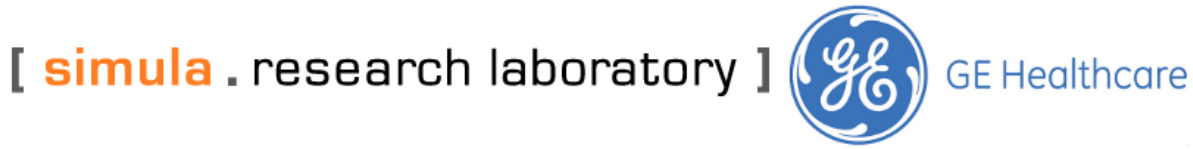

Bibliographie

[AbaqusGeneralizedFungform, 2016] AbaqusGeneralizedFungform (2016). Abaqus documentation. `http://abaqus.software.polimi.it/v6.14/books/usb/default.htm?startat=pt05ch22s05abm09.html#usb-mat-canisohyperelastic-fung`. [Online ; accessed 12-September-2016].

[Abraham et al., 2002] Abraham, W. T., Fisher, W. G., Smith, A. L., Delurgio, D. B., Leon, A. R., Loh, E., Kocovic, D. Z., Packer, M., Clavell, A. L., Hayes, D. L., et al. (2002). Cardiac resynchronization in chronic heart failure. *New England Journal of Medicine*, 346(24) :1845–1853.

[Amberg et al., 2007] Amberg, B., Romdhani, S., and Vetter, T. (2007). Optimal step nonrigid icp algorithms for surface registration. In *2007 IEEE Conference on Computer Vision and Pattern Recognition*, pages 1–8. IEEE.

[Antiga, 2002] Antiga, L. (2002). Patient-specific modeling of geometry and blood flow in large arteries. *Politecnico di Milano*.

[Arevalo et al., 2016] Arevalo, H. J., Vadakkumpadan, F., Guallar, E., Jebb, A., Malamas, P., Wu, K. C., and Trayanova, N. A. (2016). Arrhythmia risk stratification of patients after myocardial infarction using personalized heart models. *Nature communications*, 7.

[Ateshian and Costa, 2009] Ateshian, G. A. and Costa, K. D. (2009). A frame-invariant formulation of fung elasticity. *Journal of biomechanics*, 42(6) :781–785.

[Ateshian et al., 2007] Ateshian, G. A., Ellis, B. J., and Weiss, J. A. (2007). Equivalence between short-time biphasic and incompressible elastic material responses. *Journal of biomechanical engineering*, 129(3) :405–412.

[Aubry et al., 2011] Aubry, M., Schlickewei, U., and Cremers, D. (2011). The wave kernel signature : A quantum mechanical approach to shape analysis. In *Computer Vision Workshops (ICCV Workshops), 2011 IEEE International Conference on*, pages 1626–1633. IEEE.

[Audette et al., 2000] Audette, M. A., Ferrie, F. P., and Peters, T. M. (2000). An algorithmic overview of surface registration techniques for medical imaging. *Medical image analysis*, 4(3) :201–217.

[Augenstein et al., 2005] Augenstein, K. F., Cowan, B. R., LeGrice, I. J., Nielsen, P. M., and Young, A. A. (2005). Method and apparatus for soft tissue material parameter estimation using tissue tagged magnetic resonance imaging. *Journal of biomechanical engineering*, 127(1) :148–157.

[Auricchio et al., 2002] Auricchio, A., Stellbrink, C., Sack, S., Block, M., ürgen Vogt, J., Bakker, P., Huth, C., Schöndube, F., Wolfhard, U., Böcker, D., et al. (2002). Long-term clinical effect of hemodynamically optimized cardiac resynchronization therapy in patients with heart failure and ventricular conduction delay. *Journal of the American College of Cardiology*, 39(12) :2026–2033.

[Axel and Dougherty, 1989] Axel, L. and Dougherty, L. (1989). Mr imaging of motion with spatial modulation of magnetization. *Radiology*, 171(3) :841–845.

[Bagger et al., 2012] Bagger, T., Sloth, E., and Jakobsen, C.-J. (2012). Left ventricular longitudinal function assessed by speckle tracking ultrasound from a single apical imaging plane. *Critical care research and practice*, 2012.

[Bajcsy et al., 1983] Bajcsy, R., Lieberson, R., and Reivich, M. (1983). A computerized system for the elastic matching of deformed radiographic images to idealized atlas images. *Journal of computer assisted tomography*, 7(4) :618–625.

[Barber and Hose, 2005] Barber, D. and Hose, D. (2005). Automatic segmentation of medical images using image registration : diagnostic and simulation applications. *Journal of medical engineering & technology*, 29(2) :53–63.

[Barber et al., 2007] Barber, D. C., Oubel, E., Frangi, A. F., and Hose, D. (2007). Efficient computational fluid dynamics mesh generation by image registration. *Medical image analysis*, 11(6) :648–662.

[Beatty, 1987] Beatty, M. F. (1987). Topics in finite elasticity : hyperelasticity of rubber, elastomers, and biological tissues with examples. *Applied Mechanics Reviews*, 40(12) :1699–1734.

[Becker et al., 1996] Becker, R. C., Gore, J. M., Lambrew, C., Weaver, W. D., Rubison, R. M., French, W. J., Tiefenbrunn, A. J., Bowlby, L. J., and Rogers, W. J. (1996). A composite view of cardiac rupture in the united states national registry of myocardial infarction. *Journal of the American College of Cardiology*, 27(6) :1321–1326.

[Benzley et al., 1995] Benzley, S. E., Perry, E., Merkley, K., Clark, B., and Sjaardama, G. (1995). A comparison of all hexagonal and all tetrahedral finite element meshes for elastic and elasto-plastic analysis. In *Proceedings, 4th International Meshing Roundtable*, volume 17, pages 179–191. Sandia National Laboratories Albuquerque, NM.

[Bettendorff-Bakman et al., 2006] Bettendorff-Bakman, D.-E., Schmid, P., Lunkenheimer, P., and Niederer, P. (2006). A finite element study relating to the rapid filling phase of the human ventricles. *Journal of theoretical biology*, 238(2) :303–316.

[Betts et al., 2013] Betts, J. G. et al. (2013). et al. anatomy & physiology. *Open Stax College*.

[Bistoquet et al., 2007] Bistoquet, A., Oshinski, J., and Skrinjar, O. (2007). Left ventricular deformation recovery from cine mri using an incompressible model. *IEEE Transactions on Medical Imaging*, 26(9) :1136–1153.

[Blacker, 2000] Blacker, T. (2000). Meeting the challenge for automated conformal hexahedral meshing. In *9th international meshing roundtable*, pages 11–20. Citeseer.

[Blessberger and Binder, 2010] Blessberger, H. and Binder, T. (2010). Two dimensional speckle tracking echocardiography : basic principles. *Heart*, 96(9) :716–722.

[Bogen et al., 1980] Bogen, D. K., Rabinowitz, S. A., Needleman, A., McMahon, T. A., and Abelmann, W. H. (1980). An analysis of the mechanical disadvantage of myocardial infarction in the canine left ventricle. *Circulation Research*, 47(5) :728–741.

[Bonet and Wood, 1997] Bonet, J. and Wood, R. D. (1997). *Nonlinear continuum mechanics for finite element analysis*. Cambridge university press.

[Bovendeerd et al., 1994] Bovendeerd, P., Huyghe, J., Arts, T., Van Campen, D., and Reneman, R. (1994). Influence of endocardial-epicardial crossover of muscle fibers on left ventricular wall mechanics. *Journal of biomechanics*, 27(7) :941–951.

[Bovendeerd, 1990] Bovendeerd, P. H. M. (1990). The mechanics of the normal and ischemic left ventricle during the cardiac cycle : a numerical and experimental analysis.

[Boyett et al., 2005] Boyett, M. R., Li, J., Inada, S., Dobrzynski, H., Schneider, J. E., Holden, A. V., and Zhang, H. (2005). Imaging the heart : computer 3-dimensional anatomic models of the heart. *Journal of electrocardiology*, 38(4) :113–120.

[Breithardt et al., 2003] Breithardt, O.-A., Stellbrink, C., Herbots, L., Claus, P., Sinha, A. M., Bijnens, B., Hanrath, P., and Sutherland, G. R. (2003). Cardiac resynchronization therapy can reverse abnormal myocardial strain distribution in patients with heart failure and left bundle branch block. *Journal of the American College of Cardiology*, 42(3) :486–494.

[Breitkreutz et al., 2007] Breitkreutz, R., Walcher, F., and Seeger, F. H. (2007). Focused echocardiographic evaluation in resuscitation management : Concept of an advanced life support–conformed algorithm. *Critical care medicine*, 35(5) :S150–S161.

[Broit, 1981] Broit, C. (1981). Optimal registration of deformed images.

[Bronstein and Kokkinos, 2010] Bronstein, M. M. and Kokkinos, I. (2010). Scale-invariant heat kernel signatures for non-rigid shape recognition. In *Computer Vision and Pattern Recognition (CVPR), 2010 IEEE Conference on*, pages 1704–1711. IEEE.

[Buchalter et al., 1990] Buchalter, M. B., Weiss, J. L., Rogers, W. J., Zerhouni, E. A., Weisfeldt, M. L., Beyar, R., and Shapiro, E. P. (1990). Noninvasive quantification of left ventricular rotational deformation in normal humans using magnetic resonance imaging myocardial tagging. *Circulation*, 81(4) :1236–1244.

[Bucki et al., 2010] Bucki, M., Lobos, C., and Payan, Y. (2010). A fast and robust patient specific finite element mesh registration technique : application to 60 clinical cases. *Medical image analysis*, 14(3) :303–317.

[Burton et al., 2006] Burton, R. A., Plank, G., Schneider, J. E., Grau, V., Ahammer, H., Keeling, S. L., Lee, J., Smith, N. P., Gavaghan, D., Trayanova, N., et al. (2006). Three-dimensional models of individual cardiac histoanatomy : Tools and challenges. *Annals of the New York Academy of Sciences*, 1080(1) :301–319.

[CCI-Impact, 2016] CCI-Impact (2016). Oslo university hospital, acute feedback on left ventricular lead implantation location for cardiac resynchronization therapy (cci impact). *https ://clinicaltrials.gov*.

[Cerqueira et al., 2002] Cerqueira, M. D., Weissman, N. J., Dilsizian, V., Jacobs, A. K., Kaul, S., Laskey, W. K., Pennell, D. J., Rumberger, J. A., Ryan, T., Verani, M. S., et al. (2002). Standardized myocardial segmentation and nomenclature for tomographic imaging of the heart a statement for healthcare professionals from the cardiac imaging committee of the council on clinical cardiology of the american heart association. *Circulation*, 105(4) :539–542.

[Chen et al., 2003] Chen, J., Song, S.-K., Liu, W., McLean, M., Allen, J. S., Tan, J., Wickline, S. A., and Yu, X. (2003). Remodeling of cardiac fiber structure after infarction in rats quantified with diffusion tensor mri. *American Journal of Physiology-Heart and Circulatory Physiology*, 285(3) :H946–H954.

[Ciarlet and Mardare, 2009] Ciarlet, P. G. and Mardare, C. (2009). The pure displacement problem in nonlinear three-dimensional elasticity : intrinsic formulation and existence theorems. *Comptes Rendus Mathematique*, 347(11) :677–683.

[Colletti et al., 2011] Colletti, P. M., Shinbane, J. S., and Shellock, F. G. (2011). Mr-conditional pacemakers : The radiologist's role in multidisciplinary management. *American Journal of Roentgenology*, 197(3) :W457–W459.

[Constantino et al., 2012] Constantino, J., Hu, Y., and Trayanova, N. A. (2012). A computational approach to understanding the cardiac electromechanical activation sequence in the normal and failing heart, with translation to the clinical practice of crt. *Progress in biophysics and molecular biology*, 110(2) :372–379.

[Corrado et al., 1997] Corrado, D., Basso, C., Thiene, G., McKenna, W. J., Davies, M. J., Fontaliran, F., Nava, A., Silvestri, F., Blomstrom-Lundqvist, C., Wlodarska, E. K., et al. (1997). Spectrum of clinicopathologic manifestations of arrhythmogenic right ventricular cardiomyopathy/dysplasia : a multicenter study. *Journal of the American College of Cardiology*, 30(6) :1512–1520.

[Costa et al., 2001] Costa, K. D., Holmes, J. W., and McCulloch, A. D. (2001). Modelling cardiac mechanical properties in three dimensions. *Philosophical Transactions of the Royal Society of London A : Mathematical, Physical and Engineering Sciences*, 359(1783) :1233–1250.

[Costa et al., 1996] Costa, K. D., Hunter, P. J., Rogers, J., Guccione, J. M., Waldman, L., and McCulloch, A. D. (1996). A three-dimensional finite element method for large elastic deformations of ventricular myocardium : Cylindrical and spherical polar coordinates. *Journal of biomechanical engineering*, 118(4) :452–463.

[Costa et al., 1997] Costa, K. D., May-Newman, K., Farr, D., O'Dell, W. G., McCulloch, A. D., and Omens, J. H. (1997). Three-dimensional residual strain in midanterior canine left ventricle. *American Journal of Physiology-Heart and Circulatory Physiology*, 273(4) :H1968–H1976.

[Couteau et al., 2000] Couteau, B., Payan, Y., and Lavallée, S. (2000). The mesh-matching algorithm : an automatic 3d mesh generator for finite element structures. *Journal of biomechanics*, 33(8) :1005–1009.

[Dandel and Hetzer, 2009] Dandel, M. and Hetzer, R. (2009). Echocardiographic strain and strain rate imaging clinical applications. *International journal of cardiology*, 132(1) :11–24.

[Dandel et al., 2009] Dandel, M., Lehmkuhl, H., Knosalla, C., Suramelashvili, N., and Hetzer, R. (2009). Strain and strain rate imaging by echocardiography-basic concepts and clinical applicability. *Current cardiology reviews*, 5(2) :133–148.

[Davatzikos, 1997] Davatzikos, C. (1997). Spatial transformation and registration of brain images using elastically deformable models. *Computer Vision and Image Understanding*, 66(2) :207–222.

[Davatzikos and Bryan, 1996] Davatzikos, C. and Bryan, N. (1996). Using a deformable surface model to obtain a shape representation of the cortex. *IEEE transactions on medical imaging*, 15(6) :785–795.

[Demer and Yin, 1983] Demer, L. L. and Yin, F. (1983). Passive biaxial mechanical properties of isolated canine myocardium. *The Journal of physiology*, 339 :615.

[Demiray, 1976] Demiray, H. (1976). Stresses in ventricular wall. *Journal of Applied Mechanics*, 43(2) :194–197.

[Denney et al., 2003] Denney, T. S., Gerber, B. L., and Yan, L. (2003). Unsupervised reconstruction of a three-dimensional left ventricular strain from parallel tagged cardiac images. *Magnetic resonance in medicine*, 49(4) :743–754.

[D'hooge et al., 2002] D'hooge, J., Konofagou, E., Jamal, F., Heimdal, A., Barrios, L., Bijnens, B., Thoen, J., Van de Werf, F., Sutherland, G., and Suetens, P. (2002). Two-dimensional ultrasonic strain rate measurement of the human heart in vivo. *IEEE transactions on ultrasonics, ferroelectrics, and frequency control*, 49(2) :281–286.

[Doenst et al., 2009] Doenst, T., Spiegel, K., Reik, M., et al. (2009). Fluid-dynamic modelling of the left ventricle-prototypical evaluation of the effect of ischemic remodelling and surgical ventricular reconstruction. *Annals of Thoracic Surgery*.

[Dokos et al., 2002] Dokos, S., Smaill, B. H., Young, A. A., and LeGrice, I. J. (2002). Shear properties of passive ventricular myocardium. *American Journal of Physiology-Heart and Circulatory Physiology*, 283(6) :H2650–H2659.

[Domenichini et al., 2005] Domenichini, F., Pedrizzetti, G., and Baccani, B. (2005). Three-dimensional filling flow into a model left ventricle. *Journal of Fluid Mechanics*, 539 :179–198.

[Dorri et al., 2006] Dorri, F., Niederer, P., and Lunkenheimer, P. (2006). A finite element model of the human left ventricular systole. *Computer methods in biomechanics and biomedical engineering*, 9(5) :319–341.

[Durrer et al., 1970] Durrer, D., Van Dam, R. T., Freud, G., Janse, M., Meijler, F., and Arzbaecher, R. (1970). Total excitation of the isolated human heart. *Circulation*, 41(6) :899–912.

[Ecabert et al., 2008] Ecabert, O., Peters, J., Schramm, H., Lorenz, C., von Berg, J., Walker, M. J., Vembar, M., Olszewski, M. E., Subramanyan, K., Lavi, G., et al. (2008). Automatic model-based segmentation of the heart in ct images. *IEEE transactions on medical imaging*, 27(9) :1189–1201.

[Fernandez et al., 2004] Fernandez, J., Mithraratne, P., Thrupp, S., Tawhai, M., and Hunter, P. (2004). Anatomically based geometric modelling of the musculo-skeletal system and other organs. *Biomechanics and modeling in mechanobiology*, 2(3) :139–155.

[Fernandez-Teran and Hurle, 1982] Fernandez-Teran, M. and Hurle, J. (1982). Myocardial fiber architecture of the human heart ventricles. *The Anatomical Record*, 204(2) :137–147.

[Fishbein et al., 1978] Fishbein, M. C., Maclean, D., and Maroko, P. R. (1978). The histopathologic evolution of myocardial infarction. *Chest*, 73(6) :843–849.

[Frangi et al., 2001] Frangi, A. F., Niessen, W. J., and Viergever, M. A. (2001). Three-dimensional modeling for functional analysis of cardiac images, a review. *IEEE transactions on medical imaging*, 20(1) :2–5.

[Frederiksen et al., 2010] Frederiksen, C. A., JUHL-OLSEN, P., Larsen, U., Nielsen, D., Eika, B., and Sloth, E. (2010). New pocket echocardiography device is interchangeable with high-end portable system when performed by experienced examiners. *Acta Anaesthesiologica Scandinavica*, 54(10) :1217–1223.

[Fung, 1967] Fung, Y. (1967). Elasticity of soft tissues in simple elongation. *American Journal of Physiology–Legacy Content*, 213(6) :1532–1544.

[Gee et al., 2010] Gee, M., Förster, C., and Wall, W. (2010). A computational strategy for prestressing patient-specific biomechanical problems under finite deformation. *International Journal for Numerical Methods in Biomedical Engineering*, 26(1) :52–72.

[Geyer et al., 2010] Geyer, H., Caracciolo, G., Abe, H., Wilansky, S., Carerj, S., Gentile, F., Nesser, H.-J., Khandheria, B., Narula, J., and Sengupta, P. P. (2010). Assessment of myocardial mechanics using speckle tracking echocardiography : fundamentals and clinical applications. *Journal of the American Society of Echocardiography*, 23(4) :351–369.

[Gibson et al., 2003] Gibson, A., Riley, J., Schweiger, M., Hebden, J., Arridge, S., and Delpy, D. (2003). A method for generating patient-specific finite element meshes for head modelling. *Physics in medicine and biology*, 48(4) :481.

[Go et al., 1998] Go, A. S., Barron, H. V., Rundle, A. C., Ornato, J. P., and Avins, A. L. (1998). Bundle-branch block and in-hospital mortality in acute myocardial infarction. *Annals of internal medicine*, 129(9) :690–697.

[Götte et al., 2006] Götte, M. J., Germans, T., Rüssel, I. K., Zwanenburg, J. J., Marcus, J. T., van Rossum, A. C., and van Veldhuisen, D. J. (2006). Myocardial strain and torsion quantified by cardiovascular magnetic resonance tissue tagging : studies in normal and impaired left ventricular function. *Journal of the American College of Cardiology*, 48(10) :2002–2011.

[Götte et al., 2001] Götte, M. J., van Rossum, A. C., Twisk, J. W., Kuijer, J. P., Marcus, J. T., and Visser, C. A. (2001). Quantification of regional contractile function after infarction : strain analysis superior to wall thickening analysis in discriminating infarct from remote myocardium. *Journal of the American College of Cardiology*, 37(3) :808–817.

[Graham Jr et al., 1968] Graham Jr, T. P., Covell, J. W., Sonnenblick, E. H., Ross Jr, J., and Braunwald, E. (1968). Control of myocardial oxygen consumption : relative influence of contractile state and tension development. *Journal of Clinical Investigation*, 47(2) :375.

[Grasso and Brener, 2014] Grasso, A. and Brener, S. (2014). Complications of acute myocardial infarction.

[Grogan et al., 1995] Grogan, M., Redfield, M. M., Bailey, K. R., Reeder, G. S., Gersh, B. J., Edwards, W. D., and Rodeheffer, R. J. (1995). Long-term outcome of patients with biopsy-proved myocarditis : comparison with idiopathic dilated cardiomyopathy. *Journal of the American College of Cardiology*, 26(1) :80–84.

[Guccione and McCulloch, 1993] Guccione, J. and McCulloch, A. (1993). Mechanics of active contraction in cardiac muscle : part i constitutive relations for fiber stress that describe deactivation. *Journal of biomechanical engineering*, 115(1) :72–81.

[Guccione et al., 1995] Guccione, J. M., Costa, K. D., and McCulloch, A. D. (1995). Finite element stress analysis of left ventricular mechanics in the beating dog heart. *Journal of biomechanics*, 28(10) :1167–1177.

[Guccione et al., 1991] Guccione, J. M., McCulloch, A. D., and Waldman, L. (1991). Passive material properties of intact ventricular myocardium determined from a cylindrical model. *Journal of biomechanical engineering*, 113(1) :42–55.

[Guyton and Hall, 2006] Guyton, A. and Hall, J. (2006). Heart muscle ; the heart as a pump and function of the heart valves. *Textbook of medical physiology*, 11 :103–15.

[Hamby et al., 1983] Hamby, R. I., Weissman, R. H., Prakash, M., and Hoffman, I. (1983). Left bundle branch block : a predictor of poor left ventricular function in coronary artery disease. *American heart journal*, 106(3) :471–477.

[Hansegård et al., 2009] Hansegård, J., Urheim, S., Lunde, K., Malm, S., and Rabben, S. I. (2009). Semi-automated quantification of left ventricular volumes and ejection fraction by real-time three-dimensional echocardiography. *Cardiovascular ultrasound*, 7(1) :1.

[Hartwig et al., 2009] Hartwig, V., Giovannetti, G., Vanello, N., Lombardi, M., Landini, L., and Simi, S. (2009). Biological effects and safety in magnetic resonance imaging : a review. *International journal of environmental research and public health*, 6(6) :1778–1798.

[Harvey and Leinwand, 2011] Harvey, P. A. and Leinwand, L. A. (2011). Cellular mechanisms of cardiomyopathy. *The Journal of cell biology*, 194(3) :355–365.

[Hassaballah et al., 2013] Hassaballah, A. I., Hassan, M. A., Mardi, A. N., and Hamdi, M. (2013). An inverse finite element method for determining the tissue compressibility of human left ventricular wall during the cardiac cycle. *PloS one*, 8(12) :e82703.

[Heimdal, 2011] Heimdal, A. (2011). 4d strain : advanced research application for quantitative echocardiography. *United Kingdom : GE Healthcare*.

[Heimdal et al., 1998] Heimdal, A., Støylen, A., Torp, H., and Skjærpe, T. (1998). Real-time strain rate imaging of the left ventricle by ultrasound. *Journal of the American Society of Echocardiography*, 11(11) :1013–1019.

[Hoffman and Spaan, 1990] Hoffman, J. and Spaan, J. (1990). Pressure-flow relations in coronary circulation. *Physiological Reviews*, 70(2) :331–390.

[Holden, 2008] Holden, M. (2008). A review of geometric transformations for nonrigid body registration. *IEEE transactions on medical imaging*, 27(1) :111–128.

[Holmes et al., 2005] Holmes, J. W., Borg, T. K., and Covell, J. W. (2005). Structure and mechanics of healing myocardial infarcts. *Annu. Rev. Biomed. Eng.*, 7 :223–253.

[Holmes et al., 1997] Holmes, J. W., Nunez, J. A., and Covell, J. W. (1997). Functional implications of myocardial scar structure. *American Journal of Physiology-Heart and Circulatory Physiology*, 272(5) :H2123–H2130.

[Holzapfel, 2000] Holzapfel, G. A. (2000). Nonlinear solid mechanics, vol. 24.

[Holzapfel, 2002] Holzapfel, G. A. (2002). Nonlinear solid mechanics : a continuum approach for engineering science. *Meccanica*, 37(4) :489–490.

[Holzapfel and Ogden, 2009] Holzapfel, G. A. and Ogden, R. W. (2009). Constitutive modelling of passive myocardium : a structurally based framework for material characterization. *Philosophical Transactions of the Royal Society of London A : Mathematical, Physical and Engineering Sciences*, 367(1902) :3445–3475.

[Hooks et al., 2007] Hooks, D. A., Trew, M. L., Caldwell, B. J., Sands, G. B., LeGrice, I. J., and Smaill, B. H. (2007). Laminar arrangement of ventricular myocytes influences electrical behavior of the heart. *Circulation Research*, 101(10) :e103–e112.

[Hort, 1960] Hort, W. (1960). Makroskopische und mikrometrische untersuchungen am myokard verschieden stark gefüllter linker kammern. *Virchows Archiv für pathologische Anatomie und Physiologie und für klinische Medizin*, 333(6) :523–564.

[HRS, 2014] HRS (2014). Heart rhythm society : Ejection fraction.

[Hsu et al., 1998] Hsu, E., Muzikant, A., Matulevicius, S., Penland, R., and Henriquez, C. (1998). Magnetic resonance myocardial fiber-orientation mapping with direct histological correlation. *American Journal of Physiology-Heart and Circulatory Physiology*, 274(5) :H1627–H1634.

[Huang et al., 2008] Huang, Q.-X., Adams, B., Wicke, M., and Guibas, L. J. (2008). Non-rigid registration under isometric deformations. In *Computer Graphics Forum*, volume 27, pages 1449–1457. Wiley Online Library.

[HUISMAN et al., 1980] HUISMAN, R. M., ELZINGA, G., WESTERHOF, N., and SIPKEMA, P. (1980). Measurement of left ventricular wall stress. *Cardiovascular research*, 14(3) :142–153.

[Humphrey, 2006] Humphrey, J. (2006). Towards a theory of vascular growth and remodeling. In *Mechanics of Biological Tissue*, pages 3–15. Springer.

[Humphrey et al., 1990] Humphrey, J., Strumpf, R., and Yin, F. (1990). Determination of a constitutive relation for passive myocardium : I. a new functional form. *Journal of biomechanical engineering*, 112(3) :333–339.

[Humphrey and Yin, 1987] Humphrey, J. and Yin, F. (1987). On constitutive relations and finite deformations of passive cardiac tissue : I. a pseudostrain-energy function. *Journal of biomechanical engineering*, 109(4) :298–304.

[Hunter et al., 1998] Hunter, P., McCulloch, A., and Ter Keurs, H. (1998). Modelling the mechanical properties of cardiac muscle. *Progress in biophysics and molecular biology*, 69(2) :289–331.

[Hunter et al., 1997] Hunter, P., Nash, M., and Sands, G. (1997). Computational electromechanics of the heart. *Computational biology of the heart*, 12 :347–407.

[Hunter et al., 1991] Hunter, P. J., Nielsen, P., Smaill, B. H., LeGrice, I. J., and Hunter, I. W. (1991). An anatomical heart model with applications to myocardial activation and ventricular mechanics. *Critical reviews in biomedical engineering*, 20(5-6) :403–426.

[Hunter et al., 2003] Hunter, P. J., Pullan, A. J., and Smaill, B. H. (2003). Modeling total heart function. *Annual review of biomedical engineering*, 5(1) :147–177.

[Huyghe et al., 1992] Huyghe, J. M., Arts, T., van Campen, D. H., and Reneman, R. S. (1992). Porous medium finite element model of the beating left ventricle. *American Journal of Physiology-Heart and Circulatory Physiology*, 262(4) :H1256–H1267.

[Ibrahim, 2011] Ibrahim, E.-S. H. (2011). Myocardial tagging by cardiovascular magnetic resonance : evolution of techniques–pulse sequences, analysis algorithms, and applications. *Journal of Cardiovascular Magnetic Resonance*, 13(1) :1.

[Janz and Grimm, 1972] Janz, R. F. and Grimm, A. F. (1972). Finite-element model for the mechanical behavior of the left ventricle prediction of deformation in the potassium-arrested rat heart. *Circulation research*, 30(2) :244–252.

[Jensen et al., 2004] Jensen, M., Sloth, E., Larsen, K. M., and Schmidt, M. B. (2004). Transthoracic echocardiography for cardiopulmonary monitoring in intensive care. *European journal of anaesthesiology*, 21(09) :700–707.

[Jiang et al., 2012] Jiang, Z., Pajic, M., Moarref, S., Alur, R., and Mangharam, R. (2012). Modeling and verification of a dual chamber implantable pacemaker. In *International Conference on Tools and Algorithms for the Construction and Analysis of Systems*, pages 188–203. Springer.

[Joldes et al., 2016] Joldes, G. R., Miller, K., Wittek, A., and Doyle, B. (2016). A simple, effective and clinically applicable method to compute abdominal aortic aneurysm wall stress. *Journal of the mechanical behavior of biomedical materials*, 58 :139–148.

[Judd and Levy, 1991] Judd, R. M. and Levy, B. I. (1991). Effects of barium-induced cardiac contraction on large-and small-vessel intramyocardial blood volume. *Circulation research*, 68(1) :217–225.

[Kaluzynski et al., 2001] Kaluzynski, K., Chen, X., Emelianov, S. Y., Skovoroda, A. R., and O'Donnell, M. (2001). Strain rate imaging using two-dimensional speckle tracking. *IEEE transactions on ultrasonics, ferroelectrics, and frequency control*, 48(4) :1111–1123.

[Kamisago et al., 2000] Kamisago, M., Sharma, S. D., DePalma, S. R., Solomon, S., Sharma, P., McDonough, B., Smoot, L., Mullen, M. P., Woolf, P. K., Wigle, E. D., et al. (2000). Mutations in sarcomere protein genes as a cause of dilated cardiomyopathy. *New England Journal of Medicine*, 343(23) :1688–1696.

[Karam et al., 2008] Karam, S., Raboisson, M.-J., Ducreux, C., Chalabreysse, L., Millat, G., Bozio, A., and Bouvagnet, P. (2008). A de novo mutation of the beta cardiac myosin heavy chain gene in an infantile restrictive cardiomyopathy. *Congenital heart disease*, 3(2) :138–143.

[Kasai et al., 2004] Kasai, T., DePuey, E. G., and Shah, A. A. (2004). Decreased septal wall thickening in patients with left bundle branch block. *Journal of nuclear cardiology*, 11(1) :32–37.

[Keldermann et al., 2010] Keldermann, R. H., Nash, M. P., Gelderblom, H., Wang, V. Y., and Panfilov, A. V. (2010). Electromechanical wavebreak in a model of the human left ventricle. *American Journal of Physiology-Heart and Circulatory Physiology*, 299(1) :H134–H143.

[Kelley et al., 1999] Kelley, S. T., Malekan, R., Gorman, J. H., Jackson, B. M., Gorman, R. C., Suzuki, Y., Plappert, T., Bogen, D. K., Sutton, M. G. S. J., and Edmunds, L. H. (1999). Restraining infarct expansion preserves left ventricular geometry and function after acute anteroapical infarction. *Circulation*, 99(1) :135–142.

[Kerckhoffs et al., 2009] Kerckhoffs, R. C., McCulloch, A. D., Omens, J. H., and Mulligan, L. J. (2009). Effects of biventricular pacing and scar size in a computational model of the failing heart with left bundle branch block. *Medical image analysis*, 13(2) :362–369.

[Kichula et al., 2014] Kichula, E. T., Wang, H., Dorsey, S. M., Szczesny, S. E., Elliott, D. M., Burdick, J. A., and Wenk, J. F. (2014). Experimental and computational investigation of altered mechanical properties in myocardium after hydrogel injection. *Annals of biomedical engineering*, 42(7) :1546–1556.

[Kim et al., 2004] Kim, D., Gilson, W. D., Kramer, C. M., and Epstein, F. H. (2004). Myocardial tissue tracking with two-dimensional cine displacement-encoded mr imaging : Development and initial evaluation 1. *Radiology*, 230(3) :862–871.

[Kimura et al., 1998] Kimura, B. J., Pezeshki, B., Frack, S. A., and DeMaria, A. N. (1998). Feasibility of limited echo imaging : characterization of incidental findings. *Journal of the American Society of Echocardiography*, 11(7) :746–750.

[Klotz et al., 2006] Klotz, S., Hay, I., Zhang, G., Maurer, M., Wang, J., and Burkhoff, D. (2006). Development of heart failure in chronic hypertensive dahl rats focus on heart failure with preserved ejection fraction. *Hypertension*, 47(5) :901–911.

[Kovács et al., 2001] Kovács, S. J., McQueen, D. M., and Peskin, C. S. (2001). Modelling cardiac fluid dynamics and diastolic function. *Philosophical Transactions of the Royal Society of London A : Mathematical, Physical and Engineering Sciences*, 359(1783) :1299–1314.

[Krishnamurthy et al., 2013] Krishnamurthy, A., Villongco, C. T., Chuang, J., Frank, L. R., Nigam, V., Belezzuoli, E., Stark, P., Krummen, D. E., Narayan, S., Omens, J. H., et al. (2013). Patient-specific models of cardiac biomechanics. *Journal of computational physics*, 244 :4–21.

[Lamata et al., 2010] Lamata, P., Niederer, S., Barber, D., Norsletten, D., Lee, J., Hose, R., and Smith, N. (2010). Personalization of cubic hermite meshes for efficient biomechanical simulations. In *International Conference on Medical Image Computing and Computer-Assisted Intervention*, pages 380–387. Springer.

[Lamata et al., 2011] Lamata, P., Niederer, S., Nordsletten, D., Barber, D. C., Roy, I., Hose, D. R., and Smith, N. (2011). An accurate, fast and robust method to generate patient-specific cubic hermite meshes. *Medical image analysis*, 15(6) :801–813.

[Land et al., 2012] Land, S., Niederer, S. A., and Smith, N. P. (2012). Efficient computational methods for strongly coupled cardiac electromechanics. *IEEE Transactions on Biomedical Engineering*, 59(5) :1219–1228.

[Le Bihan and Breton, 1985] Le Bihan, D. and Breton, E. (1985). Imagerie de diffusion in-vivo par résonance magnétique nucléaire. *Comptes-Rendus de l'Académie des Sciences*, 93(5) :27–34.

[Ledesma-Carbayo et al., 2004] Ledesma-Carbayo, M., Santos, A., Kybic, J., Mahia-Casado, P., Garcia-Fernandez, M., Malpica, N., Perez-David, E., and Desco, M. (2004). Myocardial strain analysis of echocardiographic sequences using nonrigid registration. In *Computers in Cardiology, 2004*, pages 313–316. IEEE.

[Lee et al., 2013] Lee, L. C., Wall, S. T., Klepach, D., Ge, L., Zhang, Z., Lee, R. J., Hinson, A., Gorman, J. H., Gorman, R. C., and Guccione, J. M. (2013). Algisyl-lvr-tm with coronary artery bypass grafting reduces left ventricular wall stress and improves function in the failing human heart. *International journal of cardiology*, 168(3) :2022–2028.

[LeGrice et al., 1995a] LeGrice, I., Takayama, Y., and Covell, J. (1995a). Transverse shear along myocardial cleavage planes provides a mechanism for normal systolic wall thickening. *Circulation Research*, 77(1) :182–193.

[LeGrice et al., 1995b] LeGrice, I. J., Smaill, B., Chai, L., Edgar, S., Gavin, J., and Hunter, P. J. (1995b). Laminar structure of the heart : ventricular myocyte arrangement and connective tissue architecture in the dog. *American Journal of Physiology-Heart and Circulatory Physiology*, 269(2) :H571–H582.

[Leitman et al., 2004] Leitman, M., Lysyansky, P., Sidenko, S., Shir, V., Peleg, E., Binenbaum, M., Kaluski, E., Krakover, R., and Vered, Z. (2004). Two-dimensional strain–a novel software for real-time quantitative echocardiographic assessment of myocardial function. *Journal of the American Society of Echocardiography*, 17(10) :1021–1029.

[Lemmon and Yoganathan, 2000a] Lemmon, J. D. and Yoganathan, A. P. (2000a). Computational modeling of left heart diastolic function : examination of ventricular dysfunction. *Journal of biomechanical engineering*, 122(4) :297–303.

[Lemmon and Yoganathan, 2000b] Lemmon, J. D. and Yoganathan, A. P. (2000b). Three-dimensional computational model of left heart diastolic function with fluid–structure interaction. *Journal of biomechanical engineering*, 122(2) :109–117.

[Li et al., 2008a] Li, H., Sumner, R. W., and Pauly, M. (2008a). Global correspondence optimization for non-rigid registration of depth scans. In *Computer graphics forum*, volume 27, pages 1421–1430. Wiley Online Library.

[Li et al., 2008b] Li, J., Greener, I. D., Inada, S., Nikolski, V. P., Yamamoto, M., Hancox, J. C., Zhang, H., Billeter, R., Efimov, I. R., Dobrzynski, H., et al. (2008b). Computer three-dimensional reconstruction of the atrioventricular node. *Circulation Research*, 102(8) :975–985.

[Li and Guskov, 2005] Li, X. and Guskov, I. (2005). Multiscale features for approximate alignment of point-based surfaces. In *Symposium on geometry processing*, volume 255, pages 217–226. Citeseer.

[Lin and Yin, 1998] Lin, D. and Yin, F. (1998). A multiaxial constitutive law for mammalian left ventricular myocardium in steady-state barium contracture or tetanus. *Journal of biomechanical engineering*, 120(4) :504–517.

[Linge et al., 2005] Linge, S., Lines, G., and Sundnes, J. (2005). Solving the heart mechanics equations with newton and quasi newton methods–a comparison. *Computer methods in biomechanics and biomedical engineering*, 8(1) :31–38.

[Liu, 2007] Liu, Y. (2007). A mean field annealing approach to accurate free form shape matching. *Pattern Recognition*, 40(9) :2418–2436.

[Liu et al., 1992] Liu, Y., Bahn, R. C., and Ritman, E. L. (1992). Dynamic intramyocardial blood volume : evaluation with a radiological opaque marker method. *American Journal of Physiology-Heart and Circulatory Physiology*, 263(3) :H963–H967.

[Löhner, 1997] Löhner, R. (1997). Automatic unstructured grid generators. *Finite Elements in Analysis and Design*, 25(1) :111–134.

[Lombaert et al., 2011] Lombaert, H., Peyrat, J.-M., Fanton, L., Cheriet, F., Delingette, H., Ayache, N., Clarysse, P., Magnin, I., and Croisille, P. (2011). Statistical atlas of human cardiac fibers : Comparison with abnormal hearts. In *International Workshop on Statistical Atlases and Computational Models of the Heart*, pages 207–213. Springer.

[Lorusso et al., 1995] Lorusso, A., Eggert, D. W., and Fisher, R. B. (1995). *A comparison of four algorithms for estimating 3-D rigid transformations*. University of Edinburgh, Department of Artificial Intelligence.

[Lower, 1932] Lower, R. (1932). Tractatus de corde, london, 1669. *Prefaced by an Introduc*.

[Lu et al., 2008] Lu, J., Zhou, X., and Raghavan, M. L. (2008). Inverse method of stress analysis for cerebral aneurysms. *Biomechanics and modeling in mechanobiology*, 7(6) :477–486.

[Lynch, 2000] Lynch, J. P. (1987-2000). Generated for multimedia teaching projects by the yale university school of medicine, center for advanced instructional media.

[Macosko and Rheology, 1994] Macosko, C. and Rheology, P. (1994). Measurements and applications. *VCH, New York*.

[Mahrholdt et al., 2005] Mahrholdt, H., Zhydkov, A., Hager, S., Meinhardt, G., Vogelsberg, H., Wagner, A., and Sechtem, U. (2005). Left ventricular wall motion abnormalities as well as reduced wall thickness can cause false positive results of routine spect perfusion imaging for detection of myocardial infarction. *European heart journal*, 26(20) :2127–2135.

[Makadia et al., 2006] Makadia, A., Patterson, A., and Daniilidis, K. (2006). Fully automatic registration of 3d point clouds. In *2006 IEEE Computer Society Conference on Computer Vision and Pattern Recognition (CVPR'06)*, volume 1, pages 1297–1304. IEEE.

[Marchesseau et al., 2013a] Marchesseau, S., Delingette, H., Sermesant, M., and Ayache, N. (2013a). Fast parameter calibration of a cardiac electromechanical model from medical images based on the unscented transform. *Biomechanics and modeling in mechanobiology*, 12(4) :815–831.

[Marchesseau et al., 2013b] Marchesseau, S., Delingette, H., Sermesant, M., Sorine, M., Rhode, K., Duckett, S. G., Rinaldi, C. A., Razavi, R., and Ayache, N. (2013b). Preliminary specificity study of the bestel–clement–sorine electromechanical model of the heart using parameter calibration from medical images. *Journal of the mechanical behavior of biomedical materials*, 20 :259–271.

[Marin and Brankov, 2010] Marin, T. and Brankov, J. G. (2010). Deformable left-ventricle mesh model for motion-compensated filtering in cardiac gated spect. *Medical physics*, 37(10) :5471–5481.

[Masugata et al., 2000] Masugata, H., Mizushige, K., Kinoshita, A., Sakamoto, S., Matsuo, H., Senda, S., and Sakamoto, H. (2000). Comparison of left ventricular diastolic filling with myocyte bulk modulus using doppler echocardiography and acoustic microscopy in pressure-overload left ventricular hypertrophy and cardiac amyloidosis. *Clinical cardiology*, 23(2) :115–122.

[Mayeur et al., 2016] Mayeur, O., Witz, J.-F., Lecomte, P., Brieu, M., Cosson, M., and Miller, K. (2016). Influence of geometry and mechanical properties on the accuracy of patient-specific simulation of women pelvic floor. *Annals of biomedical engineering*, 44(1) :202–212.

[Mazhari and McCulloch, 1999] Mazhari, R. and McCulloch, A. D. (1999). Three-dimensional mechanics of myocardial contraction : mechanisms of transverse systolic stress. *ASME-PUBLICATIONS-BED*, 42 :43–44.

[McCulloch et al., 1991] McCulloch, A., Waldman, L., Rogers, J., and Guccione, J. (1991). Large-scale finite element analysis of the beating heart. *Critical Reviews in Biomedical Engineering*, 20(5-6) :427–449.

[McVeigh et al., 1998] McVeigh, E. R., Prinzen, F. W., Wyman, B. T., Tsitlik, J. E., Halperin, H. R., and Hunter, W. C. (1998). Imaging asynchronous mechanical activation of the paced heart with tagged mri. *Magnetic resonance in medicine*, 39(4) :507–513.

[Michels et al., 1992] Michels, V. V., Moll, P. P., Miller, F. A., Tajik, A. J., Chu, J. S., Driscoll, D. J., Burnett, J. C., Rodeheffer, R. J., Chesebro, J. H., and Tazelaar, H. D. (1992). The frequency of familial dilated cardiomyopathy in a series of patients with idiopathic dilated cardiomyopathy. *New England Journal of Medicine*, 326(2) :77–82.

[Miller and Lu, 2013] Miller, K. and Lu, J. (2013). On the prospect of patient-specific biomechanics without patient-specific properties of tissues. *Journal of the mechanical behavior of biomedical materials*, 27 :154–166.

[Mitra et al., 2007] Mitra, N. J., Flöry, S., Ovsjanikov, M., Gelfand, N., Guibas, L. J., and Pottmann, H. (2007). Dynamic geometry registration. In *Symposium on geometry processing*, pages 173–182.

[Mogensen et al., 2003] Mogensen, J., Kubo, T., Duque, M., Uribe, W., Shaw, A., Murphy, R., Gimeno, J. R., Elliott, P., and McKenna, W. J. (2003). Idiopathic restrictive cardiomyopathy is part of the clinical expression of cardiac troponin i mutations. *The Journal of clinical investigation*, 111(2) :209–216.

[Möller and Trumbore, 2005] Möller, T. and Trumbore, B. (2005). Fast, minimum storage ray/triangle intersection. In *ACM SIGGRAPH 2005 Courses*, page 7. ACM.

[Mondillo et al., 2011] Mondillo, S., Galderisi, M., Mele, D., Cameli, M., Lomoriello, V. S., Zacà, V., Ballo, P., D'Andrea, A., Muraru, D., Losi, M., et al. (2011). Speckle-tracking echocardiography a new technique for assessing myocardial function. *Journal of Ultrasound in Medicine*, 30(1) :71–83.

[Moore et al., 2002] Moore, C. L., Rose, G. A., Tayal, V. S., Sullivan, D. M., Arrowood, J. A., and Kline, J. A. (2002). Determination of left ventricular function by emergency physician echocardiography of hypotensive patients. *Academic Emergency Medicine*, 9(3) :186–193.

[Moorman et al., 2003] Moorman, A., Webb, S., Brown, N. A., Lamers, W., and Anderson, R. H. (2003). Development of the heart :(1) formation of the cardiac chambers and arterial trunks. *Heart*, 89(7) :806–814.

[Mullasari et al., 2011] Mullasari, A. S., Balaji, P., and Khando, T. (2011). Managing complications in acute myocardial infarction. *J Assoc Physicians India*, 59 :43–8.

[Myronenko and Song, 2010] Myronenko, A. and Song, X. (2010). Point set registration : Coherent point drift. *IEEE transactions on pattern analysis and machine intelligence*, 32(12) :2262–2275.

[Nakatani, 2011] Nakatani, S. (2011). Left ventricular rotation and twist : why should we learn ? *Journal of cardiovascular ultrasound*, 19(1) :1–6.

[Nash, 1998] Nash, M. (1998). *Mechanics and material properties of the heart using an anatomically accurate mathematical model*. PhD thesis, ResearchSpace@ Auckland.

[Nash and Hunter, 2000] Nash, M. P. and Hunter, P. J. (2000). Computational mechanics of the heart. *Journal of elasticity and the physical science of solids*, 61(1-3) :113–141.

[Nash and Panfilov, 2004] Nash, M. P. and Panfilov, A. V. (2004). Electromechanical model of excitable tissue to study reentrant cardiac arrhythmias. *Progress in biophysics and molecular biology*, 85(2) :501–522.

[Netter, 1971] Netter, F. (1971). Heart, vol. 5, 293 pp. *The Ciba Collection of Medical Illustrations, Ciba Pharmaceutical Company, Summit, NJ.*

[Network and of Cardiology, 2012] Network, E. H. and of Cardiology, E. S. (2012). cardiovascular disease statistics.

[Niederer et al., 2011] Niederer, S. A., Plank, G., Chinchapatnam, P., Ginks, M., Lamata, P., Rhode, K. S., Rinaldi, C. A., Razavi, R., and Smith, N. P. (2011). Length-dependent tension in the failing heart and the efficacy of cardiac resynchronization therapy. *Cardiovascular research*, 89(2) :336–343.

[Niederer and Smith, 2009] Niederer, S. A. and Smith, N. P. (2009). The role of the frank–starling law in the transduction of cellular work to whole organ pump function : A computational modeling analysis. *PLoS Comput Biol*, 5(4) :e1000371.

[Nielsen et al., 1991] Nielsen, P., Le Grice, I., Smaill, B., and Hunter, P. (1991). Mathematical model of geometry and fibrous structure of the heart. *American Journal of Physiology-Heart and Circulatory Physiology*, 260(4) :H1365–H1378.

[Nordsletten et al., 2011] Nordsletten, D., Niederer, S., Nash, M., Hunter, P., and Smith, N. (2011). Coupling multi-physics models to cardiac mechanics. *Progress in biophysics and molecular biology*, 104(1) :77–88.

[Novak et al., 1994] Novak, V. P., Yin, F., and Humphrey, J. (1994). Regional mechanical properties of passive myocardium. *Journal of biomechanics*, 27(4) :403–412.

[Oduneye et al., 2015] Oduneye, S. O., Pop, M., Shurrab, M., Biswas, L., Ramanan, V., Barry, J., Crystal, E., and Wright, G. A. (2015). Distribution of abnormal potentials in chronic myocardial infarction using a real time magnetic resonance guided electrophysiology system. *Journal of Cardiovascular Magnetic Resonance*, 17(1) :1.

[Oertel and Krittian, 2011] Oertel, H. and Krittian, S. (2011). *Modelling the human cardiac fluid mechanics.* KIT Scientific Publishing.

[Ogden, 1984] Ogden, R. (1984). Non-linear elastic deformations. *Engineering Analysis*, 1(2) :119.

[Ogden, 1997] Ogden, R. W. (1997). *Non-linear elastic deformations.* Courier Corporation.

[Okamoto et al., 2000] Okamoto, R., Moulton, M. J., Peterson, S., Li, D., Pasque, M., and Guccione, J. (2000). Epicardial suction : a new approach to mechanical testing of the passive ventricular wall. *Journal of biomechanical engineering*, 122(5) :479–487.

[Okrasinski et al., 2012] Okrasinski, S. J., Ramachandran, B., and Konofagou, E. E. (2012). Assessment of myocardial elastography performance in phantoms under combined physiologic motion configurations with preliminary in vivo feasibility. *Physics in medicine and biology*, 57(17) :5633.

[Omens et al., 1993] Omens, J., MacKenna, D., and McCulloch, A. (1993). Measurement of strain and analysis of stress in resting rat left ventricular myocardium. *Journal of biomechanics*, 26(6) :665–676.

[Omens and Fung, 1990] Omens, J. H. and Fung, Y.-C. (1990). Residual strain in rat left ventricle. *Circulation Research*, 66(1) :37–45.

[Omens et al., 1991] Omens, J. H., May, K. D., and McCulloch, A. D. (1991). Transmural distribution of three-dimensional strain in the isolated arrested canine left ventricle. *American Journal of Physiology-Heart and Circulatory Physiology*, 261(3) :H918–H928.

[Ordas et al., 2007] Ordas, S., Oubel, E., Leta, R., Carreras, F., and Frangi, A. F. (2007). A statistical shape model of the heart and its application to model-based segmentation. In *Medical imaging*, pages 65111K–65111K. International Society for Optics and Photonics.

[Orderud et al., 2008a] Orderud, F., Kiss, G., Langeland, S., Remme, E. W., Torp, H. G., and Rabben, S. I. (2008a). Combining edge detection with speckle-tracking for cardiac strain assessment in 3d echocardiography. In *2008 IEEE Ultrasonics Symposium*, pages 1959–1962. IEEE.

[Orderud et al., 2008b] Orderud, F., Kiss, G., and Torp, H. G. (2008b). Automatic coupled segmentation of endo-and epicardial borders in 3d echocardiography. In *2008 IEEE Ultrasonics Symposium*, pages 1749–1752. IEEE.

[Ovsjanikov et al., 2010] Ovsjanikov, M., Mérigot, Q., Mémoli, F., and Guibas, L. (2010). One point isometric matching with the heat kernel. In *Computer Graphics Forum*, volume 29, pages 1555–1564. Wiley Online Library.

[Panfilov et al., 2007] Panfilov, A., Keldermann, R., and Nash, M. (2007). Drift and breakup of spiral waves in reaction–diffusion–mechanics systems. *Proceedings of the National Academy of Sciences*, 104(19) :7922–7926.

[Papademetris et al., 2002] Papademetris, X., Sinusas, A. J., Dione, D. P., Constable, R. T., and Duncan, J. S. (2002). Estimation of 3-d left ventricular deformation from medical images using biomechanical models. *IEEE transactions on medical imaging*, 21(7) :786–800.

[Papazov and Burschka, 2011] Papazov, C. and Burschka, D. (2011). Deformable 3d shape registration based on local similarity transforms. In *Computer Graphics Forum*, volume 30, pages 1493–1502. Wiley Online Library.

[Parvatiyar et al., 2010] Parvatiyar, M. S., Pinto, J. R., Dweck, D., and Potter, J. D. (2010). Cardiac troponin mutations and restrictive cardiomyopathy. *BioMed Research International*, 2010.

[Pathmanathan et al., 2009] Pathmanathan, P., Gavaghan, D., and Whiteley, J. (2009). A comparison of numerical methods used for finite element modelling of soft tissue deformation. *The Journal of Strain Analysis for Engineering Design*, 44(5) :391–406.

[Pearlman et al., 1982] Pearlman, E., Weber, K., Janicki, J., Pietra, G., and Fishman, A. (1982). Muscle fiber orientation and connective tissue content in the hypertrophied human heart. *Laboratory investigation ; a journal of technical methods and pathology*, 46(2) :158–164.

[Peddy et al., 2006] Peddy, S. B., Vricella, L. A., Crosson, J. E., Oswald, G. L., Cohn, R. D., Cameron, D. E., Valle, D., and Loeys, B. L. (2006). Infantile restrictive cardiomyopathy resulting from a mutation in the cardiac troponin t gene. *Pediatrics*, 117(5) :1830–1833.

[Pelc et al., 1991] Pelc, N. J., Herfkens, R. J., Shimakawa, A., and Enzmann, D. R. (1991). Phase contrast cine magnetic resonance imaging. *Magnetic resonance quarterly*, 7(4) :229–254.

[Périé et al., 2013] Périé, D., Dahdah, N., Foudis, A., and Curnier, D. (2013). Multi-parametric mri as an indirect evaluation tool of the mechanical properties of in-vitro cardiac tissues. *BMC cardiovascular disorders*, 13(1) :1.

[Perk et al., 2007] Perk, G., Tunick, P. A., and Kronzon, I. (2007). Non-doppler two-dimensional strain imaging by echocardiography–from technical considerations to clinical applications. *Journal of the American Society of Echocardiography*, 20(3) :234–243.

[Perschall et al., 2009] Perschall, M., Spiegel, K., Schenkel, T., and Oertel, H. (2009). Effects of vad placement on 3d fluid flow in a patient specific numerical model of the left ventricle with ischemic heart failure. In *World Congress on Medical Physics and Biomedical Engineering, September 7-12, 2009, Munich, Germany*, pages 611–614. Springer.

[Peskin and McQueen, 1997] Peskin, C. S. and McQueen, D. M. (1997). 14. fluid dynamics of the heart and its valves. *Case Studies in Mathematical Modeling Ecology, Physiology, and Cell Biology*, page 313.

[Pezzuto et al., 2014] Pezzuto, S., Ambrosi, D., and Quarteroni, A. (2014). An orthotropic active–strain model for the myocardium mechanics and its numerical approximation. *European Journal of Mechanics-A/Solids*, 48 :83–96.

[Pop et al., 2009] Pop, M., Sermesant, M., Mansi, T., Crystal, E., Detsky, J., Yang, Y., Fefer, P., McVeigh, E. R., Dick, A., Ayache, N., et al. (2009). Characterization of post-infarct scars in a porcine model–a combined experimental and theoretical study. In *International Conference on Functional Imaging and Modeling of the Heart*, pages 1–10. Springer.

[Prinzen et al., 1995] Prinzen, F. W., Cheriex, E. C., Delhaas, T., van Oosterhout, M. F., Arts, T., Wellens, H. J., and Reneman, R. S. (1995). Asymmetric thickness of the left ventricular wall resulting from asynchronous electric activation : a study in dogs with ventricular pacing and in patients with left bundle branch block. *American heart journal*, 130(5) :1045–1053.

[Raghavan et al., 2006] Raghavan, M., Ma, B., and Fillinger, M. F. (2006). Non-invasive determination of zero-pressure geometry of arterial aneurysms. *Annals of biomedical engineering*, 34(9) :1414–1419.

[Raviv et al., 2010] Raviv, D., Bronstein, A. M., Bronstein, M. M., Kimmel, R., and Sochen, N. (2010). Affine-invariant diffusion geometry for the analysis of deformable 3d shapes. *arXiv preprint arXiv :1012.5933*.

[Reisner et al., 2004] Reisner, S. A., Lysyansky, P., Agmon, Y., Mutlak, D., Lessick, J., and Friedman, Z. (2004). Global longitudinal strain : a novel index of left ventricular systolic function. *Journal of the American Society of Echocardiography*, 17(6) :630–633.

[Ridker, 2003] Ridker, P. M. (2003). Clinical application of c-reactive protein for cardiovascular disease detection and prevention. *Circulation*, 107(3) :363–369.

[Riveros et al., 2013] Riveros, F., Chandra, S., Finol, E. A., Gasser, T. C., and Rodriguez, J. F. (2013). A pull-back algorithm to determine the unloaded vascular geometry in anisotropic hyperelastic aaa passive mechanics. *Annals of biomedical engineering*, 41(4) :694–708.

[Rodrigues, 1840] Rodrigues, O. (1840). *Des lois géométriques qui régissent les déplacements d'un système solide dans l'espace : et de la variation des cordonnées provenant de ces déplacements considérés indépendamment des causes qui peuvent les produire.* publisher not identified.

[Rodriguez et al., 1994] Rodriguez, E. K., Hoger, A., and McCulloch, A. D. (1994). Stress-dependent finite growth in soft elastic tissues. *Journal of biomechanics*, 27(4) :455–467.

[Rodriguez et al., 1993] Rodriguez, E. K., Omens, J. H., Waldman, L., and McCulloch, A. (1993). Effect of residual stress on transmural sarcomere length distributions in rat left ventricle. *American Journal of Physiology-Heart and Circulatory Physiology*, 264(4) :H1048–H1056.

[Rose et al., 2001] Rose, E. A., Gelijns, A. C., Moskowitz, A. J., Heitjan, D. F., Stevenson, L. W., Dembitsky, W., Long, J. W., Ascheim, D. D., Tierney, A. R., Levitan, R. G., et al. (2001). Long-term use of a left ventricular assist device for end-stage heart failure. *New England Journal of Medicine*, 345(20) :1435–1443.

[Ross and Streeter Jr, 1975] Ross, M. and Streeter Jr, D. (1975). Nonuniform subendocardial fiber orientation in the normal macaque left ventricle. *European journal of cardiology*, 3(3) :229–247.

[Rueckert et al., 1999] Rueckert, D., Sonoda, L. I., Hayes, C., Hill, D. L., Leach, M. O., and Hawkes, D. J. (1999). Nonrigid registration using free-form deformations : application to breast mr images. *IEEE transactions on medical imaging*, 18(8) :712–721.

[Rusinkiewicz and Levoy, 2001] Rusinkiewicz, S. and Levoy, M. (2001). Efficient variants of the icp algorithm. In *3-D Digital Imaging and Modeling, 2001. Proceedings. Third International Conference on*, pages 145–152. IEEE.

[Sabbah et al., 2013] Sabbah, H. N., Wang, M., Gupta, R. C., Rastogi, S., Ilsar, I., Sabbah, M. S., Kohli, S., Helgerson, S., and Lee, R. J. (2013). Augmentation of left ventricular wall thickness with alginate hydrogel implants improves left ventricular function and prevents progressive remodeling in dogs with chronic heart failure. *JACC : Heart Failure*, 1(3) :252–258.

[Sachse, 2004] Sachse, F. B. (2004). *Computational cardiology : modeling of anatomy, electrophysiology, and mechanics*, volume 2966. Springer Science & Business Media.

[Sahillioğlu and Yemez, 2012] Sahillioğlu, Y. and Yemez, Y. (2012). Minimum-distortion isometric shape correspondence using em algorithm. *IEEE transactions on pattern analysis and machine intelligence*, 34(11) :2203–2215.

[Schenkel et al., 2009] Schenkel, T., Malve, M., Reik, M., Markl, M., Jung, B., and Oertel, H. (2009). Mri-based cfd analysis of flow in a human left ventricle : methodology and application to a healthy heart. *Annals of biomedical engineering*, 37(3) :503–515.

[Schmid et al., 2009] Schmid, H., Wang, Y., Ashton, J., Ehret, A., Krittian, S., Nash, M., and Hunter, P. (2009). Myocardial material parameter estimation : a comparison of invariant based orthotropic constitutive equations. *Computer methods in biomechanics and biomedical engineering*, 12(3) :283–295.

[Scollan et al., 2000] Scollan, D., Holmes, A., Zhang, J., and Winslow, R. (2000). Reconstruction of cardiac ventricular geometry and fiber orientation using magnetic resonance imaging. *Annals of biomedical engineering*, 28(8) :934–944.

[Scollan et al., 1998] Scollan, D. F., Holmes, A., Winslow, R., and Forder, J. (1998). Histological validation of myocardial microstructure obtained from diffusion tensor magnetic resonance imaging. *American Journal of Physiology-Heart and Circulatory Physiology*, 275(6) :H2308–H2318.

[Seemann et al., 2006] Seemann, G., Keller, D., Weiss, D., and Dossel, O. (2006). Modeling human ventricular geometry and fiber orientation based on diffusion tensor mri. In *2006 Computers in Cardiology*, pages 801–804. IEEE.

[Seo et al., 2014] Seo, Y., Ishizu, T., and Aonuma, K. (2014). Current status of 3-dimensional speckle tracking echocardiography : a review from our experiences. *Journal of cardiovascular ultrasound*, 22(2) :49–57.

[Sermesant et al., 2001] Sermesant, M., Coudière, Y., Delingette, H., Ayache, N., and Désidéri, J.-A. (2001). An electromechanical model of the heart for cardiac image analysis. In *International Conference on Medical Image Computing and Computer-Assisted Intervention*, pages 224–231. Springer.

[Serri et al., 2006] Serri, K., Reant, P., Lafitte, M., Berhouet, M., Le Bouffos, V., Roudaut, R., and Lafitte, S. (2006). Global and regional myocardial function quantification by two-dimensional strain : application in hypertrophic cardiomyopathy. *Journal of the American College of Cardiology*, 47(6) :1175–1181.

[Shaw et al., 2008] Shaw, S. M., Fox, D. J., and Williams, S. G. (2008). The development of left ventricular torsion and its clinical relevance. *International journal of cardiology*, 130(3) :319–325.

[Shea and Sweeney, 2003] Shea, J. B. and Sweeney, M. O. (2003). Cardiac resynchronization therapy a patient's guide. *Circulation*, 108(9) :e64–e66.

[Shi et al., 2010] Shi, W. V., Chang, T. N., and Zhou, M. (2010). Method to detect cardiac abnormalities based on electrocardiography and sinoatrial pacemaker model. In *Mechatronics and Automation (ICMA), 2010 International Conference on*, pages 566–571. IEEE.

[Shim et al., 2012] Shim, J., Grosberg, A., Nawroth, J. C., Parker, K. K., and Bertoldi, K. (2012). Modeling of cardiac muscle thin films : pre-stretch, passive and active behavior. *Journal of biomechanics*, 45(5) :832–841.

[Sigal et al., 2008] Sigal, I. A., Hardisty, M. R., and Whyne, C. M. (2008). Mesh-morphing algorithms for specimen-specific finite element modeling. *Journal of biomechanics*, 41(7) :1381–1389.

[Simo et al., 1985] Simo, J., Taylor, R., and Pister, K. (1985). Variational and projection methods for the volume constraint in finite deformation elasto-plasticity. *Computer Methods in Applied Mechanics and Engineering*, 51(1) :177–208.

[Smaill and Hunter, 1991] Smaill, B. and Hunter, P. (1991). Structure and function of the diastolic heart : material properties of passive myocardium. In *Theory of heart*, pages 1–29. Springer.

[Spottiswoode et al., 2007] Spottiswoode, B. S., Zhong, X., Hess, A., Kramer, C., Meintjes, E. M., Mayosi, B. M., and Epstein, F. H. (2007). Tracking myocardial motion from cine dense images using spatiotemporal phase unwrapping and temporal fitting. *IEEE Transactions on medical imaging*, 26(1) :15–30.

[Staten et al., 2011] Staten, M. L., Owen, S. J., Shontz, S. M., Salinger, A. G., and Coffey, T. S. (2011). A comparison of mesh morphing methods for 3d shape optimization. In *Proceedings of the 20th international meshing roundtable*, pages 293–311. Springer.

[Streeter, 1979] Streeter, D. D. (1979). Gross morphology and fiber geometry of the heart. *Handbook of physiology*, pages 61–112.

[Streeter and Bassett, 1966] Streeter, D. D. and Bassett, D. L. (1966). An engineering analysis of myocardial fiber orientation in pig's left ventricle in systole. *The Anatomical Record*, 155(4) :503–511.

[Streeter and Hanna, 1973] Streeter, D. D. and Hanna, W. T. (1973). Engineering mechanics for successive states in canine left ventricular myocardium i. cavity and wall geometry. *Circulation Research*, 33(6) :639–655.

[Streeter et al., 1978] Streeter, D. D., Powers, W., Ross, M. A., and Torrent-Guasp, F. (1978). Three-dimensional fiber orientation in the mammalian left ventricular wall. *Cardiovascular system dynamics*, pages 73–84.

[Streeter et al., 1969] Streeter, D. D., Spotnitz, H. M., Patel, D. P., Ross, J., and Sonnenblick, E. H. (1969). Fiber orientation in the canine left ventricle during diastole and systole. *Circulation research*, 24(3) :339–347.

[Sugihara et al., 1997] Sugihara, H., Tamaki, N., Nozawa, M., Ohmura, T., et al. (1997). Septal perfusion and wall thickening in patients with left bundle branch block assessed by technetium-99m-sestamibi gated tomography. *The Journal of Nuclear Medicine*, 38(4) :545.

[Sun et al., 2009] Sun, J., Ovsjanikov, M., and Guibas, L. (2009). A concise and provably informative multi-scale signature based on heat diffusion. In *Computer graphics forum*, volume 28, pages 1383–1392. Wiley Online Library.

[Sundnes et al., 2006] Sundnes, J., Lines, G. T., Cai, X., Nielsen, B. F., Mardal, K.-A., and Tveito, A. (2006). Physiological background. In *Computing the Electrical Activity in the Heart*, pages 1–19. Springer.

[Sundnes et al., 2007] Sundnes, J., Lines, G. T., Cai, X., Nielsen, B. F., Mardal, K.-A., and Tveito, A. (2007). *Computing the electrical activity in the heart*, volume 1. Springer Science & Business Media.

[Tam et al., 2013] Tam, G. K., Cheng, Z.-Q., Lai, Y.-K., Langbein, F. C., Liu, Y., Marshall, D., Martin, R. R., Sun, X.-F., and Rosin, P. L. (2013). Registration of 3d point clouds and meshes : a survey from rigid to nonrigid. *IEEE transactions on visualization and computer graphics*, 19(7) :1199–1217.

[Teske et al., 2007] Teske, A. J., De Boeck, B. W., Melman, P. G., Sieswerda, G. T., Doevendans, P. A., and Cramer, M. J. (2007). Echocardiographic quantification of myocardial function using tissue deformation imaging, a guide to image acquisition and analysis using tissue doppler and speckle tracking. *Cardiovascular ultrasound*, 5(1) :1.

[Torrent-Guasp, 1980] Torrent-Guasp, F. (1980). La estructuración macroscópica del miocardio ventricular. *Rev Esp Cardiol*, 33(3) :265–87.

[Trabelsi et al., 2015] Trabelsi, O., Davis, F. M., Rodriguez-Matas, J. F., Duprey, A., and Avril, S. (2015). Patient specific stress and rupture analysis of ascending thoracic aneurysms. *Journal of biomechanics*, 48(10) :1836–1843.

[Tustison and Amini, 2006] Tustison, N. J. and Amini, A. A. (2006). Biventricular myocardial strains via nonrigid registration of anfigatomical nurbs models. *IEEE Transactions on Medical Imaging*, 25(1) :94–112.

[Underwood et al., 1986] Underwood, S., Rees, R., Savage, P., Klipstein, R., Firmin, D., Fox, K., Poole-Wilson, P., and Longmore, D. (1986). Assessment of regional left ventricular function by magnetic resonance. *British heart journal*, 56(4) :334–340.

[Usyk et al., 2000] Usyk, T., Mazhari, R., and McCulloch, A. (2000). Effect of laminar orthotropic myofiber architecture on regional stress and strain in the canine left ventricle. *Journal of elasticity and the physical science of solids*, 61(1-3) :143–164.

[Usyk and McCulloch, 2003] Usyk, T. P. and McCulloch, A. D. (2003). Computational methods for soft tissue biomechanics. In *Biomechanics of soft tissue in cardiovascular systems*, pages 273–342. Springer.

[Van Kaick et al., 2011] Van Kaick, O., Zhang, H., Hamarneh, G., and Cohen-Or, D. (2011). A survey on shape correspondence. In *Computer Graphics Forum*, volume 30, pages 1681–1707. Wiley Online Library.

[Vendelin et al., 2002] Vendelin, M., Bovendeerd, P. H., Engelbrecht, J., and Arts, T. (2002). Optimizing ventricular fibers : uniform strain or stress, but not atp consumption, leads to high efficiency. *American Journal of Physiology-Heart and Circulatory Physiology*, 283(3) :H1072–H1081.

[Veress et al., 2005] Veress, A. I., Gullberg, G. T., and Weiss, J. A. (2005). Measurement of strain in the left ventricle during diastole with cine-mri and deformable image registration. *Journal of biomechanical engineering*, 127(7) :1195–1207.

[Veress et al., 2011] Veress, A. I., Segars, W. P., Tsui, B. M., and Gullberg, G. T. (2011). Incorporation of a left ventricle finite element model defining infarction into the xcat imaging phantom. *IEEE transactions on medical imaging*, 30(4) :915–927.

[Vergroesen et al., 1987] Vergroesen, I., Noble, M., and Spaan, J. (1987). Intramyocardial blood volume change in first moments of cardiac arrest in anesthetized goats. *American Journal of Physiology-Heart and Circulatory Physiology*, 253(2) :H307–H316.

[Vernooy et al., 2005] Vernooy, K., Verbeek, X. A., Peschar, M., Crijns, H. J., Arts, T., Cornelussen, R. N., and Prinzen, F. W. (2005). Left bundle branch block induces ventricular remodelling and functional septal hypoperfusion. *European Heart Journal*, 26(1) :91–98.

[Vetter and McCulloch, 1998] Vetter, F. J. and McCulloch, A. D. (1998). Three-dimensional analysis of regional cardiac function : a model of rabbit ventricular anatomy. *Progress in biophysics and molecular biology*, 69(2) :157–183.

[Vos et al., 2015] Vos, T., Barber, R. M., Bell, B., Bertozzi-Villa, A., Biryukov, S., Bolliger, I., Charlson, F., Davis, A., Degenhardt, L., Dicker, D., et al. (2015). Global, regional, and national incidence, prevalence, and years lived with disability for 301 acute and chronic diseases and injuries in 188 countries, 1990–2013 : a systematic analysis for the global burden of disease study 2013. *The Lancet*, 386(9995) :743–800.

[Vossoughi et al., 1980] Vossoughi, J., Vaishnav, R. N., and Patel, D. J. (1980). Compressibility of the myocardial tissue. *Advances in bioengineering*, pages 45–48.

[Wael et al., 2016] Wael, M., Ibrahim, E.-S. H., and Fahmy, A. S. (2016). Detection of cardiac function abnormality from mri images using normalized wall thickness temporal patterns. *International journal of biomedical imaging*, 2016.

[Walker et al., 2005a] Walker, J. C., Guccione, J. M., Jiang, Y., Zhang, P., Wallace, A. W., Hsu, E. W., and Ratcliffe, M. B. (2005a). Helical myofiber orientation after myocardial infarction and left ventricular surgical restoration in sheep. *The Journal of thoracic and cardiovascular surgery*, 129(2) :382–390.

[Walker et al., 2005b] Walker, J. C., Ratcliffe, M. B., Zhang, P., Wallace, A. W., Fata, B., Hsu, E. W., Saloner, D., and Guccione, J. M. (2005b). Mri-based finite-element analysis of left ventricular aneurysm. *American Journal of Physiology-Heart and Circulatory Physiology*, 289(2) :H692–H700.

[Walker et al., 2008] Walker, J. C., Ratcliffe, M. B., Zhang, P., Wallace, A. W., Hsu, E. W., Saloner, D. A., and Guccione, J. M. (2008). Magnetic resonance imaging-based finite element stress analysis after linear repair of left ventricular aneurysm. *The Journal of thoracic and cardiovascular surgery*, 135(5) :1094–1102.

[Wang et al., 2002] Wang, D. H., Makaroun, M. S., Webster, M. W., and Vorp, D. A. (2002). Effect of intraluminal thrombus on wall stress in patient-specific models of abdominal aortic aneurysm. *Journal of Vascular Surgery*, 36(3) :598–604.

[Wang and Amini, 2012] Wang, H. and Amini, A. A. (2012). Cardiac motion and deformation recovery from mri : a review. *IEEE Transactions on Medical Imaging*, 31(2) :487–503.

[Wang et al., 2013] Wang, H., Gao, H., Luo, X., Berry, C., Griffith, B. E., Ogden, R., and Wang, T. (2013). Structure-based finite strain modelling of the human left ventricle in diastole. *International journal for numerical methods in biomedical engineering*, 29(1) :83–103.

[Weber, 1989] Weber, K. T. (1989). Cardiac interstitium in health and disease : the fibrillar collagen network. *Journal of the American College of Cardiology*, 13(7) :1637–1652.

[Weiss et al., 1996] Weiss, J. A., Maker, B. N., and Govindjee, S. (1996). Finite element implementation of incompressible, transversely isotropic hyperelasticity. *Computer methods in applied mechanics and engineering*, 135(1) :107–128.

[Wenk et al., 2011] Wenk, J. F., Sun, K., Zhang, Z., Soleimani, M., Ge, L., Saloner, D., Wallace, A. W., Ratcliffe, M. B., and Guccione, J. M. (2011). Regional left ventricular myocardial contractility and stress in a finite element model of posterobasal myocardial infarction. *Journal of biomechanical engineering*, 133(4) :044501.

[Wenk et al., 2009] Wenk, J. F., Wall, S. T., Peterson, R. C., Helgerson, S. L., Sabbah, H. N., Burger, M., Stander, N., Ratcliffe, M. B., Guccione, J. M., et al. (2009). A method for automatically optimizing medical devices for treating heart failure : designing polymeric injection patterns. *Journal of biomechanical engineering*, 131(12) :121011.

[WHO, 2012] WHO (2012). World health organisation : The top 10 causes of death statistics.

[Willenheimer et al., 1997] Willenheimer, R. B., Israelsson, B. A., Cline, C. M., and Erhardt, L. R. (1997). Simplified echocardiography in the diagnosis of heart failure. *Scandinavian Cardiovascular Journal*, 31(1) :9–16.

[Williams, 1956] Williams, E. (1956). Hooke's law and the concept of the elastic limit. *Annals of Science*, 12(1) :74–83.

[Winslow, 1711] Winslow, J. (1711). Observations sur les fibres du coeur et sur ses valvules. *Histoire (et Mémoires) de l'Academie Royale des Sciences (Paris)*, (1714) :151–6.

[Wu et al., 2006] Wu, M.-T., Tseng, W.-Y. I., Su, M.-Y. M., Liu, C.-P., Chiou, K.-R., Wedeen, V. J., Reese, T. G., and Yang, C.-F. (2006). Diffusion tensor magnetic resonance imaging mapping the fiber architecture remodeling in human myocardium after infarction correlation with viability and wall motion. *Circulation*, 114(10) :1036–1045.

[Wyman et al., 1999] Wyman, B. T., Hunter, W. C., Prinzen, F. W., and McVeigh, E. R. (1999). Mapping propagation of mechanical activation in the paced heart with mri tagging. *American Journal of Physiology-Heart and Circulatory Physiology*, 276(3) :H881–H891.

[Xi et al., 2011] Xi, J., Lamata, P., Lee, J., Moireau, P., Chapelle, D., and Smith, N. (2011). Myocardial transversely isotropic material parameter estimation from in-silico measurements based on a reduced-order unscented kalman filter. *Journal of the mechanical behavior of biomedical materials*, 4(7) :1090–1102.

[Yamaji et al., 2005] Yamaji, K., Fujimoto, S., Ikeda, Y., Masuda, K., Nakamura, S., Saito, Y., and Yutani, C. (2005). Apoptotic myocardial cell death in the setting of arrhythmogenic right ventricular cardiomyopathy. *Acta cardiologica*, 60(5) :465–470.

[Yang et al., 2006] Yang, Z., Bowles, N. E., Scherer, S. E., Taylor, M. D., Kearney, D. L., Ge, S., Nadvoretskiy, V. V., DeFreitas, G., Carabello, B., Brandon, L. I., et al. (2006). Desmosomal dysfunction due to mutations in desmoplakin causes arrhythmogenic right ventricular dysplasia/cardiomyopathy. *Circulation research*, 99(6) :646–655.

[Yeh et al., 2011] Yeh, I.-C., Lin, C.-H., Sorkine, O., and Lee, T.-Y. (2011). Template-based 3d model fitting using dual-domain relaxation. *IEEE Transactions on Visualization and Computer Graphics*, 17(8) :1178–1190.

[Yettram and Beecham, 1998] Yettram, A. and Beecham, M. (1998). An analytical method for the determination of along-fibre to cross-fibre elastic modulus ratio in ventricular myocardium : a feasibility study. *Medical engineering & physics*, 20(2) :103–108.

[Yin, 1984] Yin, F. (1984). Applications of the finite-element method to ventricular mechanics. *Critical reviews in biomedical engineering*, 12(4) :311–342.

[Yin et al., 1996] Yin, F., Chan, C., and Judd, R. M. (1996). Compressibility of perfused passive myocardium. *American Journal of Physiology-Heart and Circulatory Physiology*, 271(5) :H1864–H1870.

[Yin et al., 1987] Yin, F. C., Strumpf, R. K., Chew, P. H., and Zeger, S. L. (1987). Quantification of the mechanical properties of noncontracting canine myocardium under simultaneous biaxial loading. *Journal of biomechanics*, 20(6) :577–589.

[Young et al., 2008] Young, P., Beresford-West, T., Coward, S., Notarberardino, B., Walker, B., and Abdul-Aziz, A. (2008). An efficient approach to converting three-dimensional image data into highly accurate computational models. *Philosophical Transactions of the Royal Society of London A : Mathematical, Physical and Engineering Sciences*, 366(1878) :3155–3173.

[Yousef et al., 2009] Yousef, Z. R., Foley, P. W., Khadjooi, K., Chalil, S., Sandman, H., Mohammed, N. U., and Leyva, F. (2009). Left ventricular non-compaction : clinical features and cardiovascular magnetic resonance imaging. *BMC cardiovascular disorders*, 9(1) :37.

[Ypenburg et al., 2009] Ypenburg, C., van Bommel, R. J., Borleffs, C. J. W., Bleeker, G. B., Boersma, E., Schalij, M. J., and Bax, J. J. (2009). Long-term prognosis after cardiac resynchronization therapy is related to the extent of left ventricular reverse remodeling at midterm follow-up. *Journal of the American College of Cardiology*, 53(6) :483–490.

[Zemzemi, 2009] Zemzemi, N. (2009). *Theoretical and Numerical study of the electric activity of the heart. Modeling and Numerical simulation of electrocardiograms.* PhD thesis, Université Paris Sud-Paris XI.

[Zerhouni et al., 1988] Zerhouni, E. A., Parish, D. M., Rogers, W. J., Yang, A., and Shapiro, E. P. (1988). Human heart : tagging with mr imaging–a method for noninvasive assessment of myocardial motion. *Radiology*, 169(1) :59–63.

[Zhang et al., 2008] Zhang, H., Sheffer, A., Cohen-Or, D., Zhou, Q., Van Kaick, O., and Tagliasacchi, A. (2008). Deformation-driven shape correspondence. In *Computer Graphics Forum*, volume 27, pages 1431–1439. Wiley Online Library.

[Zhuang et al., 2010] Zhuang, X., Rhode, K. S., Razavi, R. S., Hawkes, D. J., and Ourselin, S. (2010). A registration-based propagation framework for automatic whole heart segmentation of cardiac mri. *IEEE transactions on medical imaging*, 29(9) :1612–1625.

[Zienkiewicz et al., 1977] Zienkiewicz, O. C., Taylor, R. L., Zienkiewicz, O. C., and Taylor, R. L. (1977). *The finite element method*, volume 3. McGraw-hill London.

Annexe A

Développements préliminaires: Modèle de matériau anisotrope pour le logiciel Abaqus®

Préambule

Dans ce chapitre, une nouvelle subroutine pour le logiciel Abaqus a été développé. Cette Subroutine, décrit le comportement du tissu cardiaque comme expliqué par [Guccione et al., 1991]. Cette fonction d'énergie de déformation est le résultat d'essais biaxiaux qui peut déterminer le comportement d'isotrope transverse du matériau en phase passive du cycle cardiaque. Pour ce code, les équations proposées par [Ateshian and Costa, 2009] ont été utilisées.

Cette subroutine a été comparé pour un test de gonflement avec un modèle de type Fung codé sur le logiciel Abaqus® et les résultats montrent une bonne concordance.

Ensuite, un modèle test EFs cubique a été créé afin de comparer les impacts des différents paramètres de matériau sur cet élément sachant que les mêmes fonction d'énergie de déformation et valeur de contrainte active ont été utilisées. Les résultats montrent que les paramètres de matériau dans le modèle de Guccione ont un impact important sur les valeurs de contrainte et déformation. Cela montre que différents protocoles expérimentaux et l'état du spécimen peuvent influer sur l'ensemble des paramètres. En outre, obtenir une solution unique pour une équation exponentielle est une tâche difficile.

Enfin, ce code a été utilisé pour contracter le VG de référence (chapitre 3). Une simulation par EFs quasi-statique avec la méthode Newton-Raphson modifiée a été utilisée. La simulation a atteint avec succès sa convergence et les résultats ont été analysés.

A.1 Perspective and future work: preliminary developments of transversely isotropic constitutive material model in Abaqus® software

ABSTRACT

Cardiovascular simulations using patient-specific geometries need an accurate mechanical behaviour which describes the left ventricle (LV) movements. A simulation with reliable material model and material parameters (MPs) can help researchers to understand the mechanical behaviour of LV which is responsible for pumping blood through cardiovascular system under different loading conditions and pathologies. In order to represent the myocardium behaviour, one should consider the nonlinear interactions between the responses to different cardiac cycle loading patterns ; the impact of the laminar myofibers plane structure ; the influence of transverse plane stresses produced by the myocyte chains ; and the collagen-fiber relationship. These complex interactions in macro-scale are mechanical but strongly coupled to the electrophysiological processes in micro-scale and the blood flow in the heart cavities. Therefore, a complete electro-mechanical framework should contain models for electrical signal propagation through myocytes in cell level coupled to the whole organ movement as well as fluid interaction to the heart structure. This work aims at developing a Guccione material model for Abaqus® software. However, the available finite-element (FE) simulation software are not representing adequately the behaviour of LV tissue which should represent reliably both the nonlinear passive and active behaviour of LV. Here, we focus on the macro-scale of mechanical behaviour of LV structure. A frame-work for Guccione material model has been developed in Fortran® language for Abaqus® software. This subroutine have been compared in an inflation test with the Fung-type model in Abaqus® and the results show a good agreement in this comparison. Then, we developed myocyte contraction equation in this subroutine and applied it to a healthy reference LV.

GRAPHICAL ABSTRACT

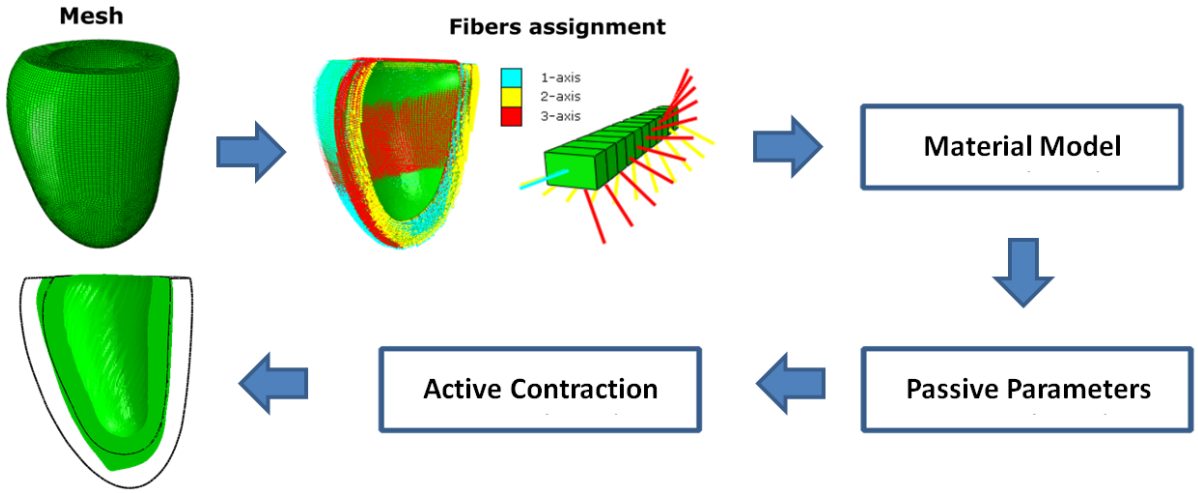

HIGHLIGHTS

— A new subroutine code for isotropic transversely material model developed for Abaqus® software.

— This study shows that the MPs have important impact on the exponential strain energy function under the same active stress and boundary conditions on a cubic FE model.

— The subroutine successfully achieved the convergence in a quasi-static simulation of a healthy LV.

KEY WORDS: LV ; Abaqus® subroutine ; isotropic transverse Guccione material model.

A.1.1 Introduction

Mechanical response of passive myocardium muscle has been proposed to be isotropic transverse or orthotropic material. Three orthogonal directions (fiber, myocyte sheet and normal to fiber-sheet) define locally the behaviour of this complex tissue. To describe such models, one should consider 3D spatial and temporal movement of the left ventricle (LV) specimen during an experimental test following an estimation of their proper material parameters (MPs). The collection of such nonlinear responses needs an adequate and detailed mathematical model. Then, one should validate the uniqueness of solution which is a very difficult task for highly nonlinear behaviour and large numbers of parameters to be identified [Holzapfel and Ogden, 2009]. The results can vary dependant on the location of specimen as LV thickness varies from base to apex, the loading conditions, experimental setup and the specimen [Holzapfel and Ogden, 2009], [Guccione et al., 1995] and [Usyk et al., 2000].

Several models have been developed based on whether myocardial tissue is transversal isotropic or orthotropic material model. One common transversely isotropic model is described by [Guccione et al., 1991, Costa et al., 1996] which has been widely used for MPs identification and finite-element (FE) modelling. This model has an exponential equation with slightly less parameters to be identified. Further, more complicated models which explain more precisely the myocardium behaviour have been developed considering the orthotropic assumption with several exponential equations [Costa et al., 2001,Schmid et al., 2009,Holzapfel and Ogden, 2009] and MPs constants. However, the detailed equations for FE implantation of such orthotropic models are not well explained in the literature [Pezzuto et al., 2014].

The proper material model for cardiac tissue and, more specifically, for myocyte contraction have not been yet developed based on the state-of-the-art in the Abaqus® software which is the reference tool for nonlinear FE analysis in solid mechanics problems. The purpose of this work is to describe the implementation of one of the most commonly used cardiac transverse isotropic material model [Guccione et al., 1991] into Abaqus® software to perform a cardiac cycle. For this, a new subroutine in Fortran® language has been developed to calculate the stress tensors as a function of strain components as well as the elasticity tensor. The aim is to overcome challenges to handle strong nonlinearity, the incompressibility of myocardium tissue, and taking into account the fibre orientation in the FE model and in tensor calculations.

This paper is organised as follows: first, we describe the model and equations to reconstruct the stress and spatial elasticity tensor. Then, we described equations for myocyte contraction to be used in our developed material model and applied it with several MPs from literature.

We, then, apply these equations for contracting the reference LV model. We present our results following by a verification of this developed code by inflating a reference LV and compare its results with the existing Fung-type material model in Abaqus® at end diastolic. Finally, we discuss our results and limitations to this work.

A.1.2 Methods

Myocardium is considered as a nearly incompressible material. We define a nonlinear strain energy function based on exponential strain energy proposed by [Guccione et al., 1995]. In order to ease the FE simulation to take into account the myocardial incompressibility and to avoid element locking, we coupled a volumetric (dilatational) part to the distortional Guccione equation (isochoric) as explained previously in for instance [Simo et al., 1985, Weiss et al., 1996, Bonet and Wood, 1997, Holzapfel and Ogden, 2009]. The resulting model describes the cardiac tissue as a transversely isotropic material, with a characteristic direction aligned with the local fiber orientation.

$$\begin{aligned} W &= \overline{W} + U(J), \\ \overline{W} &= \frac{1}{2}c(exp(Q) - 1), \\ Q &= b_3\overline{E}_{ff}^2 + b_2(\overline{E}_{ss}^2 + \overline{E}_{nn}^2 + 2\overline{E}_{sn}^2) + b_1(2\overline{E}_{fs}^2 + 2\overline{E}_{fn}^2). \end{aligned} \tag{6}$$

where $\overline{W}$ is a function of six independent distortional components of Green-Lagrange strain tensor $\overline{\mathbf{E}} = \frac{1}{2}(\overline{\mathbf{C}} - 1)$ in *fiber (f)*, *sheet (s)* and *sheet-normal (n)* directions, $\overline{\mathbf{C}} = \overline{\mathbf{F}}^T\overline{\mathbf{F}}$ is distortional right Cauchy-Green tensor, $\overline{\mathbf{F}} = J^{-1/3}\mathbf{F}$ is, $U(J)$ is the volumetric part which often is a polynomial function of J that is the determinant of distortional deformation gradient ($det(\overline{\mathbf{F}}) = 1$), and c and b_{1-3} are four MPs values which have been identified from experimental tests.

Formulations to Reconstruct the Cauchy Stress Tensor

As it has been mentioned in the introduction to develop the subroutine in Abaqus® software, the Cauchy stress and the spatial elasticity tensors should be reconstructed in the code. In continuum mechanics, second order stress tensor consists of nine components (also symmetric) which explains the state of an element inside the material at deformed configuration. This tensor, once, in material (undeformed) configuration is expressed as the second Piola-Kirchhoff stress ($\mathbf{S}$) and it derives from a strain energy function such as in Equation 6. In case where the material is nearly incompressible this total stress parameter can be decomposed into

distortional and volumetric parts [Holzapfel, 2000]. The volumetric part is a function of hydrostatic pressure which interpreted from total deformation gradient. The distortional part derives from the deviatoric second Piola-Kirchhoff stress $\overline{\mathbf{S}} = \partial\overline{W}/\partial\overline{\mathbf{E}}$ where $\overline{W}$ and $\overline{\mathbf{E}}$, therefore, will develop from the strain energy function (Equation 6).

$$\mathbf{S} = \frac{\partial W}{\partial \mathbf{E}} = -Jp\mathbf{C}^{-1} + J^{-2/3}\mathbf{DEV}(\overline{\mathbf{S}}), \tag{7}$$

where, $\mathbf{DEV}(\cdot) = (\cdot) - \frac{1}{3}[(\cdot) : \overline{\mathbf{C}}]\overline{\mathbf{C}}^{-1}$ is the deviatoric operator in the material frame of $\overline{\mathbf{S}}$, $\mathbf{C} = \mathbf{F}^{-1}\mathbf{F}$ is right Cauchy-Green tensor and $p = -dU/dJ$ is the hydrostatic pressure derived from dilatational part of the stress.

Then, we can drive the Cauchy stress tensor similarly:

$$\sigma = -p\mathbf{I} + \mathbf{dev}\overline{\sigma}. \tag{8}$$

where, $\mathbf{dev}(\cdot) = (\cdot) - \frac{1}{3}[(\cdot) : \mathbf{I}]\mathbf{I}^{-1}$ is the deviatoric operator in the spatial frame, $\overline{\sigma} = J\overline{\mathbf{FSF}}^{T}$.

We define the volumetric part later in the application on different FE simulations. This equation will give the hydrostatic pressure (represents also the total dilatational stress) in the first strain energy function derivatives and to reconstruct the spatial elasticity tensor.

Formulations for Elasticity Tensor

The elasticity tensor is the bridge to explain how a material deforms under prescribed loading conditions (stress). Therefore, the incremental strain can be computed via this tensor from the stress. We use the equations stated in the work of [Ateshian and Costa, 2009] to reconstruct the material and spatial (current frame) elasticity tensors. The material elasticity tensor is obtained by differentiating the stress tensor defined in Equation 7 with respect to the components of the Green-Lagrange strain components. We refer to [Simo et al., 1985, Weiss et al., 1996] for the detailed mathematical derivations, and here simply we state the expression for $\mathbb{C}$:

$$\begin{aligned}
\mathbb{C} &= 2Jp\mathbf{C}^{-1}\underline{\overline{\otimes}}\mathbf{C}^{-1} - J(p + J\frac{dp}{dJ})\mathbf{C}^{-1}\otimes\mathbf{C}^{-1} \\
&+ J^{-4/3}[\overline{\mathbb{C}} - \frac{1}{3}[\overline{\mathbb{C}} : (\overline{\mathbf{C}}\otimes\overline{\mathbf{C}}^{-1}) + (\overline{\mathbf{C}}^{-1}\otimes\overline{\mathbf{C}}) : \overline{\mathbb{C}}] - \frac{1}{3}(\overline{\mathbf{C}} : \overline{\mathbb{C}} : \overline{\mathbf{C}})(\overline{\mathbf{C}}^{-1}\otimes\overline{\mathbf{C}}^{-1})] \\
&+ \frac{2}{3}[(\overline{\mathbf{C}} : \overline{\mathbf{S}})(\overline{\mathbf{C}}^{-1}\underline{\overline{\otimes}}\overline{\mathbf{C}}^{-1} + \frac{1}{3}\overline{\mathbf{C}}^{-1}\otimes\overline{\mathbf{C}}^{-1}) - (\overline{\mathbf{S}}\otimes\overline{\mathbf{C}}^{-1} + \overline{\mathbf{C}}^{-1}\otimes\overline{\mathbf{S}})],
\end{aligned} \tag{9}$$

where, $\otimes$ and $\underline{\otimes}$ are the tensor dyadic products (refer to the Appendix A.1.5), (:) is the double contraction operator between tensors of different orders which are mentioned in Appendix A.1.5 [Bonet and Wood, 1997, Ateshian et al., 2007] and $\overline{\mathbb{C}} = \frac{\partial^2 \overline{W}}{\partial \overline{\mathbf{E}}^2}$ is the distortional part of material elasticity tensor.

The first line of the right hand side of Equation 9 (the first two terms) is the volumetric contribution, the second line (third term) is the distortional contribution, etc. If we push-forward the Equation 9, we obtain the spatial elasticity tensor (Equation 10) which will be used in the equations of our developed subroutine of material model.

$$\begin{aligned}\mathcal{C} &= 2p\mathbf{I}\underline{\otimes}\mathbf{I} - (p + J\frac{dp}{dJ})\mathbf{I}\otimes\mathbf{I} \\ &+ \overline{\mathcal{C}} - \frac{1}{3}[\overline{\mathcal{C}} : (\mathbf{I}\otimes\mathbf{I}) + (\mathbf{I}\otimes\mathbf{I}) : \overline{\mathcal{C}} - \frac{1}{3}(\mathbf{I} : \overline{\mathcal{C}} : \mathbf{I})(\mathbf{I}\otimes\mathbf{I})] \\ &+ \frac{2}{3}[(\mathbf{I} : \overline{\sigma})(\mathbf{I}\underline{\otimes}\mathbf{I} + \frac{1}{3}\mathbf{I}\otimes\mathbf{I}) - (\overline{\sigma}\otimes\mathbf{I} + \mathbf{I}\otimes\overline{\sigma})].\end{aligned} \tag{10}$$

where $\overline{\mathcal{C}} = J^{-1}(\mathbf{F}\underline{\otimes}\mathbf{F}) : \overline{\mathbb{C}} : (\mathbf{F}^T\underline{\otimes}\mathbf{F}^T)$ as previously defined in [Simo et al., 1985, Weiss et al., 1996, Ateshian et al., 2007] and $\underline{\otimes}$ is the tensor dyadic product from [Bonet and Wood, 1997] (refer to the Appendix A.1.5).

For introducing these equations in Abaqus® software, two tensors should be calculated in subroutine. The first tensor is the Cauchy stress and the second one is the spatial elasticity tensor in matrix representation. The FE software, in each iteration, returns the deformation gradient and from this tensor in local coordinate system, we can calculate the second Piola-Kirchhoff stress and Cauchy stress. Further, we reconstruct the reduced second-order elasticity tensor (6×6) from the fourth-order spatial elasticity tensor given from Equation 10. The second-order spatial elasticity tensor which has been introduced in subroutine code is given as following:

$$\mathcal{C} = \begin{pmatrix} \mathcal{C}_{1111} & \mathcal{C}_{1122} & \mathcal{C}_{1133} & \mathcal{C}_{1112} & \mathcal{C}_{1113} & \mathcal{C}_{1123} \\ & \mathcal{C}_{2222} & \mathcal{C}_{2233} & \mathcal{C}_{2212} & \mathcal{C}_{2213} & \mathcal{C}_{2223} \\ & & \mathcal{C}_{3333} & \mathcal{C}_{3312} & \mathcal{C}_{3313} & \mathcal{C}_{3323} \\ & \text{Sym.} & & \mathcal{C}_{1212} & \mathcal{C}_{1213} & \mathcal{C}_{1223} \\ & & & & \mathcal{C}_{1313} & \mathcal{C}_{1323} \\ & & & & & \mathcal{C}_{2323} \end{pmatrix} \tag{11}$$

Knowing that the fourth-order spatial elasticity tensor has symmetry properties (refer to the Appendix A.1.5).

We developed these equations in Fortran language as a new material model. This in-house

code is presented in Appendix A.1.5 which calculates all the variables in local coordinate system.

Contraction Model

We aimed to perform a systolic numerical simulation with our developed subroutine. The systolic contraction is more complex due to complexity of myocyte structure. It is a combination of two mechanical actions: the action of the endocardial blood pressure and the myocyte contraction. Having this in mind, the Equation 8 can be expanded in:

$$\sigma_{\mathbf{total}} = \sigma_{\mathbf{passve}} + \sigma_{\mathbf{active}}, \tag{12}$$

where $\sigma_{\mathbf{active}}$ is the contribution of the myocyte contraction in total Cauchy stress.

The approximation of complex myocyte active contraction values in different directions is yet a challenge in cardiac domain. The active Cauchy stresses in shear local directions are assumed to be zero. Then from Equation 8, the Cauchy stress tensor becomes zero in shear local directions. Due to the lack of experimental tests to determine the fiber transverse stresses (a_n and a_s for *normal* and *sheet* directions, respectively), these parameters were also considered to be zero on the Cauchy tensor diagonal. Therefore, the only non-zero value in the Equation 13 will be the active stress in the fiber direction. However, it has been showed that the transverse fiber directions can be described as a function of the active fiber stress component ($20 - 60\%$) from biaxial tests to fit to the experimental results [Usyk and McCulloch, 2003, Lin and Yin, 1998, Usyk et al., 2000].

The $\sigma_{\mathbf{active}}$ was defined as following for cardiac tissue [Usyk and McCulloch, 2003]:

$$\sigma_{\mathbf{active}} = J^{-1}\mathbf{F}\mathbf{R}_f{}^{-1} \begin{bmatrix} 0 & 0 & 0 \\ 0 & 0 & 0 \\ 0 & 0 & a_f \end{bmatrix} \mathbf{R}_f\mathbf{F}^T, \tag{13}$$

where a_f is the active tension developed by the contracting fibers.

Although the active contraction is a complex dependant variable [Nash and Panfilov, 2004], we considered it only as a function of time which ramps to its maximum value as it has been proposed before [Walker et al., 2005b, Dorri et al., 2006].

We modified the subroutine in order to model the myocyte contraction for FE simulation with different MPs in the literature. This study will show the difference of proposed MPs in the literature in active contraction.

Test Cases

Two geometrical models were considered in this paper : a hegaxedral element and a healthy LV obtained from US images. The hexahedral element of the edge size equal to 2 mm. Then, for the contraction phase, a local orthonormal basis denoted $(\vec{\mathbf{e}}_1, \vec{\mathbf{e}}_2, \vec{\mathbf{e}}_3)$ has been assigned in the center of this element where $\vec{\mathbf{e}}_3$ is aligned with the local fiber orientation in the reference configuration (Figure A1). As boundary conditions, one face of this element was fixed in order to keep the element in 3D space. The MPs assigned to this element are mentioned in Table A1.

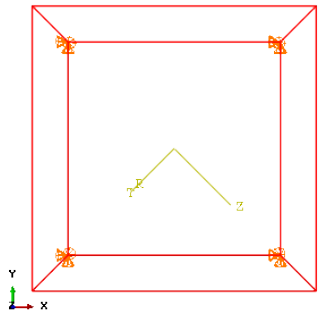

FIGURE A1 – FE cube generated to study the impact of MPs on the stress results. The local coordinate system is shown in yellow vectors. One face of this element was fixed in order to avoid rigid body deformation in 3D space.

For the reference LV FE model, we employed a healthy volunteer LV extracted from 4D US at end-diastole (ED) or end-systole (ES). In order to describe the fiber directional dependency, we defined a local curvilinear coordinate system for each element of reconstructed FE LV model (refer to Chapter 3). The basal nodes assigned to remain coplanar as the LV boundary condition.

Systole Phase for the Reference LV

We aimed to study the response of the LV during systolic phase for an anisotropic material model. The contraction model is explained previously in Section A.1.2 to model the complex torsion and rotation of LV model. We applied active contraction value $a_f = 135$ kPa in the fiber direction as the only non-zero parameter in active contraction tensor. A quasi-static FE simulation has been performed with Standard solver in Abaqus® software.

The basal part was fixed to stay coplanar to avoid rigid body motions and the systolic

pressure was applied to the endocardial surface equal to 11.24 kPa [Dorri et al., 2006]. The volumetric equation for this part is taken from volumetric part of [Marchesseau et al., 2013b]:

$$U(J) = \frac{k}{2}(J-1)^2, \tag{14}$$

A.1.3 Results

The MPs and the stress results across the equatorial plane are presented in Table A1 for diastolic simulation of the reference LV model. Figure A2 shows the impact of the same contraction value and strain energy function in hexahedral element for various MPs mentioned in Table A1. This figure illustrates the sensitivity of one element to different MPs.

Figure A3 shows the results of LV contraction in Maximum Principal stress and displacements. The EF calculated is 61.27% which is in the range for a healthy contraction [HRS, 2014] where the cavity volume reduced from 94.09 to 36.436ml. Figure A4 show several transversal cuts of contracted LV overlaid with ED geometry by 10 mm of intervals. The wall thickness at equatorial plane is about $\sim 11\%$

Table A1 – MPs attributed to the cubic element for Guccione strain energy function.

	c kPa	b_3	b_2	b_1
1. [Okamoto et al., 2000]	0.512	67.1	24.2	21.6
2. [Keldermann et al., 2010]	1.2	26.7	13.5	14.7
3. [Wenk et al., 2009]	0.33	49.3	19.3	17.4
4. [Walker et al., 2005b]	0.128	53.7	21.3	17.3
5. [Walker et al., 2005b]	0.146	67.1	26.6	21.6
6. [Walker et al., 2005b]	0.233	49.3	19.3	17.4
7. [Xi et al., 2011]	0.189	29.9	13.5	13.3
8. [Augenstein et al., 2005]	3	11.1	1.8	10
9. [Land et al., 2012]	1.662	14.3	4.5	10
10. [Omens et al., 1991]	2.4	26.7	2	14.7
11. [Walker et al., 2005b]	0.359	67.1	24.2	21.6
12. [Omens et al., 1993]	2.2	9.2	2	3.7

Material Model verification

In Abaqus® software, a compressible Fung-type exponential model has been developed for passive material behaviour [AbaqusGeneralizedFungform, 2016]. This model can be transfor-

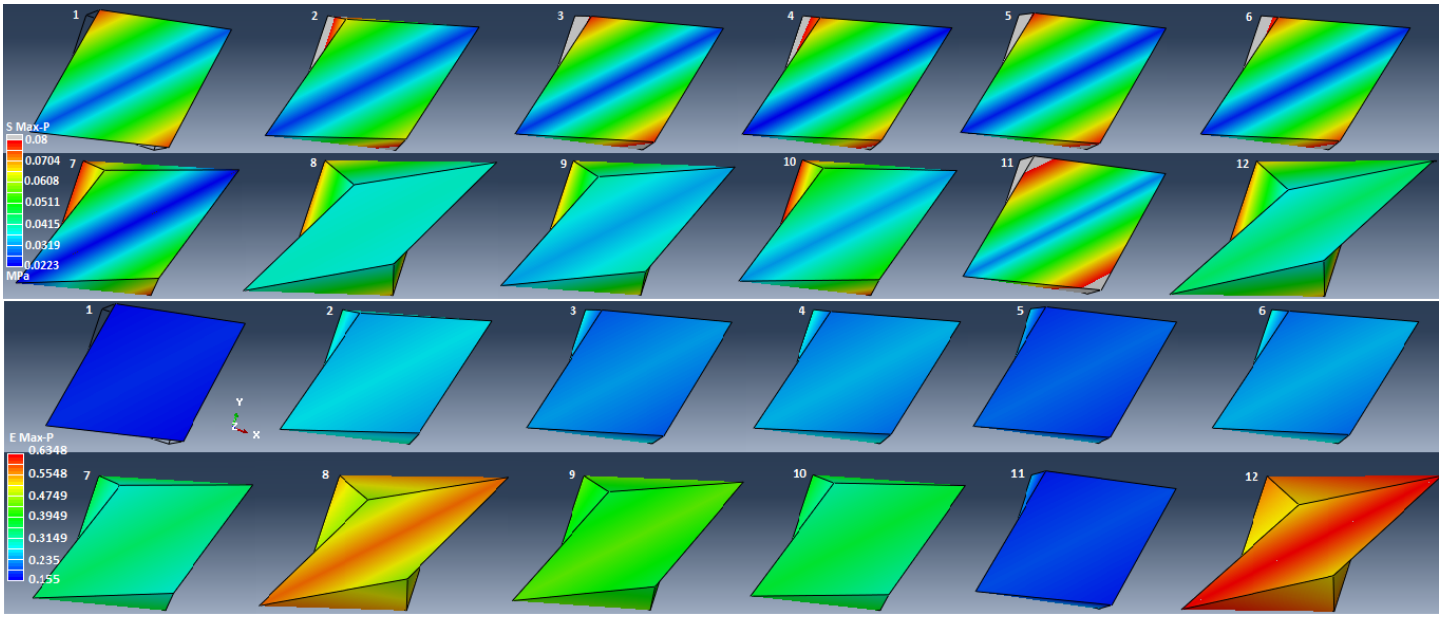

FIGURE A2 – The impacts of MPs on the Maximum-Principal stresses and strains in the FE cube.

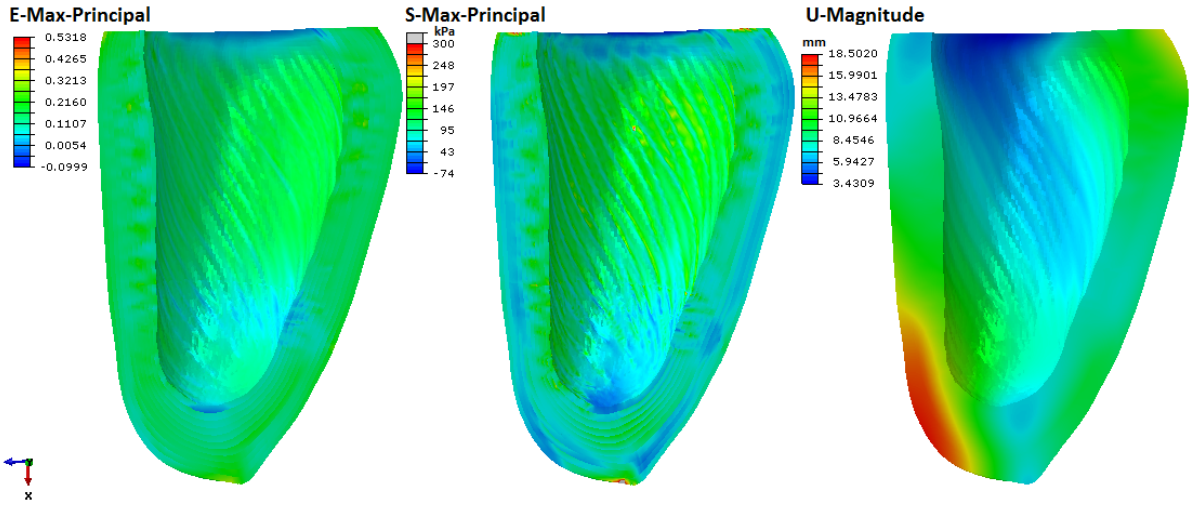

FIGURE A3 – The contracted reference LV results. The Maximum stress (MPa), the strain and displacements (mm) are shown in this figure.

med carefully to isotropic transverse material model by defining the stiffness tensor constants. In order to validate that the in-house code is implemented correctly, we performed two FE simulations. The first simulation is the in-house code for a passive inflation and the second one is the existing Fung-type model ($W = \frac{1}{2}c(e^Q - 1)$) in Abaqus® [AbaqusGeneralizedFungform, 2016, Ateshian and Costa, 2009]. The exponential power differs from what has been described in Guccione material model to: $Q = \overline{E}_{ij} b_{ijkl} \overline{E}_{kl}$ where b_{ijkl} are dimensionless symmetric fourth-order tensor of material constants and $\overline{E}$ are the components of distortional Green-Lagrange

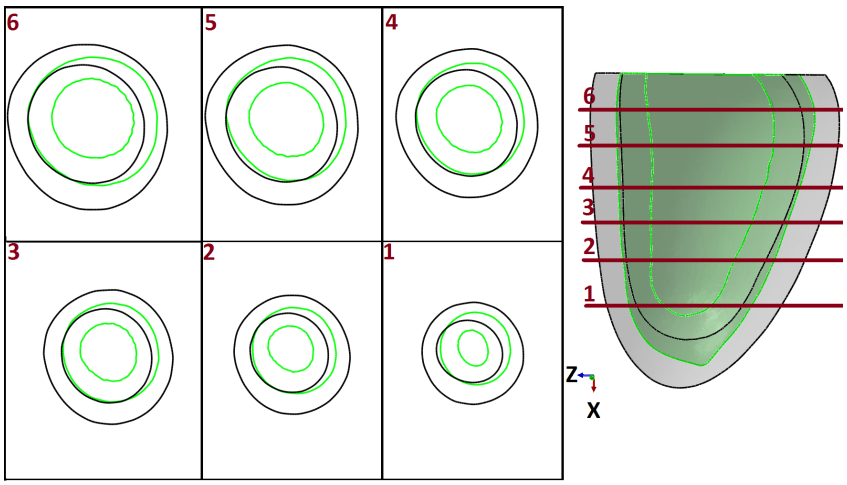

FIGURE A4 – Transversal cuts ($10mm$) of contracted reference LV (green shaded) overlaid on the ED (grey shaded) geometry. At the equatorial, we have observed 11% increase in the wall thickness.

strain tensor.

One advantage is that we have the possibility to attribute different volumetric equation for the small compressible behaviour. Refer to the Equation 6, we have to define $U(J)$ similar to the developed equation in Abaqus®:

$$U(J) = \frac{k}{2}(\frac{J^2-1}{2} - ln(J)), \tag{15}$$

where, k is the bulk modulus for volumetric variations.

Then, the hydrostatic pressure and its derivative to the determinant of deformation gradient for elasticity tensor become:

$$p = -\frac{\partial U}{\partial J} = -\frac{k}{2}(J - J^{-1}), \tag{16}$$

$$\frac{\partial p}{\partial J} = -\frac{k}{2}(1 + J^{-2}). \tag{17}$$

We attributed the MPs from literature (Table A1.7) to inflate the reference LV model with 2kPa for both material models.

The Figure A5 shows the comparison of the developed material model results with the existing Fung-type strain energy function in Abaqus®. The Maximum-Principal stresses and displacements for a diastolic pressure equal to 2 kPa are shown in this figure [AbaqusGeneralizedFungform, 2016].

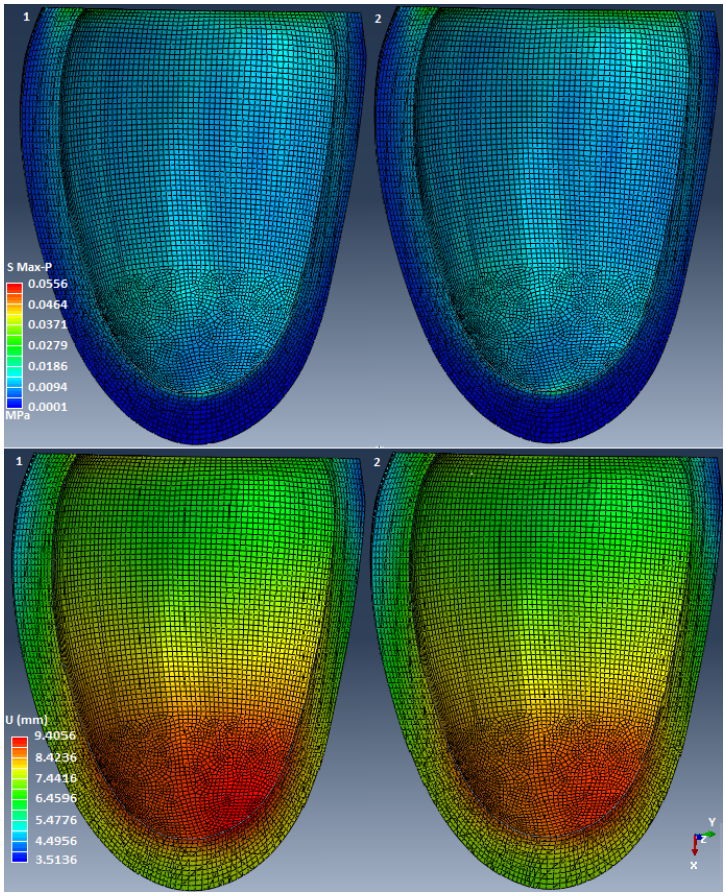

FIGURE A5 – The developed subroutine results compared to the Fung-type material model which already developed in this FE software. The Maximum-Principal stresses and displacements are shown in this figure.

A.1.4 Discussion & Conclusion

In this work, we have developed an in-house code to describe the anisotropic myocardium behaviour. We have verified the results of this code by performing a FE simulation and comparing the results with the existing Fung-type model in Abaqus® software. The results in Figure A5 show a very good agreement between the obtained results.

We also studied the impact of MPs on a hexahedral element contraction. We have previously showed that the stresses in Fung-type models are sensitive to the MPs (refer to Chapter 3). Here we showed that for the same set of MPs, the contraction of this element behaves differently. This again highlights the importance of MPs choices and designing the experimental tests to identify the best set. However, identifying the best solution for an exponential function is a challenging task and the solution might not be unique since the myocardium tissue changes dramatically during a cycle. Also this is shown in Figure A2 that for different sets, the cubic element results are approximately similar (such as 4 & 7 and $2, 3, 5$ & 6).

In Figure A2, cases number 1 and 11 have the same exponential MPs with different c values. Indeed, number 11 has deformed slightly more and has higher stress values due to lower c value. Number 5 has the same exponential parameters for b_1 and b_3 and slightly higher b_2 and lower c which resulted in similar deformation to number 11 with lower stress distributions.

In case of LV contraction, we were limited to one active stress value due to the computational costs of this FE simulation. There were two difficulties in the system: first, the high nonlinear expressions of strain energy function and second, we observed buckling of our system on the apex and endocardial surface which made the convergence complicated and so reduced time steps. Despite all these difficulties, the simulation has successfully reached its total convergence. A modified algorithm of the *Newton-Raphson* for solving equations has been used to improve the convergence of this FE solution. This buckling on the apex can be due to the lack of real data for fiber orientations as in some regions at the apex we observed a sudden concentration of stress values. At the basal part, we observed high values of stress due to the imposed boundary conditions in longitudinal direction and also inhomogeneous stress values in apex. The Maximum-Principal stress is varying between 95 to 200 kPa in this simulation while there are some negative stress values at apex and basal part which is due to the hydrostatic pressure reaction and elements bulking. The Von-Mises stress is varying between $97-230$ kPa which is a wider range as previously reported in the range of $100-150$ kPa [Dorri et al., 2006, McCulloch et al., 1991, Guccione and McCulloch, 1993, Hunter et al., 1998]

The assigned orientations were considered a linear increase from outside to the inside of tissue thickness which is not smooth enough for such simulation. One improvement to this work is to use the fiber directions obtained from DT-MRI images [Vetter and McCulloch, 1998, Hsu et al., 1998, Scollan et al., 1998, Scollan et al., 2000, Chen et al., 2003, Burton et al., 2006, Seemann et al., 2006, Hooks et al., 2007, Li et al., 2008b, Lombaert et al., 2011].

This work is the first step to develop an anisotropic material model for cardiac tissue and needs to be improved in contraction model ; FE mesh and fiber orientations in order to reproduce a realistic anisotropic material behaviour of the LV. The only improvement to this code for a fully anisotropic material will be to change the first and second derivatives of the second Piola-Kirchhoff stresses. In addition, it should be compared with real image data to validate its FE results.

A.1.5 Complementary Data

Tensor double contractions

For second-order tensors $\mathbf{M}$ and $\mathbf{N}$: $\mathbf{M} : \mathbf{N} = M_{ij}N_{ij}$

For fourth-order tensor $\mathbf{M}$, third-order tensor $\mathbf{N}$, and second-order $\mathbf{T}$:

$(\mathbf{M} : \mathbf{T})_{ij} = M_{ijkl}T_{kl}$, $(\mathbf{T} : \mathbf{M})_{ij} = T_{kl}M_{klij}$, $(\mathbf{N} : \mathbf{T})_{i} = N_{ijk}T_{jk}$, $(\mathbf{N} : \mathbf{M})_{ijk} = N_{ilm}M_{lmjk}$

For two fourth-order tensors of $\mathbf{M}$ and $\mathbf{N}$: $(\mathbf{M} : \mathbf{N})_{ijkl} = M_{ijmn}N_{mnkl}$

Tensor dyadic products

For two second-order tensors $\mathbf{M}$ and $\mathbf{N}$:

$(\mathbf{M} \otimes \mathbf{N})_{ijkl} = M_{ij}N_{kl}$, $(\mathbf{M}\overline{\otimes}\mathbf{N})_{ijkl} = \frac{1}{2}(M_{ik}N_{jl} + M_{il}N_{jk})$, $(\mathbf{M}\underline{\otimes}\mathbf{N})_{ijkl} = (M_{ik}N_{jl})$

Elasticity tensor symmetry properties

From Hooke's law and the stress/strain symmetries for a fourth-order stiffness tensor $\mathbf{M}$, we can reduce the material constants to 21 from 81 constants:

$\mathbf{M}_{ijkl} = \mathbf{M}_{jikl} = \mathbf{M}_{ijlk} = \mathbf{M}_{klij}$

Developed subroutine programmed in Fortran® language

```
      SUBROUTINE UMAT(STRESS, STATEV, DDSDDE, SSE, SPD, SCD, RPL,
     1 DDSDDT, DRPLDE, DRPLDT, STRAN, DSTRAN, TIME, DTIME, TEMP, DTEMP,
     2 PREDEF, DPRED, CMNAME, NDI, NSHR, NTENS, NSTATV, PROPS, NPROPS,
     3 COORDS, DROT, PNEWDT, CELENT, DFGRD0, DFGRD1, NOEL, NPT, LAYER,
     4 KSPT, KSTEP, KINC)
C
      INCLUDE 'aba_param.inc'
C
      CHARACTER*8 CMNAME
C
      DIMENSION STRESS(NTENS), STATEV(NSTATV), DDSDDE(NTENS, NTENS),
     1 DDSDDT(NTENS), DRPLDE(NTENS), STRAN(NTENS), DSTRAN(NTENS),
     2 PREDEF(1), DPRED(1), PROPS(NPROPS), COORDS(3), DROT(3, 3),
     3 DFGRD0(3, 3), DFGRD1(3, 3), TIME(2)
C ---------------------------------------------------------------
      PARAMETER (ZERO=0.D0, ONE=1.D0, TWO=2.D0, THREE=3.D0, FOUR=4.D0,
     1 SIX=6.D0)
      Real(8), dimension(3,3) :: DISTGR, Sbar, Ebar, Ident, Cbar, C,
     1 invC, S, Dev, Sigbar, sigma, Dev1,
     1 term5
      Real(8), dimension(9,9) :: DDWDDE, term1, term2, term3, term4,
     1 term8, term9, L, Lbar1, Lbar2, Lbar3,
     1 Lbar4, Lbar, AAAA
      Real(8) cc, b1, b2, b3, af, K, term6, term7, PP, dpdj
      Real(8) af1, aff, DDP, DDP1, DET, Q, FIB
C ----------MPs in MPa
      cc=0.000512
      b1=21.6
      b2=24.2
      b3=67.1
      K=0.1
C ----------CONTRACTION PARAMETERS IF IT IS ACTIVE
      aff=0.135
      af1 = TIME(1)*aff
C ----------CALCULATE THE FBAR FROM DEFORMATION GRADIENT
      call determinant(DFGRD1, DET)
      SCALE=DET**(-ONE/THREE)
      DO K1=1, 3
       DO K2=1, 3
        DISTGR(K2, K1)=SCALE*DFGRD1(K2, K1)
       END DO
      END DO
C ----------CALCULATE THE C AND CBAR
      Ident = reshape((/ one, zero, zero, zero,
     1 one, zero, zero, zero, one /), shape(Ident))                    ! Identity matrix
      C = MATMUL(TRANSPOSE(DFGRD1),DFGRD1)
      Cbar = MATMUL(TRANSPOSE(DISTGR),DISTGR)                    ! DISTGR = Fbar
C ----------CALCULATE THE EBAR AND Q IN STRAIN ENEGRY FUNCTION
      Ebar = one/two*(Cbar - Ident)
      Q = b3*Ebar(3,3)**two + b2*(Ebar(1,1)**two +
     1  Ebar(2,2)**two + two*Ebar(1,2)**two) +
     1  b1*(two*Ebar(1,3)**two + two*Ebar(2,3)**two)
      FIB = cc* EXP(Q)
C ----------CALCULATE THE SBAR AND THE HYDROSTATIC PRESSURE DEPEND ON U(J)
      Sbar(1,1)= FIB*b2*Ebar(1,1)
      Sbar(2,2)= FIB*b2*Ebar(2,2)
      Sbar(3,3)= FIB*b3*Ebar(3,3)
      Sbar(1,2)= FIB*two*b2*Ebar(1,2)
      Sbar(1,3)= FIB*two*b1*Ebar(1,3)
      Sbar(2,3)= FIB*two*b1*Ebar(2,3)
      DO K1=1, 3
       DO K2=1, K1-1
        Sbar(K1, K2) = Sbar(K2, K1)
       END DO
      END DO
      call Inverse33(C,invC)
      call Ddotproduct33(Sbar, C, DDP)                    ! Sbar:C
C---------------------------------------------------------------
      PP = -K*log(DET)                    ! Hydrostatic pressure
      Dev = Sbar - one/three*DDP*invC
      S = DET**(-two/three)* Dev - DET*PP*invC
C ----------CALCULATE THE SIGBAR
      Sigbar = DET**(-one)*MATMUL(MATMUL(DISTGR,Sbar),
     1 TRANSPOSE(DISTGR))
C
      call Ddotproduct33(Sigbar, Ident, DDP1)
      Dev1 = Sigbar - one/three*DDP1*Ident
      sigma = Dev1 - PP*Ident     ! Cauchy stress
C ----------CALCULATE THE SECOND DERIVATIVES OF STRAIN ENERGY FUNCTION
```

C

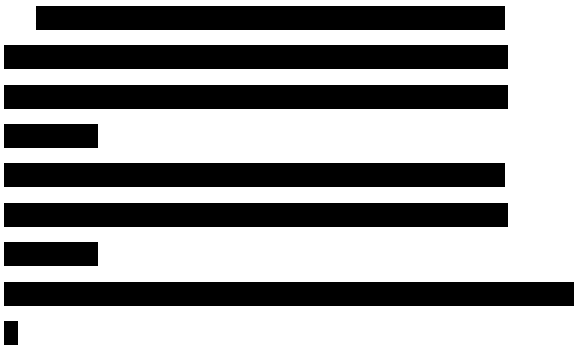

```
      do K1 = 1,9
       do K2 = 1,K1-1
         DDWDDE(K1, K2)=DDWDDE(K2, K1)
       enddo
      enddo
C ----------CALCULATE AND RECONSTRUCT THE FOURTH-ORDER ELASTICITY TENSOR L
      call AvKroneckerProduct33(Ident, Ident, term1)
              ! 9*9     term1 = I AX I
      call KroneckerProduct(Ident, Ident, term2)
                           ! 9*9     term2 = I X I
      call HKroneckerProduct33(DISTGR, DISTGR, Lbar1)
              !9*9       Lbar1 = Fbar hX Fbar
      call                        HKroneckerProduct33(TRANSPOSE(DISTGR),
TRANSPOSE(DISTGR),   Lbar2)!9*9   "Lbar2   =   transpose(Fbar)   hX
transpose(Fbar)"
     C
      call Ddotproduct99(Lbar1, DDWDDE, Lbar3)
                        ! 9*9   Lbar3 =  Lbar1 : DDWDDE
      call Ddotproduct99(Lbar3, Lbar2, Lbar4)
                           !9*9       Lbar4 = Lbar3 : Lbar2
      Lbar = DET**(-one)*Lbar4
                           !9*9
      call Ddotproduct99(Lbar, term2, term3)
              ! 9*9       term3 = Lbar X term2
      call Ddotproduct99(term2, Lbar, term4)
              ! 9*9       term4 = term2 X Lbar
      call Ddotproduct93(Lbar, Ident, term5)
                           ! 3*3       term5 = Lbar : I
      call Ddotproduct33(Ident, term5, term6)
              ! scaler    term6 = I : term5
      call Ddotproduct33(Ident, Sigbar, term7)
                           ! scaler    term7 = I : Tbar
      call KroneckerProduct(Sigbar, Ident, term8)
                           ! 9*9       term8 = Tbar X I
      call KroneckerProduct(Ident, Sigbar, term9)
                           ! 9*9       term9 = I X Tbar
C-------------------------------------------------------------
     dpdj=-K/DET
                           ! derivative of hydrostatic pressure to J
C-----------L
      L = two*PP*term1 - (PP+DET*dpdj)* term2 + Lbar - one/three*(term3
```

```
+ term4 - one/three*term6*term2) + two/three*(term7*(term1 + one/three*term2) - (term8 + term9))
C---------------------------------------------------------------
C ----------CALCULATE THE CAUCHY STRESS
      DO K1=1,NDI
      STRESS(K1)= sigma(K1,K1)
      END DO
            STRESS(3)= STRESS(3) +af1
      STRESS(4)= sigma(1,2)
      STRESS(5)= sigma(1,3)
      STRESS(6)= sigma(2,3)
C ----------RECONSTRUCT THE FINAL STIFFNESS TENSOR
      DDSDDE(1, 1)= L(1,1)
      DDSDDE(2, 2)= L(5,5)
      DDSDDE(3, 3)= L(9,9)
      DDSDDE(4, 4)= L(1,5)
      DDSDDE(5, 5)= L(1,9)
      DDSDDE(6, 6)= L(5,9)

      DDSDDE(1, 2)= L(2,2)
      DDSDDE(1, 3)= L(3,3)
      DDSDDE(1, 4)= L(1,2)
      DDSDDE(1, 5)= L(1,3)
      DDSDDE(1, 6)= L(2,3)
C
      DDSDDE(2, 3)= L(6,6)
      DDSDDE(2, 4)= L(4,5)
      DDSDDE(2, 5)= L(4,6)
      DDSDDE(2, 6)= L(5,6)
C
      DDSDDE(3, 4)= L(7,8)
      DDSDDE(3, 5)= L(7,9)
      DDSDDE(3, 6)= L(8,9)
C
      DDSDDE(4,5)= L(1,6)
      DDSDDE(4,6)= L(2,6)
C
      DDSDDE(5,6)= L(2,9)
 C
      DO K1=1, NTENS
        DO K2=1, K1-1
          DDSDDE(K1,K2) = DDSDDE(K2,K1)
        END DO
      END DO
C=============================================================
C Subroutines which were used in this code to calculate mathematical operations
C=============================================================
C=============================================================
```

Annexe B

Abbréviation

3D : three dimensional

AHA : American heart association

ALE : arbitrary lagrangian eulerian

AS : area strain

AAS : average active stress

AV : atrioventriculaire, atrioventricular

BBG : bloc de branche gauche

CAs : coronary arteries

CHF : congestive heart failure

CMP : cardiomyopathy

CRT : cardiac resynchronization therapy

CT scan : scanner de tomodensitométrie

CVP : coefficients of variation in percentage

DTMRI : diffusion tensor for MRI

ECG : electrocardiogram

EDV : end-diastole cavity volume

EF : ejection fraction

EFs : éléments finis

ES : end-systole

ESV : end-systole cavity volume

FE : finite-element

FEA : finite-element analysis

GE : general electric

HMT : Hunter-McCulloch-terKeurs

IBP : intracavital blood pressure

ICP : iterative closest point

KaHMo : Karlsruhe heart model

LSQ : least squared method

LBBB : left bundle branch block

LV : left ventricle

MCV : maladies cardiovasculaires

MI : myocardial infarctions

MPs : material parameters

MRI : magnetic resonance imagining

NSTEMI : Non ST segment Elevated Myocardial Infarction

RC : resynchronisation cardiaque

RDFE : the reference deformable FE

ROI : region of interest

RS : radial strain

RV : right ventricle

SA : sino-atrial, sino-atrial

STEMI : ST segment Elevation Myocardial Infarction

SVD : singular value decomposition

TDIRM : tenseur de diffusion par l'IRM

US : ultrason

VAD : ventricular assist devices

VG : ventricule gauche

ZPGs : zero-pressure geometries

École Nationale Supérieure des Mines de Saint-Étienne

NNT : *2017LYSEM004*

Sareh BEHDADFAR

CONTRIBUTION TO PATIENT-SPECIFIC STRESS ASSESSMENT IN THE HUMAN LEFT VENTRICLE USING IMAGE-BASED FINITEELEMENT ANALYSES

Speciality: Mechanics and Engineering

Keywords: Left ventricle, patient-specific, finite element modelling, GE healthcare ultrasound

Abstract:

Mechanical stresses in the left ventricle of the heart may present abnormalities which gradually can result in heart failure. It is therefore important to be able to rebuild accurately this behaviour in order to understand, analyse, diagnose and treat cardiac dysfunction. In this context, personalized or patient-specific finite element simulations of the heart are of a great interest, but there remain several challenges in clinical routine accessibility. It is essential to bear in mind that no imaging method allows access to the mechanical properties of the cardiac tissue or the state of residual stresses of each patient. These two data are necessary to reconstruct the stress fields in the heart using state of the art. In this thesis, we have worked on two problems:

1. The stress field in the cardiac tissue can be predicted by the finite element models but it requires precise determination of the tissue's mechanical properties. Some models require more than 11 values to be determined, therefore, it is not realistic to identify these parameters for each individual. The question is, therefore: Is it possible to reconstruct the stress field in cardiac tissue given the uncertainty of the mechanical properties? It is thus shown that for several constitutive models, the stress dependency on the parameters is low.
2. Mechanical models often require high spatial resolution imaging data to reconstruct the stress maps in the tissue which leads the imaging modality towards MRI, even if it is an expensive modality. Our second question is: Is it possible to use ultrasound data to meet the same goals in case of patients suffering from cardiac pathologies? To answer, a fast and efficient automatic mesh morphing algorithm is introduced to generate hexahedral fine meshes for patients' coarse geometries obtained from echocardiography. In addition to this automatic mesh generation pipeline, we developed a method to detect the infarct zone as well as estimating an average active contraction value expressing the state of the tissue activity during systolic phase. This algorithm has been successful to detect the abnormal tissue zone in acute ischemia case. Following, it was applied to a cohort of 8 patients suffering from left bundle branch block obtained from GE Healthcare's ultrasound system, treated by resynchronization therapy.

École Nationale Supérieure des Mines de Saint-Étienne

NNT : *2017LYSEM004*

Sareh BEHDADFAR

CONTRIBUTION A L'EVOLUTION DE LA CONTRAINTE PATIENT-SPECIFIQUE DANS LE VENTRICULE GAUCHE HUMAIN PAR ANALYSE ELEMENTS FINIS A PARTIR D'IMAGES MEDICALES

Spécialité: Mécanique et Ingénierie

Mots clefs: Ventricule gauche, patient-spécifique, modélisation par éléments finis, GE Healthcare ultrasons

Résumé:

Les contraintes mécaniques dans le ventricule gauche du cœur peuvent présenter des anomalies en cas d'insuffisance cardiaque et il est donc important de pouvoir les reconstruire précisément pour comprendre, analyser, diagnostiquer et traiter une dysfonction cardiaque. Dans ce contexte, les calculs personnalisés ou patient-spécifiques par la méthode des éléments finis dans le cœur présentent un fort intérêt, mais il subsiste plusieurs défis pour les diffuser jusqu'à la clinique, à savoir qu'aucune méthode d'imagerie ne permet d'accéder aux propriétés mécaniques du tissu cardiaque ou à l'état de contraintes résiduelles de chaque patient. Ces deux données sont pourtant requises pour reconstruire les champs de contraintes dans le cœur en utilisant l'état de l'art. Dans cette thèse, afin de contribuer à la résolution de cette problématique, nous avons travaillé sur deux problèmes: 1. le champ de contrainte dans le tissu cardiaque peut être prédit par les modèles par éléments finis mais cela requiert de déterminer précisément les propriétés mécaniques du tissu. Certains modèles nécessitent plus de 11 valeurs à déterminer, ce qu'il n'est pas réaliste de vouloir identifier à l'échelle de chaque individu. La question est donc : est-il possible de reconstruire le champ de contrainte dans le tissu cardiaque dans un contexte d'incertitude sur les propriétés mécaniques ? Il est alors montré que pour plusieurs modèles de comportement, la dépendance des contraintes aux paramètres est faible. 2. Les modèles mécaniques nécessitent souvent des données d'imagerie de très haute résolution spatiale pour pouvoir reconstruire les cartes de contraintes dans le tissu, ce qui oriente la modalité l'imagerie vers l'IRM. Or il s'agit d'une modalité couteuse. Notre seconde question est donc : est-il possible d'exploiter des données d'échographie pour attendre les mêmes objectifs pour les patients ? Pour y répondre, nous avons introduit une nouvelle méthode de morphing de maillage éléments finis. A partir d'un maillage héxaèdres de référence de haute résolution, un maillage du ventricule gauche de chaque patient a été obtenu par morphing sur les images échographiques. Ensuite, nous avons développé une méthode pour détecter une éventuelle zone de tissu infarcté en estimant la valeur de contraction active moyenne exprimant l'état de l'activité tissulaire de chaque patient pendant la phase systolique. Cet algorithme a réussi à détecter la zone anormale des tissus dans le cas d'ischémie aiguë simulée numériquement puis il a été appliqué à une cohorte de 8 patients atteint du bloc de branche gauche et traité par resynchronisation.